工學博士學位論文

Fabrication of Silver Nanocomposites using Poly(vinyl alcohol) System and Their Environmental Applications

폴리비닐 알코올계를 이용한 은나노복합체의 제조 및 환경분야 응용

2014年 2月

서울大學校 大學院

化學生物工學部

宋 周 永

Fabrication of Silver Nanocomposites using Poly(vinyl alcohol) System and Their Environmental Applications

폴리비닐 알코올계를 이용한 은나노복합체의 제조 및 환경분야 응용

指導敎授 張 正 植

이 論文을 工學博士 學位論文으로 提出함

2013 년 11 월

서울大學校 大學院

化學生物工學部

宋 周 永

宋周永의 工學博士 學位論文을 認准함

2013 年 11 月

委 員 長 _____ (인)

副委員長 _____ (인)

委 員 _____ (인)

委 員 _____ (인)

委 員 _____ (인)

Fabrication of Silver Nanocomposites using Poly(vinyl alcohol) System and Their Environmental Applications

by

Jooyoung Song

Submitted to the Graduate School of Seoul National University in Partial Fulfillment of the Requirements for the Degree of Doctor of Philosophy

February, 2014

Thesis Adviser: Jyongsik Jang

Abstract

Fabrication of Silver Nanocomposites using Poly(vinyl alcohol) System and Their Environmental Applications

Jooyoung Song

School of Chemical and Biological Engineering

The Graduate School

Seoul National University

Fabrication and application of nano-sized materials is an emerging research field in modern society because the nanomaterials, the small materials with at least one dimension in the range 1–100 nm, provide unique chemical, physical, and optical properties, which are different from their bulk-counterpart. From the early work on gold nanoparticles to the recent development of graphene nanosheets, myriad nanomaterials have been discovered and studied in diverse fields. However, there is still lack of studies on the facile and environmentally benign synthetic methods.

This dissertation describes the fabrication of silver complex nanostructures with facile and environmentally benign approaches.

Silver halides (AgBr and AgCl) nanoparticles were synthesized under aqueous solution with assistance of poly(vinyl alcohol) stabilizer. Their size can be controlled by varying the reaction temperature. In this system, PVA was used as a stabilizer for the formation of silver halide nanoparticles through interaction with Ag^+ ions. After partial reduction process, the metallic silver decorated silver halides strongly absorbed visible-region light and showed excellent plasmonic photocatalytic activity under visible-light irradiation. It is verified that the size of the silver halide substrate affected its light absorption region.

Additionally, silver-embedded polymer nanofibers were also prepared by aqueous-phase synthetic method. In the preparation of silver/PVA nanofibers, AIBN formed complex with silver ions by interaction between the cyano groups and the silver ions. In addition, the AIBN acted as reductants for the reduction of silver ions, and PVA was used as a gelator and stabilizer for fabrication of fibrous nanostructures. After the complex-mediated reaction in aqueous medium, silver nanoparticles-embedded PVA nanofibers were obtained. Furthermore, the Ag/PVA/PTBAM nanofibers could be obtained by adding the TBAM monomer to the Ag/PVA/AIBN solution. In this route, the AIBN act as radical initiator for the dispersion polymerization of PTBAM. The

synthesized nanofibers were applied as an antibacterial agent and showed excellent antibacterial performance.

This dissertation provides the possibility of facile and *eco*-friend approaches for the preparation of silver-containing nanomaterials and their potential applications. PVA was used as polymeric stabilizer or structure-director for silver-containing nanocomposites. The nanomaterials presented in this dissertation could be applied to environmental fields such as antimicrobial agent and visible-light photocatalyst. In addition, this dissertation might not only provide a facile synthetic route for the silver-silver halide nanophotocatalyst and the silver/polymer nanofiber but also advance our understanding of the formation mechanism of the metal-containing nanocomposites.

Keywords: Silver, Silver halide, Nanocomposites, Poly(vinyl alcohol), Photocatalysis, Antimicrobial agent

Student Number: 2008-21086

List of Abbreviations

AIBN : 2,2'-Azobis(isobutyronitrile)

Ag@AgBr : Ag nanoparticles decorated AgBr

Ag@AgCl : Ag nanoparticles decorated AgCl

CFU : Colony forming unit

E. coli : Escherichia coli

EDX : Energy dispersive X-ray

FE-SEM : Field emission-scanning electron microscope

FTIR : Fourier transform-infrared

ICP : Inductively coupled plasma

KB : Kirby-Bauer

λ_{max} : Position of the maximum absorption wavelength

LB : Luria Bertani

MB : Methylene blue

MC : Methylene chloride

MIC : Minimum inhibitory concentration

MO : Methyl orange

NO : Nitric oxide

OD_{600} : Optical density at 600 nm of wavelength

PMMA : Poly(methyl methacrylate)

PTBAM : Poly[2-(*tert*-butylaminoethyl) methacrylate]

PVA : Poly(vinyl alcohol)

PVP : Polyvinylpyrrolidone

RhB : Rhodamine B

S. aureus : *Staphylococcus aureus*

SERS : Surface enhanced Raman spectroscopy

SPR : Surface plasmon resonance

TEM : Transmission electron microscope

TGA : Thermogravimetric

UV-vis : Ultraviolet-visible

XPS : X-ray photoelectron spectroscope

XRD : X-ray diffraction

List of Tables

List of Figures

indicate nodules on the cubic surfaces. The reactions were conducted in aqueous solution at 25°C with PVA as a stabilizer.

Figure 13. Schematic illustration of the plausible morphological change of the Ag@AgCl during the reduction procedure. The metallic Ag^0 clusters were formed on the AgCl surface through mild reduction process and these Ag^0 gradually grown bigger and finally cover over the surface of the AgCl nanoparticles.

Figure 14. Photographs of the Ag@AgCl suspensions prepared via the partial reduction of the as-prepared AgCl nanocubes. The AgCl nanocubes with edge length of ~57 (T25), ~61(T40), and ~87 nm (T60) were synthesized at 25, 40, and 60 °C, respectively and reduced to Ag@AgCl nanocomposites using L-arginine at 25 °C.

Figure 15. UV-visible absorbance spectra of the Ag@AgCl nanocomposites prepared via the partial reduction of the as-prepared AgCl nanocubes. The AgCl nanocubes with edge length of ~56, ~61, and ~87 nm were synthesized at 25, 40, and 60 °C, respectively and reduced to Ag@AgCl nanocomposites using L-arginine at 25 °C. The spectra are normalized against the intensity of major peaks.

Figure 16. FE-SEM images of the Ag@AgCl nanocomposites prepared by

reducing the (a) ~56, (b) ~61 and (c) ~87 nm sized AgCl substrate. The arrows in FE-SEM images indicate nodules (metallic Ag) on the cubic surfaces. The scale bars are 100 nm.

Figure 17. UV-visible absorbance spectra of the Ag@AgCl dispersion prepared via the partial reduction of the as-prepared AgCl nanocubes at different reduction times. The AgCl nanocubes synthesized at 25, 40, and 60 °C have different edge length of (a) ~57, (b) ~61, and (c) ~87 nm, respectively. The as-prepared AgCl nanocubes are reduced by L-arginine under same reduction condition.

Figure 18. Photocatalytic degradation of MB over different Ag@AgCl nanoparticles prepared with various reduction times.

Figure 19. Scheme of the proposed plasmonic photocatalytic mechanism of the Ag-decorated AgCl nanocomposite.

Figure 20. Photocatalytic degradation of MB over different Ag@AgCl nanoparticles prepared with the different sized AgCl substrates.

Figure 21. Photocatalytic degradation of (a) MB, (b) MO, and (c) RhB dyes over Ag@AgCl T25 nanoparticles. The photocatalytic experiments were done under visible light (> 400 nm) irradiation and the cycling

test was performed using the 8 h reduced samples. The photocatalytic efficiency (%) was calculated based on the first degradation data.

Figure 22. Low-magnification FE-SEM images of the synthesized AgBr nanoparticles.

Figure 23. FE-SEM images of the AgBr nanoparticles prepared with low concentration of PVA (molar ratio to silver precursor is 50). The arrows indicate the trigonal prism shaped AgBr.

Figure 24. FE-SEM images of the AgBr prepared by precipitation reaction between $AgNO_3$ and NaBr in aqueous solution without the PVA stabilizer.

Figure 25. FE-SEM images of the AgBr nanocubes prepared at different reaction temperature: (a) 25, (b) 40, and (c) 60 °C. The insets show the magnified images of each product and the scale bars in the inset images are 200 nm.

Figure 26. FE-SEM images of the Ag@AgBr nanocomposites synthesized by reducing the as-prepared AgBr nanocubes. The reduction was conducted using the AgBr nanocubes prepared at different reaction temperature: (a) 25, (b) 40, and (c) 60 °C. The spectra are

Table of Contents

1. Introduction

1.1 Background

1.1.1 Nanomaterials

The advancement of science and technology has resulted in the fabrication of tiny materials with at least one dimension in the range 1–100 nm; defined as nanomaterials [1-6]. Thanks to the efforts of numerous research groups, nanostructures of metals [7-9], inorganic complexes [10-13], and polymers [14-17] of myriad shapes, such as a sphere, cone, rod, fiber, tube, sheet, etc., have been realized. Interest in nanostructured materials has been growing steadily due to their fascinating properties and potential applications, both of which stem from their nanoscale dimensions [1-3]. They displayed unique quantum phenomena, atomic physics, and enhanced performances compared to bulk materials (over the micron size) due to their quantum confinement effect and increased surface-to-volume ratio. From the early work on gold nanoparticles to the recent development of graphene nanosheets, myriad nanomaterials have been discovered and studied in diverse fields. Fabrication of these nanomaterials combining physics, chemistry, and biosciences might advance our understanding about material science and nature.

1.1.2 Metal nanostructures

Noble-metal nanocrystals have attracted numerous attentions due to their potential use in catalysis, electronics, optics, and biology [18-21]. The physicochemical properties of these nanocrystals are highly affected to their size and shape [9, 22]. When light incident to a metal particle, the oscillating electromagnetic field of the light induces a collective coherent oscillation of the free electrons of the metal and it causes a forming of dipole oscillation along the direction of the electric field of the light (**Figure 1**) [22-24]. The amplitude of the oscillation reaches maximum at a specific frequency, called surface plasmon resonance (SPR) [22-24]. These SPR properties of metal nanomaterials exhibit a strong correlation with their shape and size. Furthermore, because the shape determines the arrangements of atoms on the surface of metal nanocrystal, the reactivity and selectivity of metal nanocatalysts can be tuned by controlling the shape of these particles [25,26]. In 1850's Michael Faraday synthesized Au colloids in aqueous system [27]. Since then, myriad of solution-phase methods have been developed for preparing metal colloids; however, most of the products had some problems such as polydispersed sizes and pooly defined shapes. Last decade, thank to the numerous efforts of research groups, solution-phase

synthetic routes for various metal nanostructures with the quality, quantity, and reproducibility have been successfully developed. Especially, Xia and co-workers have demonstrated poly(vinyl pyrrolidone)-assisted synthetic procedure for metal nanostructures with various shapes such as nanocube, nanofiber, nanoplate, etc.[9,28-31] Although the many meaningful results have been reported, the study on controlling the assembly of metal atoms into nanocrystals is still at a rudimentary stage.

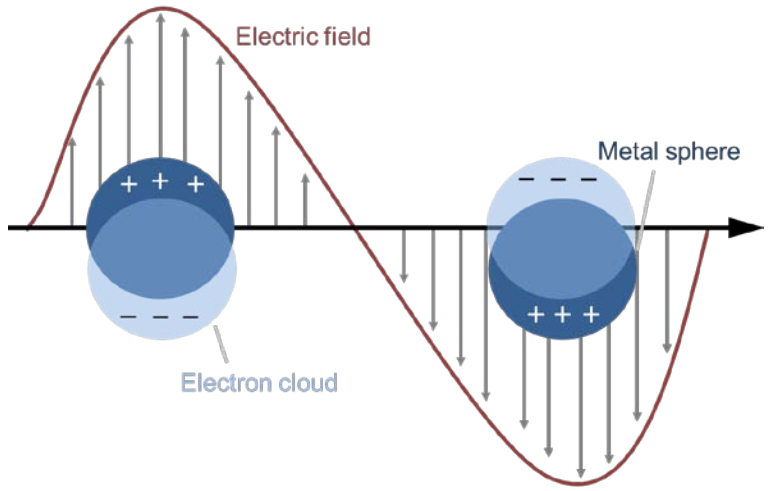

Figure 1. Schematic diagram illustrating a surface plasmon resonance in plasmonic nanoparticles

1.1.2.1 Silver nanoparticles

Historically, silver has most widely been used in jewelry/metal-craft and health field. In modern industry, Ag, particularly in nanoparticle form, has been used as a catalyst in various oxidation or oxidative coupling reactions. For instance, the methanol can be transformed to formaldehyde with catalytic-assistance of the silver [32]. In addition, Ag nanoparticles can convert ethylene to ethylene oxide, an important industrial precursor [9]. Furthermore, silver nanoparticles are well known as excellent antimicrobial agents. There are numerous reports of studies with antimicrobial composites using silver nanoparticles as biocidal additives due to their excellent antimicrobial properties. [33-35] Additionally, because of their unique and strong SPR properties, silver nanostructures also have been applied as substrates for surface enhanced Raman spectroscopy (SERS), optical labeling, and optical sensing.

1.1.2.2 Silver halide nanocomposite

Silver halide (AgCl and AgBr) is extensively used as source materials for photographic film because of its photosensitive property [36]. Recently, the silver halides containing metallic silver nanoparticle have been received great interest due to their excellent plasmonic

photocatalytic activity under visible light irradiation. The Ag nanoparticles can serve as visible light sensitizers to prepare the effective photocatalysts due to their SPR property [37]. Additionally, the Ag nanoparticles on the surface of semiconductor can facilitate the separation of photo-generated electron-hole pairs by trap the electrons, leading the enhancement of the photocatalytic efficiency [38,39]. In 2008, Huang's group developed AgCl nanoparticles decorated with Ag nanograins (abbreviated as Ag@AgCl) as a plasmonic photocatalyst using an ion-exchange reaction (for AgCl production) and strong light irradiation (for Ag^0 formation) [40]. The Ag@AgCl composite showed efficient and stable photocatalytic performance in visible light. Since then, various strategies for the formation of silver-silver halide composite photocatalysts have been developed. Li *et al.* synthesized a porous AgCl/Ag nanocomposite with sponge-like morphology via a two-step route; the as-prepared nanocomposite had stable catalytic activity under visible light irradiation [41]. Xu *et al.* fabricated Ag/AgCl composites using a hydrothermal method in an ionic liquid system, which could repeatedly degrade methyl orange (MO) in visible light [42]. Additionally, Wang *et al.* demonstrated that Ag@AgBr (Ag nanoparticles decorated AgBr) composite prepared by the ion-exchange

reaction can decompose organic dye under visible light [43]. The Ag@AgBr can absorb in a wide range of visible light because of SPR of the deposited silver nanoparticles. In general, nano-photocatalysts allow the improved catalytic efficiency due to their large surface area which can provide more reactive sites for the catalysis. However, there is limited information on the control of the morphology and size of the Ag nanoparticle/silver halide in nanoscale is because of the fast precipitation reaction between Ag^+ and Cl^- ions. Recently, polyvinylpyrrolidone (PVP) and ethylene glycol were used as stabilizers to slow down and control the reaction rate. Sun and co-workers fabricated AgCl nanocubes with an average edge length of 130 nm [44]. However, the nanocubes were agglomerated and grew into micron-sized particles under the harsh, reducing reaction conditions [45]. An *et al.* synthesized an AgCl:Ag nanophotocatalyst with an average diameter of 85 nm *via* a two-step approach [46]. That approach required the use of a surfactant and strong reducing agents, which are not environmentally friendly. Therefore, it is imperative to develop the reliable synthetic strategy for the Ag nanoparticle/silver halide nanostructures.

1.1.3 Metal-polmer nanocomposite

Various synthetic strategies have been developed for the preparation

of the metal-polymer nanocomposite. The most frequently used approach to prepare the polymer nanocomposite is based on the entrapment of metal precursor on polymer matrix followed by reduction [47-50]. In this approach, the well-dispersed metal nanoparticles decorated polymer can be obtained using the polymer with metal-binding functional groups. For instances, Jeon *et al.* described the one-step synthesis of Ag and Au nanoparticles dispersed polymeric film using PVP as both the reducing agent and polymer matrix [47]. They explain that the hydroxyl (-OH) end groups of PVP reduce the metal ions to the metal nanoparticles with a narrow size distribution at high temperature. Recently, numerous efforts have been devoted to developing the polymer nanostructures containing metal nanoparticles to enlarge their specific surface area, leading the better performance.

1.1.3.1 Electrospun silver-polymer nanofibers

In general, polymer nanofibers and nanotubes have mainly been produced using templates such as anodic aluminium oxide [51,52], mesoporous silica [53], surfactants [54], and biomaterials [55]. Only within the last decade has a newly introduced electrospinning method been used to prepare one-dimensional polymer nanostructures [56-58].

Continuous fibers with submicron diameters can easily be prepared by controlling electrospinning conditions such as solution viscosity, solution conductivity, and electric-field intensity [56]. In order to extend their application field, embedding of functional nano-compound such as silver, gold, TiO_2, and ZnO during preparation of electrospun polymer nanofibers has been attempted [59-62]. Silver nanoparticles in particular have been studied intensively for antimicrobial application. For example, one-pot and smart preparation routes for synthesis of Ag/polymer nanofibers were developed by Shi *et al.* [63]. They used the electrospinning solvent as the reducing agent and a nylon-6 matrix as the stabiliser for *in situ* synthesis of silver nanoparticles. In this process, silver nanoparticle-embedded polymer nanofibers were synthesized *via* electrospinning without additional reducing/protecting agents, and exhibited excellent antibacterial activities. Mahanta and Valiyaveettil synthesized the methacrylated poly(vinyl alcohol) (PVA) nanofibers containing Ag nanoparticles *via* electrospinning method [64]. They presented that the polymers with hydroxyl groups reduced the silver ions to metallic Ag nanoparticles during the electrospinning process. As listed above, most of these nanocomposites have been prepared *via* the electrospinning method, which needs a high electric potential to fabricate

the nanofibers. Thus, facile synthetic strategy for silver–polymer composit nanofiber is still challenging and of particular interest.

1.1.3.2 Solution-phase synthesized silver-polymer nanofibers

From an industrial viewpoint, solution-phase synthesis is a well-established mass production technique [65,66]. A variety of solution-phase methods for preparation of metal or inorganic nanostructures have been developed [9,29,67]. However, solution-phase synthesis of polymer nanostructure remains limited because nanometre-sized polymers are unstable and readily revert to the bulk state. To overcome these problems, solution-phase synthesis of metal-polymer complex nanostructures was introduced which uses the coordination activity between metal binding groups of polymer and metal ions (or metal nanoparticles) as a driving force. In these methods of synthesis, the polymer can be fabricated at a submicron size because the metal provides mechanical stability to the composite nanostructure. Among the metal compounds, silver has been investigated extensively due to its stability and excellent antimicrobial activity [68-70]. For instance, silver nanoparticles embedded with antibacterial polyrhodanine nanofibers were fabricated by one-pot oxidation polymerization in ethanol solution [71]. In this process,

rhodanine forms a complex with silver cations and the oxidative polymerization of rhodanine performed using silver ions as an initiator, and the silver ions themselves, were simultaneously reduced to silver nanoparticles. During the reaction, the silver-polyrhodanine composite linearly assembled due to the shear force of magnetic stirring and had an elongated structure. Although the use of the silver ion as an initiator of oxidative polymerization is facile synthetic route for silver nanoparticle-impregnated polymers, the number of possible monomers is limited due to the high oxidation potential of Ag(I) (E = 0.8 V). Thus, fabrication of the metal-embedded polymer nanostructure is still challenging.

1.1.4 Application of silver-containing nanocomposites

1.1.4.1 Visible light-responsive plasmonic photocatalyst

Photocatalysts are promising materials for solar energy applications [72-74]. Considering that visible light accounts for ~43% of sunlight, it is desirable to fabricate a photocatalyst having high activity in visible light [75-77]. Various strategies for the synthesis of visible-light-driven photocatalysts have been developed [78-81]. Metal- or nonmetal-doped TiO_2 and ZnO nanostructures have been designed to harvest visible-region light by controlling the bandgap of these semiconductors [78,79]. An organic photosensitizer has been used to improve the visible light absorption of photocatalysts [80]. However, photocatalysts typically have several disadvantages, such as limited visible light responses and poor stabilities, and are environmentally unfriendly [81].

Noble-metal nanoparticles (mainly gold and silver) can absorb visible light because of their unique SPR property [82-84]. These plasmonic nanoparticles can be used as an alternative type of sensitizer to improve the visible light absorption of photocatalysts without the stability and pollution issues [85]. Various types of metal nanoparticle-deposited semiconductors have been developed as plasmonic photocatalysts [85,86]. For instance, various metal oxides such as ZnO,

TiO_2, and Cu_2O photocatalysts decorated with Ag nanoparticles have been synthesized for dye-decomposition under visible light condition. In particular, Ag nanoparticle/silver halide composites are of particular interest because of their excellent plasmonic photocatalytic activities in visible light [40,87-89]. In 2008, Huang *et al.* synthesized Ag@AgCl as a plasmonic photocatalyst using an ion-exchange reaction (for AgCl production) and strong light irradiation (for Ag^0 formation) [40]. The Ag@AgCl composite showed efficient and stable photocatalytic performance in visible light. Since then, various strategies for the formation of silver-silver halide composite photocatalysts have been developed.

1.1.4.2 Antibacterial agent

Although human mortality from bacterial infections has decreased over the last century due to developments in medical science, these remain the number one cause of death [90]. A large number of bacterial infections originate from viable bacteria that adhere to implants and medical devices [91,92]. When bacteria attach to a material surface and cell numbers increase, they start to form a biofilm. After developing on a surface, this biofilm is extremely difficult to remove and allows

microbial cells to survive even under harsh conditions. In contrast to planktonic (free-floating) bacteria, the bacteria in biofilms are up to 1000 times more tolerant to antibiotics and other biocides [93,94]. Thus, inhibition of biofilm formation is considered to be the most important goal in antimicrobial research. To do this, it is necessary to inhibit the early stages of bacterial adhesion. In general, this can be achieved by either killing the planktonic bacteria prior to adhesion using biocides, or by modifying surface properties to inhibit bacterial adhesion. During the last decades, numerous effective bactericidal materials that inhibit bacterial growth have been developed including metal, metal oxide, and polymeric nanomaterials (even their composite nanomaterials).

1.1.4.2.1. Antibacterial silver nanoparticles

Silver is an excellent antimicrobial agent because of its broad-spectrum biocidal activity and limitation of development of resistant microbial strains. In an in-depth study, Morones *et al.* demonstrated the bactericidal effect of silver nanoparticles with sizes in the range of 1−100 nm [34]. Alt *et al.* reported the in vitro antibacterial activity of nanosilver against multiresistant bacteria and the in vitro cytotoxicity of silver nanoparticles loaded into poly(methyl methacrylate) (PMMA) bone

cement [95]. It is well-known that silver nanoparticles are oxidized by oxygen, leading to the silver ion releasing. The reactions are formulated as follows.

$$4Ag^0 + O_2 \rightarrow 2Ag_2O$$

$$Ag_2O + 2H^+ \rightarrow 2Ag^+ + H_2O$$

In recent year, Alvarez *et al.* demonstrated that the antibacterial activity of silver could be adjusted by controlling the release of Ag^+ ions [96]. The Ag nanoparticles can show the excellent antibacterial activity by releasing the Ag^+ ions to the surrounding bacteria cells (**Figure 2**). Although not fatal, silver nanoparticles have shown toxicity toward mammalian cells. The toxicity of colloidal silver nanoparticles has been attributed to uptake of silver nanoparticles by cells or to the oxidative release of silver cations from the surface of the silver nanoparticles that can affect basic functions in mammalian cells [97]. From this viewpoint, immobilization of nanosilver onto adequate substrates is advantageous because it inhibits direct uptake of the nanoparticles by cells. In addition, compared to colloidal silver nanoparticles, immobilized silver nanoparticles effectively resist oxidation and aggregation, which can reduce the antibacterial efficiency [35]. There are numerous reports on the silver nanocomposites and their antibacterial performances [98-100].

For example, Lu *et al.* reported that silver nanoparticles embedded into silicon nanowires are much more stable and resistant to aggregation than colloidal silver nanoparticles. Silver impregnated polymer matrix provides the antimicrobial efficacy with sustained release of silver [35].

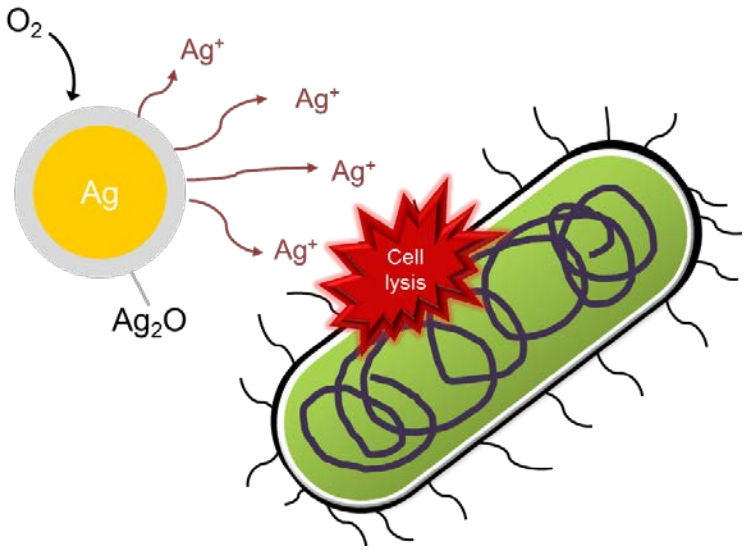

Figure 2. Schematic diagram illustrating a interactions between Ag nanoparticles, Ag ions, and bacterial cell interactions.

1.1.4.2.2. Antibacterial polymeric compounds

During the last decades, the field of antimicrobial polymers has great advances in terms of efficacy enhancement, control of size and morphology, and synthetic route development. Until now, numerous polymeric antimicrobial nanostructures have been successfully developed *via* various synthetic routes to kill the harmful bacteria as summarized in **Table 1**.

Polymeric antimicrobial materials can be divided into two categories based on their biocidal mechanism: biocide-releasing polymers and contact-active polymers. The first kills bacteria via the release of a low-molecular-weight biocide. In 1996, Worley *et al.* designed N-halamine groups containing polymers [101,102]. These synthesized chlorine-containing polymers showed excellent bactericidal activity through the release of chlorine or hypochlorite. In addition, nitric oxide (NO)-containing polymers that kill bacteria via release of the biocidal NO have been developed [103]. Despite the superior antibacterial activity, release-type biocides have serious defects, such as duration of efficacy and environmental contamination.

To fabricate ecologically sound and long-lasting antimicrobial agents, non-leaching (contact-active) antimicrobial polymers have been

designed. It is well known that bacterial cells generally have a net negative charge at their surface due to the teichoic acids of the Gram-positive bacterial cell wall and the phospholipids within the outer membrane of Gram-negative bacteria [104,105]. Based on these features, cationic polymers that can interact with negatively charged bacterial membranes have been intensively investigated as efficient antimicrobial materials [104-106]. Although the exact mechanism underlying the interactions between membrane-active biocidal polymers and bacterial cells remains unclear, membrane-disruption is broadly accepted as the bactericidal mechanism of cationic polymers. The outer membrane of *Escherichia coli* (*E. coli*) is damaged on contact with cationic polymers, until finally cellular integrity is lost. In 2011, Timofeeva reviewed the bactericidal mechanisms, and activity factors, of various antimicrobial polymers [104].

Although contact-active polymers have some advantages, such as long-term durability, being ecologically sound, and prevention of resistance, their moderate antimicrobial efficiency compared with release-type biocides is in need of improvement [107]. The size of antimicrobial agents has been demonstrated to be a key factor in their efficacy [108,109].

In other words, biocidal efficiency depends on the exposed active area of the biocide. During the last decade, nano-sized antimicrobial particles have been reported to display enhanced antimicrobial activity against typical bacteria when compared with their bulk counterparts [110-112]. Previous research has shown that cationic polymer nanoparticles with a diameter of 17 nm have enhanced bactericidal performance against *E. coli* and *Staphylococcus aureus* (*S. aureus*) compared with cationic polymer bulk powder (several tens of μm in size) under equivalent experimental conditions [110]. Additionally, as the size of biocidal particles decreases, the fractional survival of bacteria decreases more rapidly. These results illustrate that excellent antimicrobial activity can be achieved by decreasing the size of biocidal materials. Antibacterial nanoparticles with an expanded surface area provide more active sites to contact planktonic bacteria, leading to improved bactericidal activity.

Table 1. Synthetic route and applications of polymeric antimicrobial nanostructures.

Polymers	Preparation route	Morphology	Size[a]	*Bacteria*	Ref.
Poly[2-(tert-butylaminoethyl) methacrylate	Surface-initiated photopolymerization	Polymer-coated titania nanoparticle	~20 nm	*E. coli*, *S. aureus*	113
Poly[2-(tert-butylaminoethyl) methacrylate	Vapour deposition polymerization	Polymer-coated silica nanosphere	17-50 nm	*E. coli*, *S. aureus*	110
Poly[2-(tert-butylaminoethyl) methacrylate	Radical-mediated dispersion polymerization	Ag nanoparticles embedded nanofiber	~40 nm	*E. coli*, *S. aureus*	114
Poly(2-(dimethylamino) ethyl methacrylate)	Surface-initiated atom transfer radical polymerization	Polymer coated Fe_3O_4 nanosphere	50-150 nm	*E. coli*	115
Poly(2-(dimethylamino) ethyl methacrylate)	Electrospinning	Polymer fibrous structure	0.3~1.3 μm	*E. coli* *S. aureus*	116
Poly(3-allyl-5,5-dimethylhydantoinco)	Radical polymerization	Polymer-coated magnetic silica nanosphere	~144 nm	*S. aureus* *P. aeruginosa*	117
Poly(3-allyl-5,5-dimethylhydantoinco)	Seeded polymerization	Polymer-coated silica nanoparticle	11-26 nm	*E. coli* *S. aureus*	118
Poly(dimethylamino methylstyrene)	Vapor crosslinking method	Polymer film	~800 nm	*B. subtillis* *E. coli*	119
Polyrhodanine	Seeded polymerization	Polymer-coated silica nanosphere	15-56 nm	*E. coli*, *S. aureus*	111
Polyrhodanine	Chemical oxidation polymerization	Polymer-coated γ-Fe_2O_3 nanosphere	~10 nm	*E. coli*, *S. aureus*	120
Polyrhodanine	Chemical oxidation polymerization	Ag nanoparticles embedded nanofiber	~30 nm	*E. coli*, *S. aureus*, *C. albicans*	71
Polyrhodanine	Chemical oxidation polymerization	Ag nanoparticles embedded nanotube	~200 nm	*E. coli*, *S. aureus*	121
N-halamines introduced nylon 6	Electrospinning	Nanofiber membrane	100~500 nm	*E. coli* *S. aureus*	122
Poly(ethylene terephthalate)/chitosan	Electrospinning	Nanofiber mat	300-500 nm	*S. aureus* *K. pneumoniae*	123
Magainin-I grafted copolymer brush	Atom transfer radical polymerization	Polymeric brush film	~100 nm	*L. ivanovii* *E. coli*	124
Poly(N-isopropyl acrylamide)	Sonochemically synthesize	Polymer-coated silica nanoparticle	~170 nm	*Bacillus sp.*	125
Chitosan-polycaprolactone	Electrospinning	Nanofibrous membranes	200-400 nm	*S. aureus*	126
Quaternized chitosan	Electrospinning	Nanofibrous mat	50-500 nm	*E. coli* *S. aureus*	127
Carboxymethyl chitosan	Repetitive reaction between Michael addition and amidation	Dendrimer core-shell nanoparticle	~20 nm	*E. coli* *S. aureus*	128

[a] Size means the diameter (nanoparticle, nanofiber, and nanotube) or the thickness (film)

1.2 Objectives and Outlines

1.2.1 Objectives

The aim of this dissertation is providing eco-friend method to fabricate silver-containing nanocomposites in aqueous solution. PVA was used as polymeric stabilizer or structure-director for silver-containing nanocomposites. Through facile and environmentally-friendly methods in each experimental condition, the silver halide nanoparticles and silver-embedded polymer nanofibers could be obtained with unique potential properties. Finally, the environmental applications of these prepared nanocomposites such as photocatalytic and antibacterial performances are presented. This investigation might not only provide a facile synthetic route for the silver-silver halide nanophotocatalyst and the silver/polymer nanofiber but also advance our understanding of the formation mechanism of the metal-containing polymer nanocomposites.

1.2.2. Outlines

This dissertation could be divided into two sections: aqueous-phase synthesis of silver-containing nanocomposites and their environment applications. In the fabrication part, silver halide nanocomposites were

synthesized *via* precipitation reaction in PVA-dissolved aqueous solution. Silver/PVA nanofibers were synthesized *via* complex-mediated growth process. Silver/PVA/PMMA composite nanofibers were obtained by radial-mediated dispersion polymerization. In the application part, visible-light responsive photocatalytic and antibacterial properties of as-prepared nanocomposites were presented. In viewpoint of fabrication of nanocomposites and their application field, this dissertation involves the following subtopics:

I. Fabrication of size-controllable Ag@AgCl plasmonic nanoparticles through aqueous system as visible-light plasmonic photocatalysts

II. Fabrication of Ag@AgBr photocatalytic nanoparticles in aqueous system with PVA stabilizer

III. Fabrication of silver/PVA composite nanofiber in aqueous system

IV. Fabrication of silver/PVA/PTBAM nanofibers through aqueous system as antibacterial agents

2. Experimental Details

2.1 Fabrication of silver halide nanomaterials

2.1.1 Fabrication of AgCl nanocubes with PVA stabilizer

All reagents including PVA (MW: 124,000 – 186,000), silver nitrate ($AgNO_3$), sodium nitrate (NaCl), and L-arginine were purchased from Sigma Aldrich Co. The reactants were used without further purification. Unless clearly defined, the reaction was performed under laboratory light condition. The AgCl nanoparticles were synthesized via a precipitation reaction between $AgNO_3$ and NaCl in aqueous solution with the assistance of PVA. The reaction is formulated as follows:

$$AgNO_3 + NaCl \rightarrow AgCl_{(s)} + NaNO_3$$

Under the experimental conditions, the PVA played an important role in the formation of nano-sized AgCl particles. The PVA was dissolved in deionized water (0.5 g to 50 mL) as stabilizer. When the silver nitrate (0.058 mmol) was introduced into the PVA aqueous solution, the PVA hydroxyl groups interacted with Ag^+ ions (from $AgNO_3$) to form a PVA/Ag^+ complex in the aqueous phase [70,114]. Then, as the halide doners, the 1 mL of NaCl solution (58.8 mM) was sequentially injected dropwise. Addition of NaCl to the PVA/Ag^+ dispersion enabled the

synthesis of AgCl nanoparticles at the reactive site of the complex where the Cl^- ions (from NaCl) came into contact with the silver cations. The long PVA chains increased the viscosity of the reaction solution and reduced the diffusion coefficients of both Ag^+ and Cl^- ions, thereby slowing the precipitation reaction [45,129]. Additionally, the PVA served as a capping agent to stabilize the formed AgCl nanoparticles and prevent them from agglomerating. To observe the temperature effect, the precipitation reaction was performed at various temperatures from 25 to 90 °C for 30 min under laboratory light condition.

2.1.2 Partical reduction of AgCl nanoparticles

The overall synthetic procedure of the Ag@AgCl composite nanoparticle is illustrated in **Figure 3**. The 1 mL of L-arginine dissolved solution (287 mM) was added to the as-prepared AgCl solution for the partial reduction of Ag^+ ions of AgCl to form the Ag^0 nanograins. As a mild reducing agent, the L-arginine interact with the Ag^+ ion on the surface of AgCl and slowly reduces it to metallic Ag^0 and thus, the partially reduced AgCl (metallic Ag decorated AgCl nanocomposites) could be obtained. After specific time of reduction, the formed Ag@AgCl nanoparticles were centrifuged and washed with deionized

water to remove residual reagents.

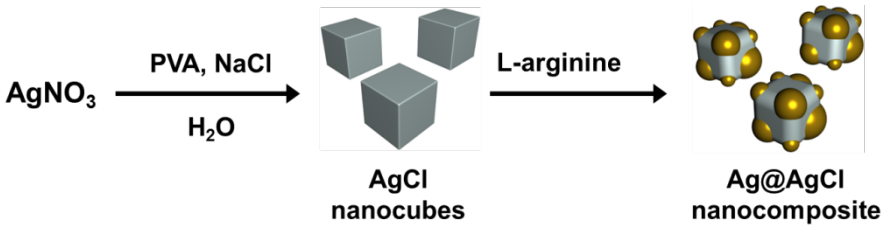

Figure 3. Illustration of the synthetic procedure used to prepare the Ag@AgCl nanoparticles.

2.1.3 Fabrication of AgBr nanocubes with PVA stabilizer

Silver nitrate ($AgNO_3$, ≥ 99.0%) and sodium bromide (NaBr, ≥ 99.0 %) were purchased from Aldrich (St. Louis, MO) and used as precursors for the silver bromide nanoparticles. PVA (Mw: 9000-10000, 31000-50000, 146000-186000,) and L-arginine (≥ 98%) were also purchased from Aldrich and used as stabilizer and reducing agent, respectively.

The AgBr synthesized under similar conditions as the AgCl nanoparticles except for the use of NaBr as a halide precursor. The AgBr nanoparticles also were synthesized in the PVA dissolved aqueous solution. As a precursor, $AgNO_3$ (0.059 mmol) was added to the PVA solution and the 1 mL of NaBr solution (58.8 mM) was sequentially injected dropwise. The precipitation reaction of AgBr was performed 1 h at various temperatures.

2.1.4 Partical reduction of AgBr nanoparticles

To form the metallic Ag nanoclusters on the surface of AgBr, the L-arginine dissolved solution (287 mM) was added to the as-prepared AgBr suspension as mild reducing agent. The reduction proceeded for 30 min under the laboratory light condition at room temperature. After the

reduction process, the synthesized Ag@AgBr nanoparticles were centrifuged and washed with deionized water to remove residual reagents.

2.2 Fabrication of silver-polymer composite nanofibers

2.2.1 Fabrication of silver/poly(vinyl alcohol) nanofibers by complex-mediated growth

As a metal precursor, $AgNO_3$ was purchased from Aldrich (St. Louis, MO) and used without further purification. The PVA was also purchased from Aldrich and used as polymeric gelator and stabilizer. The PVA (Mw: 146000-186000, 87-89 % hydrolyzed; Mw: 31000-50000, 87-89 % hydrolyzed; Mw: 9000-1000, 80 % hydrolyzed) was also purchased from Aldrich and used as polymeric gelator and stabilizer.As a complex precursor, AIBN was obtained from Junsei Chemical Co., Ltd. (Japan).

As a stabilizer and structure director, PVA was dissolved in deionized water (0.5 g to 50 mL). Then, $AgNO_3$ (0.118 mmol), was added to the PVA solution and AIBN was sequentially added. At early stage of reaction, the AIBN-Ag^+ ion complex was formed *via* interaction between the cyano group of AIBN and Ag^+ ions. During the fabrication procedure of polymer nanofibers, magnetic stirring was employed for shear flow. Under this experimental condition, PVA became oriented with silver ions in the flow direction. Consecutively, the nanofibrous structures were grown from the AIBN-Ag^+ complex. In this system, PVA acted as not only a gelator but also a stabilizing agent to prohibit silver complex

sintering. The reaction was proceeded for 24 h at 60 °C with a magnetic stirring. After the reaction, the opaque sample solution could be obtained. The synthesized silver/PVA nanofibers were collected by centrifugation with 12000 rpm for 30 min and washed with an excess amount of distilled water to remove the residual reagents.

2.2.2 Fabrication of silver/poly(vinyl alcohol)/poly[2-(tert-butyl aminoethyl) methacrylate] nanofibers using radical mediated dispersion polymerization

The monomers 2-(tert-butylamino)ethylmethacrylate (TBAM) and methylmethacrylate were purchased from Aldrich (St. Louis, MO). TBAM was used without further purification, and methylmethacrylate was used after purification with an inhibitor remover. PVA (Mw: 124,000−186,000), silver nitrate, and silver sulfadiazine (SSD) were also obtained from Aldrich (St. Louis, MO). The radical initiator AIBN was obtained from Junsei Chemical Co., Ltd. (Japan). All purifications and reactions were carried out under atmospheric pressure.

As a stabilizer and structure director, PVA was dissolved in deionized water (1.0 g to 200 mL). Silver precursor, $AgNO_3$ (0.118 mmol), was added to the PVA solution and stirred for 1 h with a magnetic stirring bar.

The hydroxyl group of PVA has some lone pair electrons which can coordinate with silver ions. When the silver ion was introduced into the PVA solution, the silver ion/PVA complexes were formed by the coordinative interaction. Next, the AIBN (0.6 mmol) dissolved methylene chloride solution (0.75 mL) was injected into the PVA solution as a seed for complex, and a radical initiator. The reaction was performed at 60 °C. At early stage of reaction, the AIBN-Ag^+ ion complex was formed *via* interaction between the cyano group of AIBN and Ag^+ ions. During the fabrication procedure of polymer nanofibers, magnetic stirring was employed for shear flow. Under this experimental condition, PVA became oriented with silver ions in the flow direction. Consecutively, the nanofibrous structures were grown from the AIBN-Ag^+ complex. In this system, PVA acted as not only a gelator but also a stabilizing agent to prohibit silver complex sintering. When TBMA (400 μL) was injected, the existing radicals initiated the polymerization of TBAM monomer with reducing the silver ions spontaneously. Injected TBAM was adsorbed onto the linear assembly of silver/PVA complex because hydrogen bonding was formed between hydroxyl (-OH) functional group of PVA and carboxyl (-COO) group of TBAM. As a result, TBAM was tightly bound with PVA and then polymerized onto

the silver/PVA complex. The polymerization proceeded for 24 h and the synthesized silver/PVA/PTBAM nanofibers were collected by centrifugation and washed with an excess amount of methanol solution to remove the residual reagents.

2.3 Applications

2.3.1 Photocatalytic properties of silver halide nanoparticles

2.3.1.1 Materials

For photocatalytic test, methylene blue (MB, ≥ 82.0 %), methyl orange (MO, ≥ 85 %), and rhodamine B (RhB, ~ 97 %) were purchased from the Aldrich and used as organic dyes.

2.3.1.2. Dye-decomposing test

The photocatalytic properties of the Ag@AgCl and Ag@AgBr nanoparticles were evaluated in terms of the decomposition of dye molecules. The MB, MO, and RhB were used as organic dyes. For the test, 10 mg of as-prepared sample was added into the 50 mL of dye-dissolved aqueous solution (50 mg/L). Prior to the light irradiation, the prepared solution was stirred for 30 min in the dark to ensure the establishment of the adsorption-desorption equilibrium for the dye. The

photocatalytic test was performed under visible light irradiation by using a Xenon-lamp with a UV cut-off filter ($\lambda > 400$ nm) at room temperature. After specific contact time, about 3 mL aliquots were taken and centrifuged to remove the dispersed photocatalyst. The concentration of the dye was measured using the UV-vis spectroscopy. With different UV-irradiation time, the solution was analyzed by UV-vis spectrophotometer at its characteristic wavelength (λ=665 nm) to determine the degradation yield (C/C_0). In addition, the used Ag@AgCl nanoparticles were collected by centrifugation and washed with distilled water for the cycle photocatalytic experiments. During the photocatalytic test, the temperature was maintained at 25 °C using water bath. The photocatalytic efficiency (%) was calculated on the basis of the first degradation data.

2.3.2. Antibacterial properties of silver-polymer nanofibers

2.3.2.1 Materials

For the evaluation of antimicrobial properties, *E. coli* (ATCC 8739) and *S. aureus* (ATCC 6538) were provided from Fisher Company. Microorganisms were cultivated in sterilized LB broth and then incubated overnight at 37 °C with a shaking incubator. The bacterial

suspensions employed for the tests contained from 10^6 to 10^7 colony forming units (CFU) per mililiter.

2.3.2.2 Modified Kirby-Bauer antimicrobial test

For the modified Kirby-Bauer (KB) test, solid-state SSD and Ag/PVA/PTBAM nanofibers were pressed into a disk shape with a diameter of 13 mm using a hydraulic press. The prepared samples had equal amount of silver. Separately, 50 μL of *S. aureus* suspension (10^6–10^7 CFU/mL) was cultured on Luria−Bertani (LB) agar plates. Then, each prepared sample disk was gently placed on the center of the bacteria growth on the LB agar plates and incubated overnight at 37 °C. Bacterial colony growth was observed, and the zone of inhibition was measured to evaluate the antibacterial performance.

2.3.2.3 Antibacterial kinetic test

For the kinetic test, *E. coli* and *S. aureus* were prepared. The culture medium of each bacterium was inoculated with bacteria and incubated overnight at 37 °C. Bacterial growth rates were measured by monitoring the optical density at 600 nm (OD_{600}) using a spectrophotometer. The incubated bacteria were injected to fresh media and grown at 37 °C with

200 rpm of shaking to an OD_{600} of 0.1. The SSD, a known anti-inflammatory ingredient, was chosen as a comparative material. Various concentrations of Ag/PVA/PTBAM nanofibers and SSD (from 1 to 25 μg/mL) were then added to the culture and then the OD_{600} was measured over time for observing the antibacterial performance.

2.3.2.4 Minimum inhibitory concentration (MIC) test

The Ag/PVA/PTBAM nanofibers were dispersed in aqueous solution for the MIC test. Nanofibers of PMMA with embedded silver nanoparticles (Ag/PMMA) were fabricated according to a reported procedure and used as a control. An aqueous solution of $AgNO_3$ was also prepared and used for comparative tests. To obtain the concentration of silver in these prepared solutions, the samples were dissolved in aqua regia. After 24 h, the solutions were diluted 100-fold, and the concentrations of Ag were measured by inductively coupled plasma atomic emission spectrometry (ICP-AES). The minimum inhibitory concentration (MIC) test was performed according to a reported procedure. For the test, 5 mL of sterilized LB agar solutions were inoculated with each bacterium (*E. coli* or *S. aureus*) (1×10^5 to 1×10^6 CFU). Then, the prepared samples were added to the bacteria

suspensions at different concentrations and incubated at 37 °C while shaking at 200 rpm. After 24 h, fresh organisms were reinoculated and incubated for an additional 24 h. Growth or nogrowth was determined by visual inspection. For accuracy of the results, all of the concentration values were analyzed three times and averaged. The standard deviation was less than 5%.

2.4 Instrumental

Photographs of transmission electron microscopy (TEM) were obtained with a Carl Zeiss LIBRA 120 at acceleration voltage for TEM was 120 kV. In the sample preparation, the samples were cast onto a copper grid after dilution in aqueous solution. Field-emission scanning electron microscopy (FE-SEM) images were obtained using a JEOL 6710 at an acceleration voltage of 10 kV. In the sample preparation, the samples were diluted in distilled water or ethanol and cast onto copper grid. Fourier transform infrared (FTIR) spectra were recorded on a Bomem MB 100 spectrometer (Quebec, Canada) in the absorption mode at a resolution of 4 cm^{-1} and 32 scans. The UV-vis spectra were taken at 25 °C with a Perkin-Elmer Lambda-20 spectrometer. Energy dispersive X-ray (EDX) analysis was performed by a Philips CM-20 microscope

coupled with an EDX facility. X-ray photoelectron spectroscopy (XPS) data was obtained using Sigma Probe electron spectroscope. Thermogravimetric analysis (TGA) was carried out in air using a TGA 2050 analyzer (TA Instruments). The weight loss of silver/ polymer nanomaterials was measured from ambient temperature up to 800 °C, at the rate of 10 °C/min to determine the inorganic content. X-ray diffraction (XRD) analysis was performed by Bruker GADDS (Germany) with General Area Detector Diffraction System (1.5406 nm of X-ray source). Inductively coupled plasma (ICP) analysis was performed with an ICPS-7500 (Shimdzu, Japan).

3. Results and Discussions

3.1. Fabrication of size-controllable Ag@AgCl plasmonic nanoparticles through aqueous system as visible-light plasmonic photocatalysts

3.1.1 Fabrication of AgCl nanoparticles

3.1.1.1 Synthetic procedure of AgCl nanocubes using poly(vinyl alcohol) as stabilizer

The silver halides were synthesized *via* precipitation reaction between the silver ion and halide ion precursors. In general, because the precipitation reaction is very fast, the use of stabilizer is inevitable for size control of the silver halide at the nanoscale. The PVA can serve as stabilizer in the formation of the AgCl nanoparticles. The PVA forms complex with Ag^+ ions in aqueous solution because of its hydroxyl side groups [70,114]. When the chloride donor (i.e, NaCl or KCl) is added, the AgCl nanoparticles are fabricated at the reactive site of the complex where the silver cations exist. In addition, the hydroxyl side groups of PVA can facilitate the adsorption of PVA onto the surface of the obtained AgCl and protect them from agglomeration during the precipitation reaction. **Figure 4** presents FE-SEM images of three as-prepared

samples that were synthesized at different molar ratio of PVA (calculated in terms of the repeating unit) to $AgNO_3$ (from 0.1 to 10), in which the PVA had the molecular weight of 146000-186000, and the synthesis was performed at 40 °C. The nanoparticles had a cubic-shape with blunted edges at the molar ratio of PVA to $AgNO_3$ was 0.1; they evolved into nanocubes with clear edges when the molar ratio of PVA to $AgNO_3$ increased to 10. Notably, the size and its distribution of the nanocubes were decreased with increasing amount of PVA, and this observation can be attributed to the stabilizing effect of the PVA. The products did not show significant change in size and the uniformity when the molar ratio increased above 10 (even to 500); it seems saturation concentration of the polymeric stabilizer on the surface of the AgCl. When the reaction was conducted in the absence of PVA, the solution appeared opaque and milky within 10 s. Micrometer-sized AgCl particles with irregular shapes formed during this rapid reaction (**Figure 5**). The particles were agglomerated and precipitated after the 1 h of reduction with L-arginine. It is clear from these results that PVA played a pivotal role not only in the formation of the AgCl nanocubes by stabilizing the precursor ions but also in the formation of Ag@AgCl nanoparticles by preventing the agglomeration of AgCl particles during the reduction.

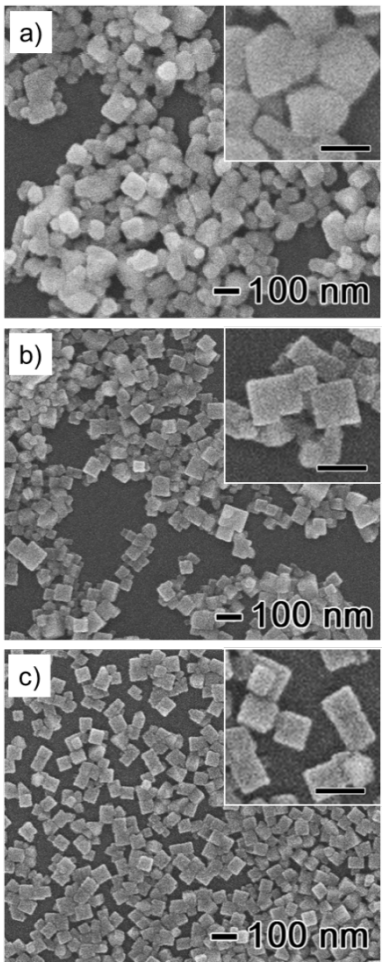

Figure 4. FE-SEM images of the AgCl nanoparticles prepared at different molar ratio of PVA to $AgNO_3$: (a) 0.1, (b) 1, and (c) 10. The PVA had the molecular weight of 146000-186000, and the synthesis was performed at 40 °C. The insets show the magnified images of each product and the scale bars in the inset images are 100 nm.

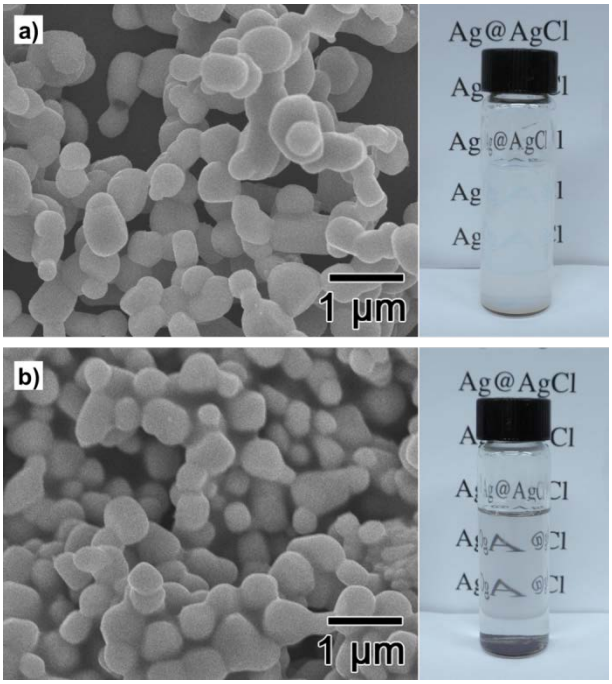

Figure 5. FE-SEM images of the (a) bulk AgCl and (b) bulk Ag@AgCl prepared under the same condition as in **Figure** 4b except for the addition of PVA stabilizer. The inserted photographs show the as-prepared solution of bulk AgCl (upper right) and bulk Ag@AgCl (bottom right). The bulk Ag@AgCl was prepared *via* reduction of bulk AgCl with L-arginine for 1 h.

3.1.1.2 Size-control of AgCl by varying reaction temperature

Figure 6 shows FE-SEM images of the AgCl nanoparticles synthesized under different reaction temperatures. The inset images at higher magnifications show that the particles had a cube-shaped morphology. The average edge length of the resulting nanocubes increased (from ~57 to ~170 nm) as the reaction temperature increased from 25 to 90°C. The size distribution of the products also broadened as the reaction temperature increased (**Figure 7**). At high temperatures, the mobility of the polymer chains and the entropy term of the reaction system increased. The degree of freedom of the Ag^{+} and Cl^{-} ions also increased with increasing reaction temperature [129]. Consequently, the particle size increased and its distribution broadened with increasing temperature.

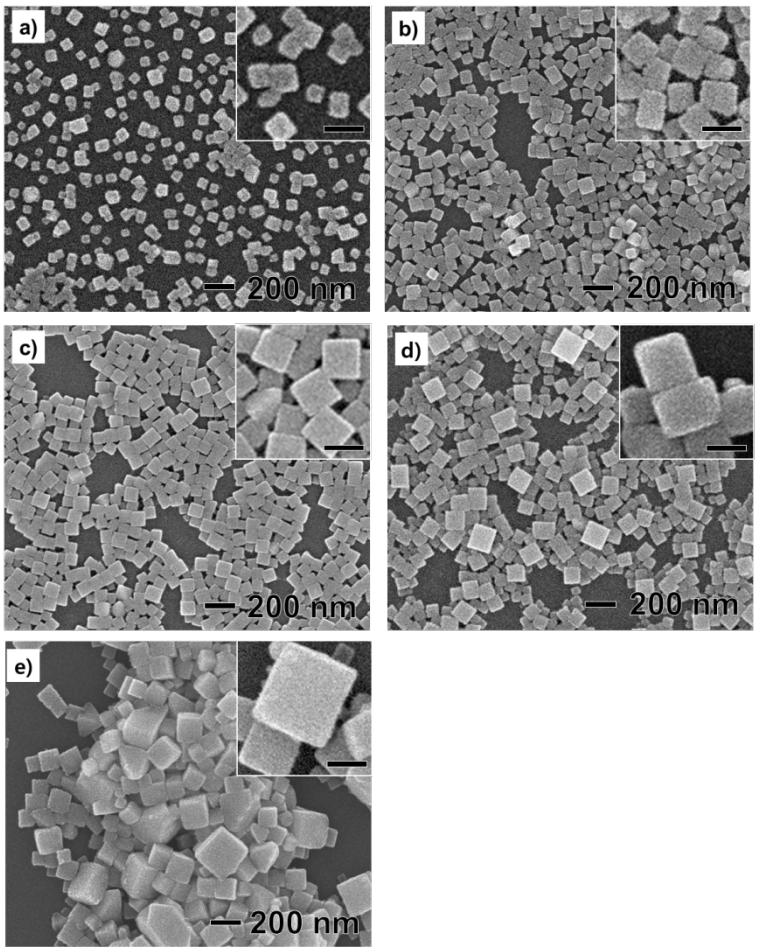

Figure 6. FE-SEM images of the AgCl nanocubes prepared at reaction temperatures of (a) 25, (b) 40, (c) 70, (d) 80, and (e) 90°C. (Inset of a-e) FE-SEM images of each product at higher magnifications; the scale bar in the inset images is 100 nm. The reactions were conducted in aqueous solution for 30 min with PVA as a stabilizer.

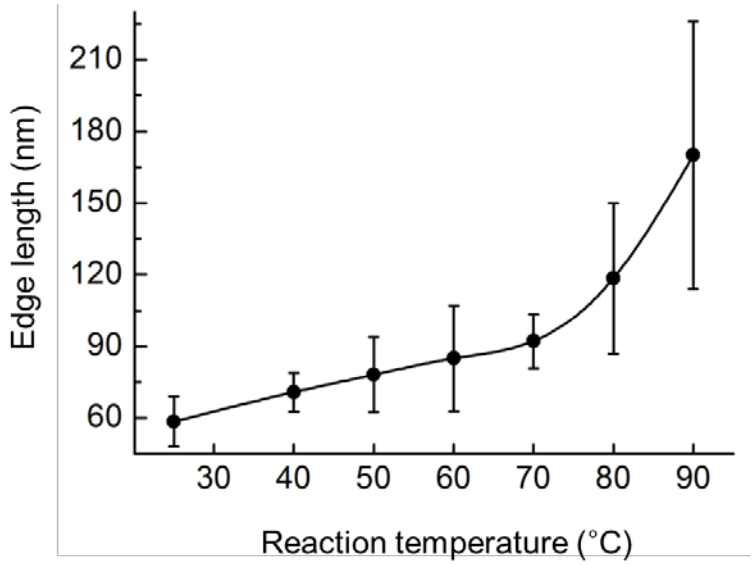

Figure 7. Variation of average edge length of AgCl nanocubes as a function of reaction temperature.

3.1.2 Systematic investigation of partial reduction of AgCl nanoparticles

3.1.2.1 Characterization of Ag@AgCl nanoparticles

The synthesized AgCl nanocubes were reduced by L-arginine to form metallic Ag nanoparticles on the AgCl surface. L-arginine is a mild reducing agent and, when added to the AgCl solution, allowed partial reduction of the as-prepared AgCl nanocubes. The extent of reduction of the AgCl as a function of the reaction time was obtained by energy-dispersive X-ray spectroscopy (EDX) (**Table 2**). EDX analysis can provide the elementary composition of the prepared samples. As the reduction proceeded, the atomic percentage of Ag increased and that of chlorine decreased because the AgCl was reduced to metallic silver during the reaction. The atomic ratio of Ag to AgCl increased from 0 to 1.60 during the 24-h reduction period, after which time ~61% of the Ag^{+} from AgCl had been reduced to Ag^{0}. The formation of AgCl nanoparticles and the evolution of silver clusters on the AgCl nanoparticles were confirmed by X-ray diffraction (XRD) (**Figure 8**). The patterns of the as-prepared AgCl nanocubes matched well with the standard peaks of AgCl (JCPDS file: 31-1238). With increasing reduction time, three diffraction peaks at 38.0, 43.9, and 64.4° appeared and gradually increased in intensity; these peaks corresponded to

metallic silver on the AgCl nanoparticles (JCPDS file: 65-2871).

Table 2. Variation of atomic% of Ag and Cl on the synthesized Ag@AgCl nanoparticles with different reduction times.

Reduction time	Atomic% of Ag	Atomic% of Cl	Atomic ratio, Ag:Cl	Atomic ratio, Ag:AgCl[a]	Reduction % of Ag[b]
0 h	50.15	49.85	1.01	0.006	0.6
1 h	51.26	48.74	1.05	0.052	4.92
2 h	53.02	46.98	1.13	0.129	11.4
4 h	55.86	44.14	1.27	0.265	20.98
6 h	59.64	40.36	1.48	0.478	32.33
8 h	62.45	37.55	1.66	0.663	39.87
10 h	64.64	35.36	1.83	0.828	45.3
18 h	66.86	33.14	2.02	1.017	50.43
24 h	72.19	27.81	2.60	1.600	61.48

[a] Values of the atomic ratio of Ag : AgCl were calculated as atomic ratio of Ag : AgCl = (A − B)/B (where A is the atomic % of Ag and B is the atomic % of Cl).

[b] Values of reduction % of Ag were calculated as reduction % of Ag = (A − B)/A.

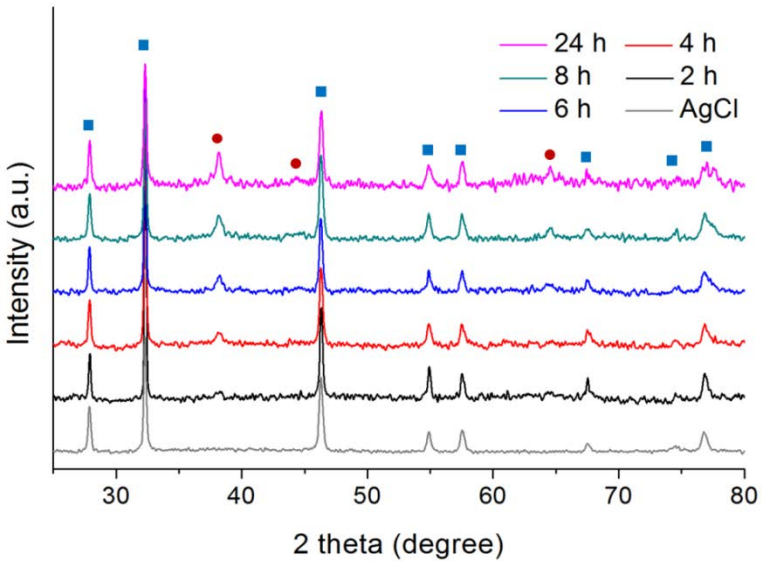

Figure 8. XRD patterns of the Ag@AgCl nanoparticles prepared with various reduction time at 25 °C. Squares and spheres represent the characteristic peaks of the AgCl and metallic Ag, respectively.

3.1.2.2 Time-dependent observation of reduction of AgCl nanoparticles

As shown in **Figure 9**, the optical properties of the Ag@AgCl nanoparticles were monitored during the reduction process by recording the UV-visible absorption spectra of the sample solutions at different times. The experiments were performed for the AgCl nanocubes having an edge length of ~57 nm. The dispersion of the original AgCl nanocubes was translucent (**Figure 10**) and absorbed at ~260 nm, which corresponded to the large AgCl bandgap (**Figure 11**) [130]. Initially, no peak was observed in the visible region. After 2 h of reduction, absorption peaks clearly appeared at 394 and 460 nm. Partial reduction of AgCl resulted in an absorption peak at ~400 nm that corresponded to the well-known SPR band of silver nanoparticles [131]. The strong plasmonic band appeared at ~460 nm. The increasing refractive index of the substrate caused a red-shift of the light absorption. For the Ag nanoclusters on AgCl nanocubes, the absorption was red-shifted by ~70 nm because the refractive index of the AgCl (2.01) is higher than that of water (1.32). As a result, the new plasmonic band appeared at a longer wavelength [132,133]. The size and shape of the formed Ag clusters also can lead to red-shifted absorption [134]. The intensity of the absorption peak of the as-prepared nanoparticles increased with increasing

reduction time over a period of 1–8 h (**Figure 9a**). More metallic Ag nanoclusters formed and grew on the surface of the AgCl substrate during the continuous reduction process, and thus the absorbance intensity of the Ag@AgCl nanoparticles increased. The split bands united into one broad absorption peak at ~445 nm as the reduction proceeded to 10 h, indicating that the Ag clusters that had formed on the AgCl surface had grown and coalesced into larger Ag crystals [135]. Additionally, the major absorption peak of the sample was blue-shifted from ~470 to ~430 nm during the 24-h reduction period (**Figure 9b**). Excessive reduction of the AgCl may have occurred to form Ag nanoparticles (or metallic Ag-covered AgCl nanoparticles). The solution color gradually turned from gray to yellow (2 h), red-orange (4 h), reddish brown (8 h), and dark brown (24 h) as reduction took place, indicating growth of the size of the metallic Ag (**Figure 10**).

The morphological change of the Ag@AgCl nanoparticles in the course of the reduction process was also investigated by recording FE-SEM images at different times. At the beginning of the reduction period (i.e., < 1 h), the as-prepared samples maintained their intrinsic cubic morphology and some had nodules on their surfaces; these nodules are thought to be reduced metallic Ag nanoparticles (**Figure 12a**). As the

reduction proceeded, the samples gradually lost their cubic morphology and became nanoparticles with rounded corners (after 4 h, **Figure 12b**) and finally became roundish nanoparticles (after 24 h, **Figure 12c**). Although the synthesized particles lost their intrinsic cubic shape, they did not significantly aggregate during the reduction, and became slightly smaller, which may have originated from loss of chloride during the reduction process. This result matched well with the blue-shifted UV-visible absorption spectrum of the products. Unfortunately, transmission electron microscopic image cannot be clearly obtained because exposing the Ag@AgCl particles to an electron beam with high current density cause the reduction of the AgCl to metallic Ag. The spatial distribution of the metallic Ag on the AgCl surface is not fully understood, but it was supposed that the metallic Ag grew over 1–10 h of reduction after which time it had fully covered the surface of the AgCl as illustrated in **Figure 13**. The union phenomena of the UV-vis peaks can support the assumption. Further reduction may have occurred at the interior of the Ag^0-covered AgCl nanoparticles at reduction times exceeding 10 h.

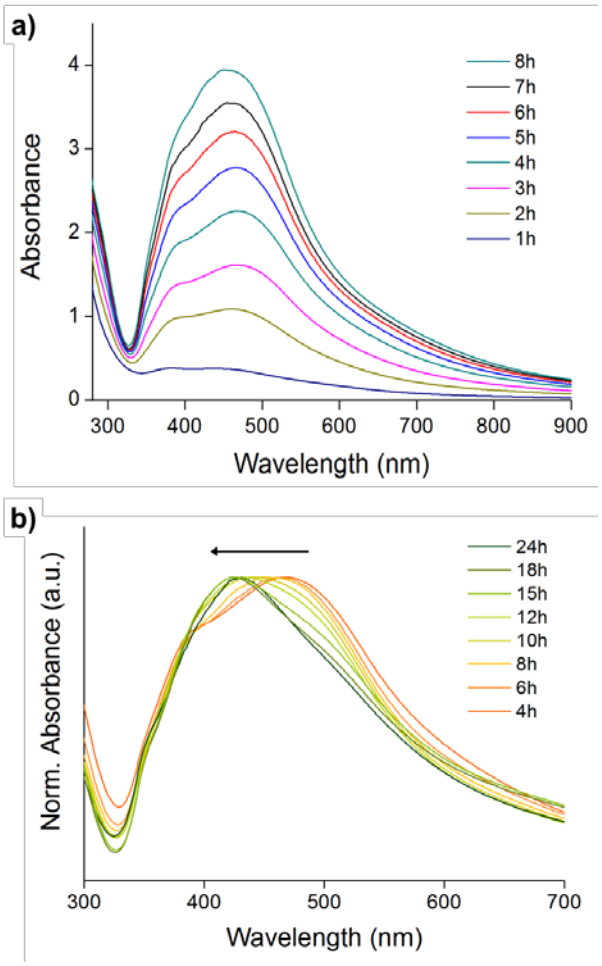

Figure 9. UV-visible absorbance spectra of the as-prepared Ag@AgCl dispersions at different reduction times (a) without normalization and (b) normalized against the intensity of the major peaks.

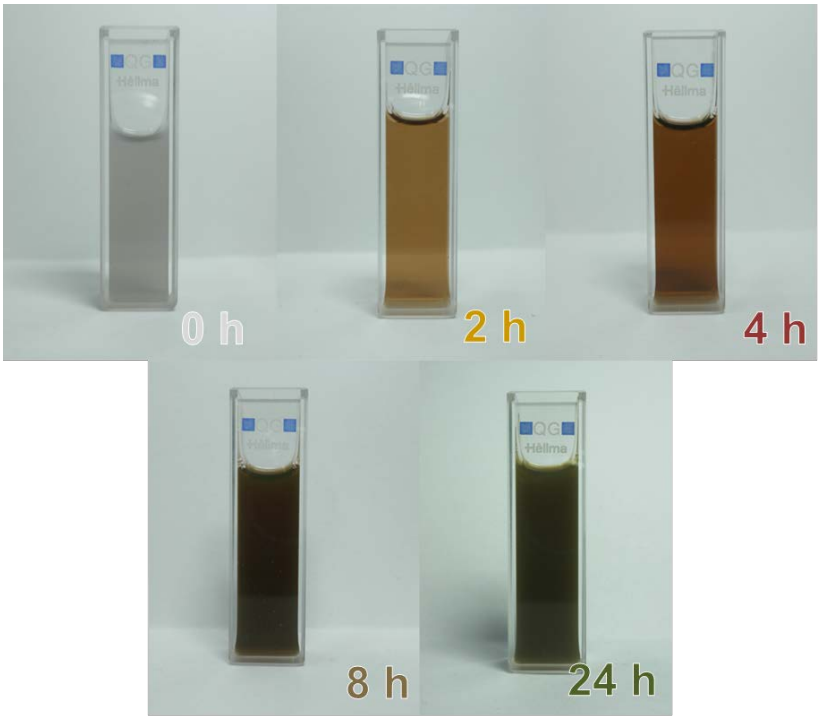

Figure 10. Photographs of the as-prepared Ag@AgCl suspensions synthesized at different reduction times. From left to right: 0, 2, 4, 8, and 24 h.

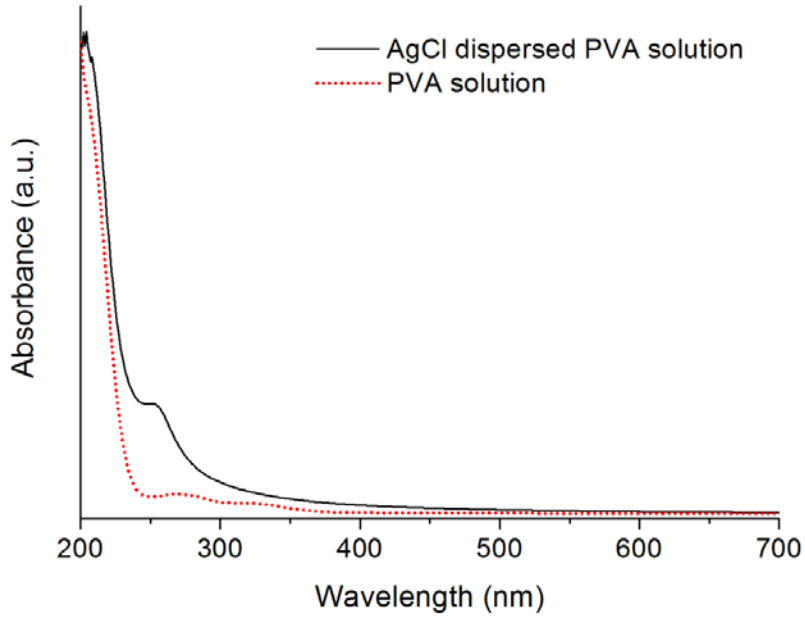

Figure 11. UV-vis spectra of the as-prepared AgCl dispersed PVA solution (black solid line) and the as-prepared PVA solution (red dot line).

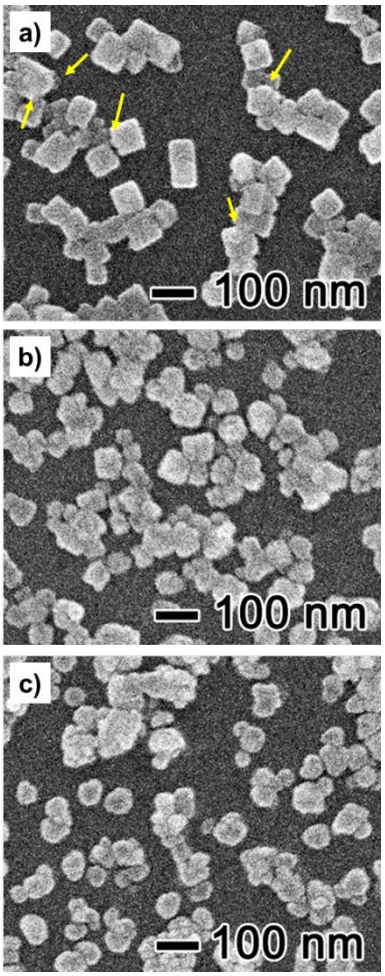

Figure 12. FE-SEM images of the Ag@AgCl nanoparticles prepared at different reduction times: (a) 1, (b) 4, and (f) 24 h. The arrows in (d) indicate nodules on the cubic surfaces. The reactions were conducted in aqueous solution at 25°C with PVA as a stabilizer.

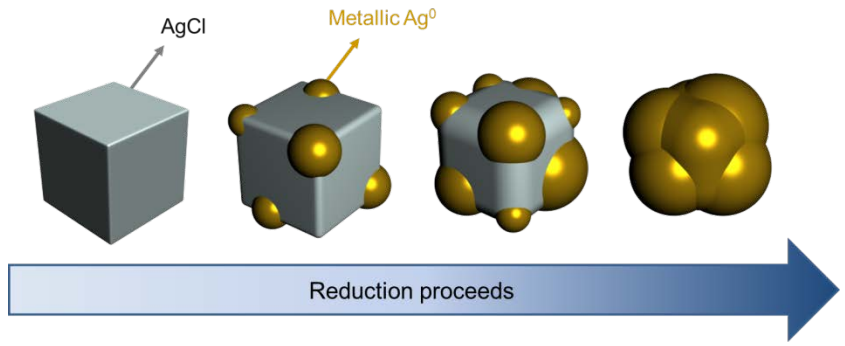

Figure 13. Schematic illustration of the plausible morphological change of the Ag@AgCl during the reduction procedure. The metallic Ag^0 clusters were formed on the AgCl surface through mild reduction process and these Ag^0 gradually grown bigger and finally cover over the surface of the AgCl nanoparticles.

3.1.2.3 The effect of AgCl size in the light absorption properties of Ag@AgCl nanoparticles

In order to confirm the relation between the substrate size and the light observation properties, the different sized AgCl nanocubes were prepared by varying the reaction temperature and the each AgCl was partially reduced to Ag@AgCl nanocomposite under same reduction condition. The color of the as-prepared sample solution turns to reddish brown (~57 nm sized AgCl substrate), red purple (~61 nm) or violet (~87 nm) after the reduction takes place by L-arginine (**Figure 14**). UV-vis spectra and the FE-SEM images of the Ag@AgCl nanocomposites are shown in **Figure 15** and **Figure 16**, respectively. As shown in the FE-SEM images (**Figure 16a-c**), the AgCl nanocubes become roundish cubes with nodules (may be metallic Ag) on their edges after the reduction process. Additionally, the sample solutions showed the strong plasmonic absorption bands appear at around 500 nm region (**Figure 15**). Interestingly, the position of the maximum absorption wavelength (λ_{max}) was shifted from 460 to 510 nm with the increasing size of the AgCl substrates (from ~57 to ~87 nm). In general, the growing size of the Ag nanoparticles can result in the red-shifted absorption. However, the UV-vis spectra of the Ag@AgCl solution obtained at different reduction time

cannot support the growth of very large silver domains (**Figure 16**). Peng and Sun indicated that the absorption band of the AgCl gradually shifted to the red at a large degree (from ~400 to ~640nm) during the reduction process [45]. Notably, the size of the samples also gradually increased (from < 100 to ~760 nm) during the reduction because of the Ostwald ripening process under their experimental condition. These data supports the hypothesis that the red-shift of the λ_{max} position was attributed to not the size growth of metallic Ag but the size of the AgCl substrate (with high refractive index).

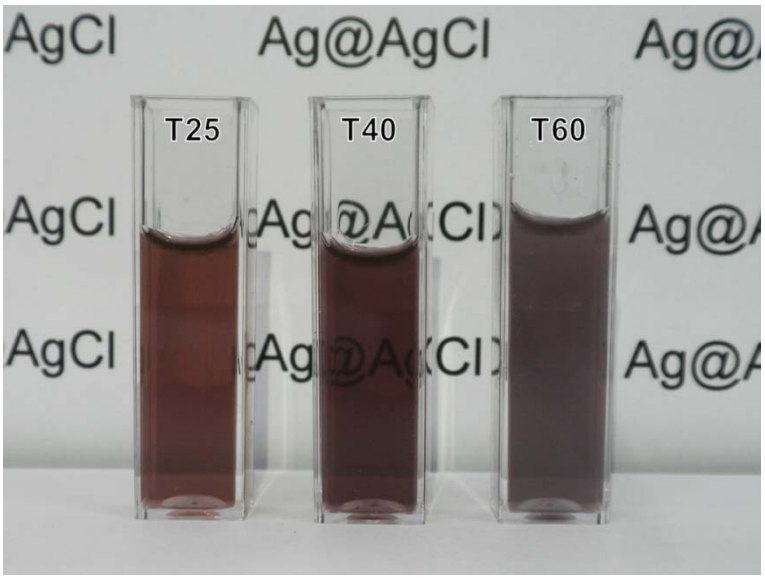

Figure 14. Photographs of the Ag@AgCl suspensions prepared via the partial reduction of the as-prepared AgCl nanocubes. The AgCl nanocubes with edge length of ~57 (T25), ~61(T40), and ~87 nm (T60) were synthesized at 25, 40, and 60 °C, respectively and reduced to Ag@AgCl nanocomposites using L-arginine at 25 °C.

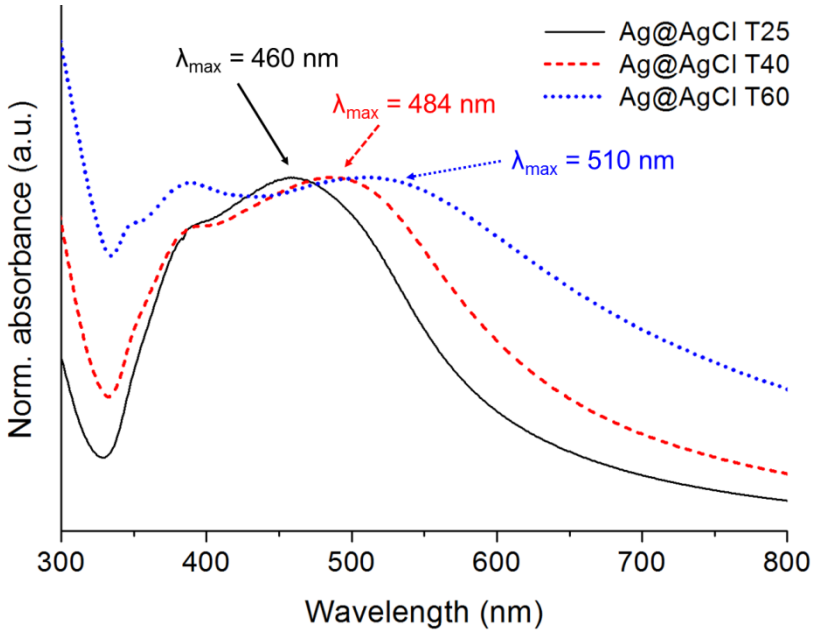

Figure 15. UV-visible absorbance spectra of the Ag@AgCl nanocomposites prepared *via* the partial reduction of the as-prepared AgCl nanocubes. The AgCl nanocubes with edge length of ~56, ~61, and ~87 nm were synthesized at 25, 40, and 60 °C, respectively and reduced to Ag@AgCl nanocomposites using L-arginine at 25 °C. The spectra are normalized against the intensity of major peaks.

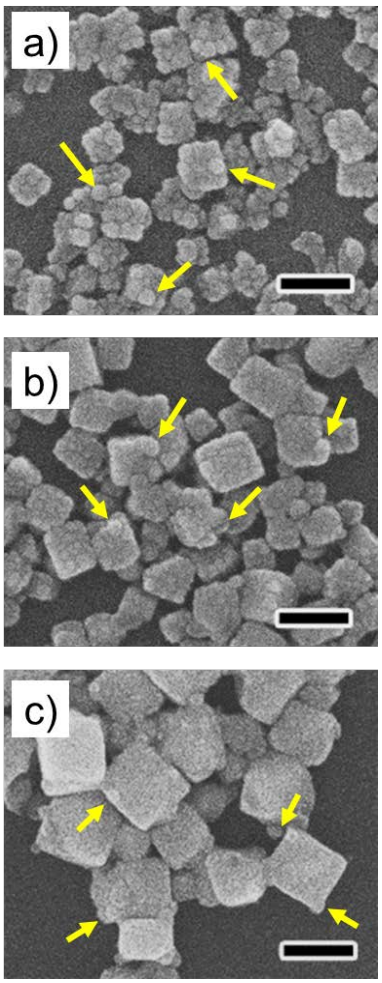

Figure 16. FE-SEM images of the Ag@AgCl nanocomposites prepared by reducing the (a) ~56, (b) ~61 and (c) ~87 nm sized AgCl substrate. The arrows in FE-SEM images indicate nodules (metallic Ag) on the cubic surfaces. The scale bars are 100 nm.

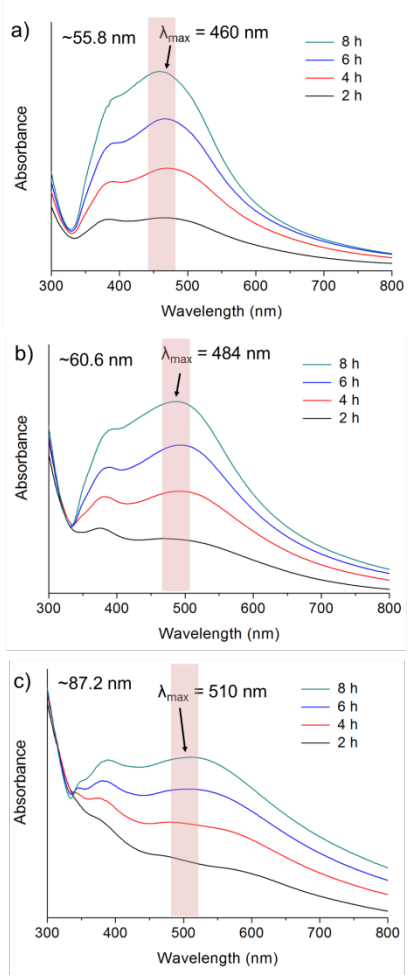

Figure 17. UV-visible absorbance spectra of the Ag@AgCl dispersion prepared via the partial reduction of the as-prepared AgCl nanocubes at different reduction times. The AgCl nanocubes synthesized at 25, 40, and 60 °C have different edge length of (a) ~57, (b) ~61, and (c) ~87 nm, respectively. The as-prepared AgCl nanocubes are reduced by L-arginine under same reduction condition.

3.1.3 Visible-light responsive photocatalytic properties of synthesized Ag@AgCl nanoparticles

The as-prepared Ag@AgCl nanoparticles were photocatalytically active in visible light because of the plasmon resonance property of the Ag nanoclusters on the surface of the AgCl. The photocatalytic activity was evaluated in terms of the decomposition of dyes. The degradation curves of methylene blue (MB) as a function of irradiation time by visible light ($\lambda > 400$ nm) are shown in **Figure 18**, in which C_0 is the concentration of MB at adsorption-desorption equilibrium and C is the concentration at a given irradiation time. The AgCl nanocubes (without metallic Ag) were not photocatalytically active. This confirmed that the Ag nanoclusters on the AgCl played an essential role in the photocatalysis mechanism. The photocatalytic efficiency of the Ag@AgCl nanocomposite increased with increasing reduction time (≤ 8 h). The Ag^0 content also increased with increasing reduction time, leading to higher SPR intensity of the silver and thus increasing the photocatalytic efficiency of the Ag@AgCl. Under visible light irradiation, the metallic Ag of the Ag@AgCl composite produces photogenerated electron-hole, which was separated by the SPR-induced local electromagnetic field. The electrons move to the Ag nanoparticles,

whereas holes move to the AgCl. The electrons could react with adsorbed O_2 to form reactive oxygen species, and the holes could react with Cl^- ions of AgCl to form Cl^0 atoms, which could both degrade organic pollutants (**Figure 19**) [87]. After the dye molecules have been decomposed, Cl^0 can return to chloride ion form again.22 When the Ag^0 covered the surface of the AgCl, the dye degradation through AgCl part can be disturbed. Then, the photocatalytic efficiency of the Ag@AgCl decreased because the metallic silver itself do not show photocatalytic activity. The photocatalytic efficiency drastically decreased after 10 h of reduction (reduction % of Ag > ~45.3%, **Table 2**). I think that the metallic Ag covered the surface of AgCl after 10 h of reduction. The relationship between the size of the nanophotocatalyst and the photocatalytic activity was investigated. As a result, the photocatalytic activity of the Ag@AgCl nanocomposites was in the following order: T25 ≥ T40 > T60 (**Figure 20**). The photocatalytic efficiency increased with decreasing the size of the Ag@AgCl nanophotocatalyst. The smaller nanoparticles provided more sites for decomposing the contacted dye molecules, enhancing the photocatalytic activity. In addition, various factors such as the content of metallic Ag, SPR property, and light absorption region may affect to the dye decomposing efficiency of the

synthesized plasmonic photocatalyst. To confirm the stability of the synthesized Ag@AgCl nanoparticles, photocatalytic reaction tests were repeatedly performed against MB, MO, and RhB dyes under visible light irradiation (**Figure 21**). The test was performed with the 8-h-reduced Ag@AgCl nanoparticles, which had the best photocatalytic performance under this experimental condition. After the organic dyes decomposed, the suspension was centrifuged to separate the Ag@AgCl nanoparticles; these could be recovered to catalyze a new reaction. The Ag@AgCl nanoparticles decomposed all of the test dyes in visible light. Additionally, the as-prepared photocatalyst preserved its plasmonic photocatalytic activity after four experimental cycles, regardless of the type of dye. The samples maintained their intrinsic shape without significant change after the photocatalytic test. Photon from visible light irradiation could be absorbed by the metallic Ag because of its SPR. The electron separated from the photon remains in the metallic Ag rather than being transferred to the Ag+ ions of the AgCl lattice. In addition, as mentioned above, the hole reacted with Cl^- ions of AgCl to form Cl^0 atoms and the Cl^0 could return to Cl^- ions again after the dye degradation. Therefore, the Ag@AgCl nanocomposite could maintain its photocatalytic activity during repeated dye decomposing test.

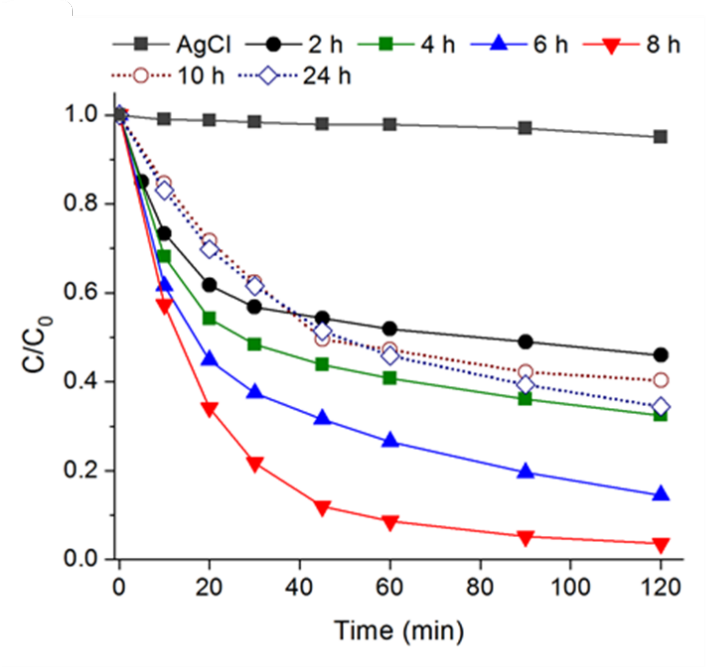

Figure 18. Photocatalytic degradation of MB over different Ag@AgCl nanoparticles prepared with various reduction times.

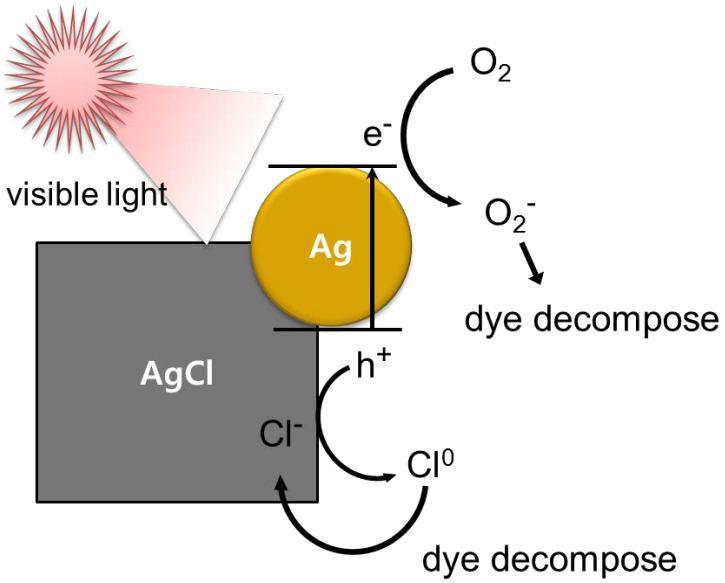

Figure 19. Scheme of the proposed plasmonic photocatalytic mechanism of the Ag-decorated AgCl nanocomposite.

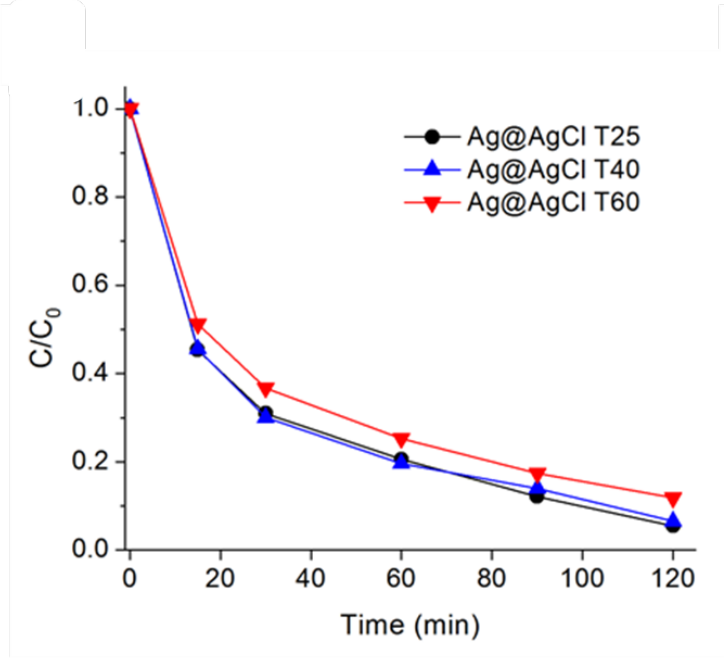

Figure 20. Photocatalytic degradation of MB over different Ag@AgCl nanoparticles prepared with the different sized AgCl substrates.

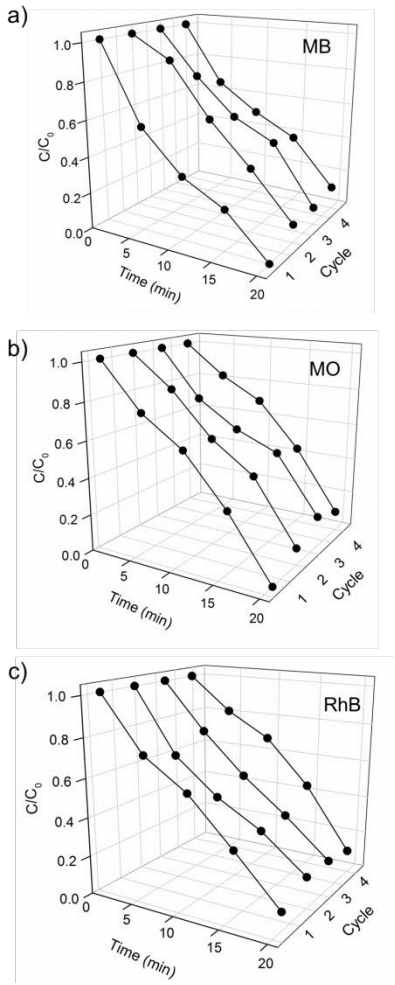

Figure 21. Photocatalytic degradation of (a) MB, (b) MO, and (c) RhB dyes over Ag@AgCl T25 nanoparticles. The photocatalytic experiments were done under visible light (> 400 nm) irradiation and the cycling test was performed using the 8 h reduced samples. The photocatalytic efficiency (%) was calculated based on the first degradation data.

3.2 Fabrication of Ag@AgBr photocatalytic nanoparticles in aqueous system with PVA stabilizer

3.2.1 Fabrication of AgBr nanoparticles with poly(vinyl alcohol) stabilizing system

The synthesis of Ag@AgBr proceeded in a way similar to the system of Ag@AgCl nanoparticles. The AgBr nanocubes were obtained when the molar ratio of PVA (MW 146,000-186,000) to Ag precursor was adjusted to 100. The FE-SEM image revealed that the AgBr nanoparticles had a uniform size of ~72 nm without any significant agglomeration when the reaction was conducted at 25 °C (**Figure 22**).

They lost their structural uniformity and the size-distribution was broaden when the PVA content decreased (**Figure** 23). In addition, when the precipitation reaction performed without PVA stabilizer, micrometer-sized AgBr particles with irregular shapewere obtained (**Figure 24**). From these results, it is clear that PVA plays a pivotal role in the formation of the uniform AgBr nanoparticles during the precipitation reaction.

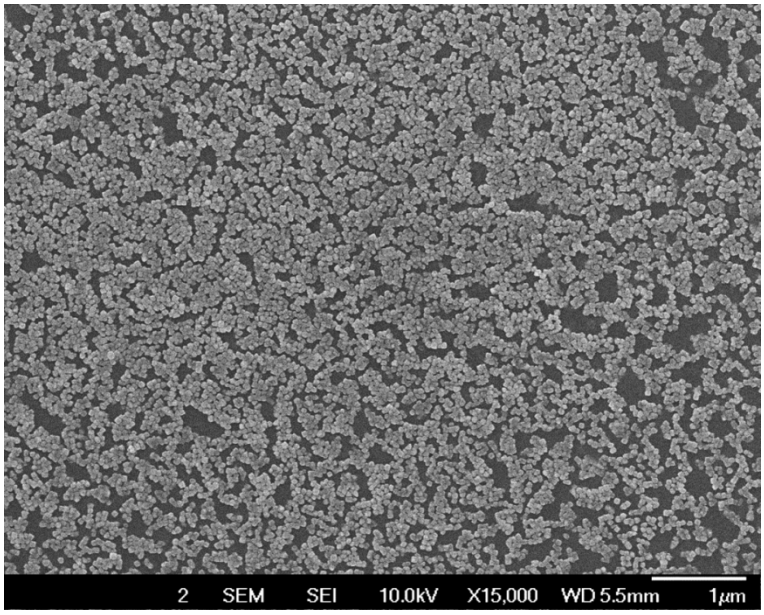

Figure 22. Low-magnification FE-SEM images of the synthesized AgBr nanoparticles.

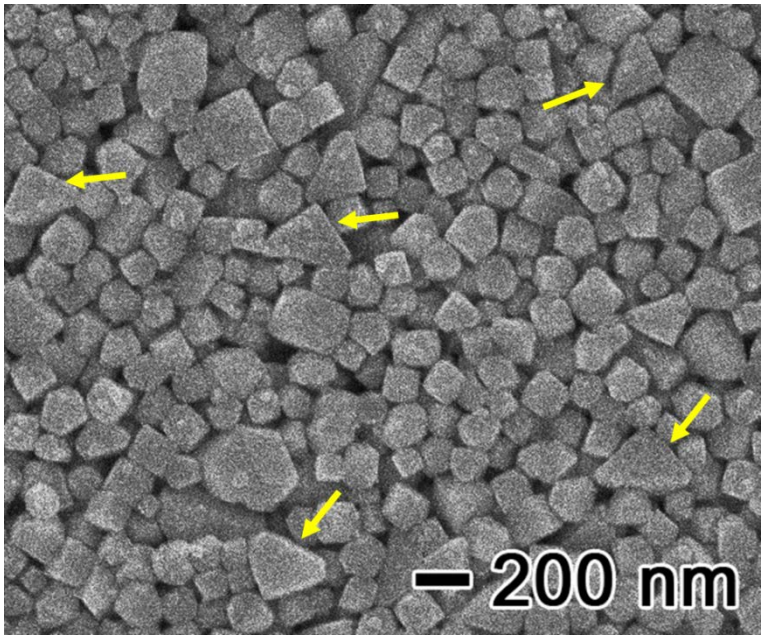

Figure 23. FE-SEM images of the AgBr nanoparticles prepared with low concentration of PVA (molar ratio to silver precursor is 50). The arrows indicate the trigonal prism shaped AgBr.

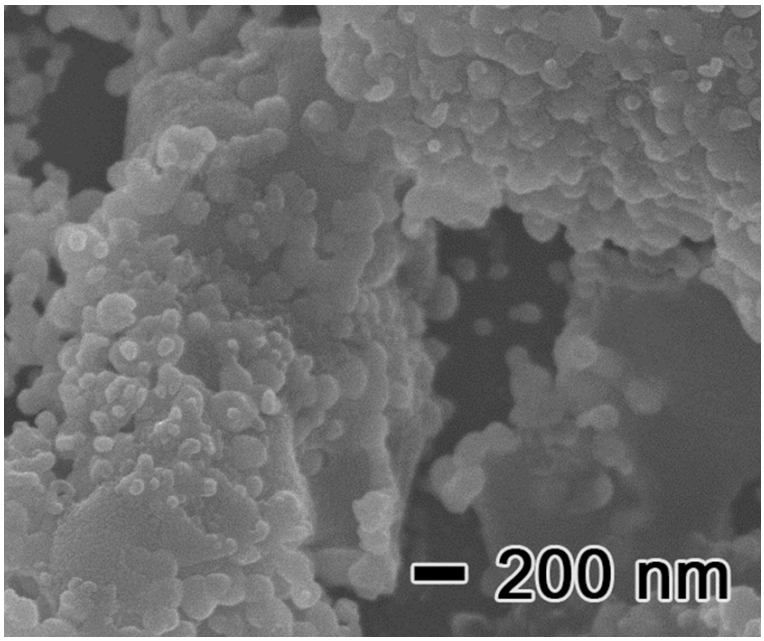

Figure 24. FE-SEM images of the AgBr prepared by precipitation reaction between $AgNO_3$ and NaBr in aqueous solution without the PVA stabilizer.

3.2.2 Size-control of AgBr nanoparitcles

Figure 25 presents field-emission scanning electron microscope (FE-SEM) images of three as-prepared samples that were synthesized at different reaction temperature (25, 40, and 60 °C), in which the PVA had the molecular weight of 146000-186000 and the molar ratio of PVA to Ag precursor was adjusted to 100. The inset images at higher magnifications show that the synthesized AgBr had a cube-shaped morphology. The edge length of the AgBr nanocubes was increased from ~72 to ~183 nm as increasing the reaction temperature (from 25 to 60 °C). Both the particle size and its distribution of the resulting AgBr increase as the reaction temperature increases. The mobility of polymeric chain and degree of freedom of the silver and halide ions increase at the high temperature. Consequently, the size of the AgBr nanocubes can be controlled by varying the reaction temperature. **Table 3** summarizes the obtained silver halides (AgCl and AgBr) under various experimental conditions, including the molecular weight of PVA, the molar ratio of PVA to the silver precursor, and reaction temperature. Overall, the molecular weight of the polymer did not significantly affect to the size of the products in this experimental condition. On the other hand, both the size and its distribution of the resulting silver halides increase as the reaction temperature increases because of the mobility of polymeric chain and degree of freedom of the silver and halide ions increase at the high temperature [129].

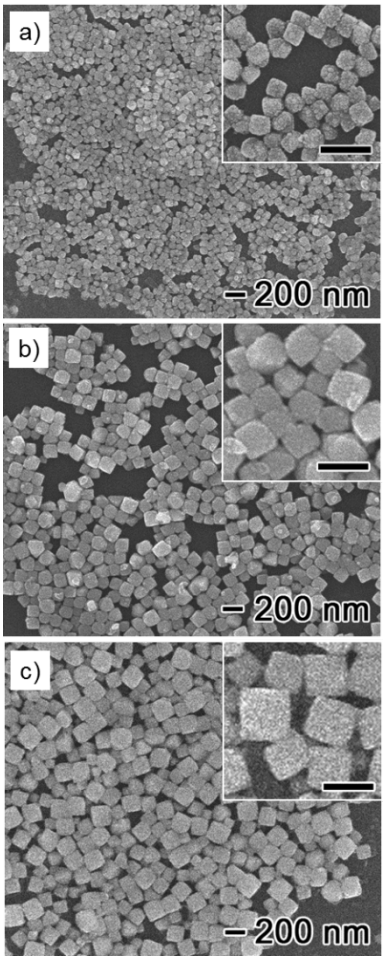

Figure 25. FE-SEM images of the AgBr nanocubes prepared at different reaction temperature: (a) 25, (b) 40, and (c) 60 °C. The insets show the magnified images of each product and the scale bars in the inset images are 200 nm.

Table 3. Summary of silver halides synthesized under different experimental conditions.

Halogen precursor	MW of PVA	Molar ratio, PVA:silver precursor	Reaction temperature	Average edge length (nm)
NaCl	146,000	25:1	40	61.1 ± 10.1
	146,000	10:1	25	55.8 ± 9.4
	146,000	10:1	40	60.6 ± 11.2
	146,000	10:1	60	87.2 ± 42.5
	146,000	1:1	40	65.0 ± 18.1
	146,000	0.1:1	40	83.8 ± 27.2
	31,000	25:1	40	61.0 ± 15.9
	9,000	25:1	40	63.3 ± 14.1
NaBr	146,000	100:1	25	71.5 ± 6.08
	146,000	100:1	40	134.3 ± 13.4
	146,000	100:1	60	183.3 ± 20.1
	9,000	100:1	40	133.9 ± 21.5

3.2.3 Synthesis and characterization of Ag@AgBr nanocomposites

3.2.3.1 Microscopic observation of the Ag@AgBr nanoparticles

The as-prepared AgBr nanocubes were partially reduced by L-arginine at 25 °C under laboratory light condition and the Ag@AgBr nanocomposites were formed. As shown in **Figure 26**, after the partial reduction, the nano-nodules (metallic Ag) were grown on the surface of the AgBr nanocubes. Additionally, the Ag@AgBr increased in size from ~72, ~134, and ~183 nm to ~176, ~240, and ~370 nm, respectively (with a deviation of ~10%) during the reduction process. Ostwald ripening process could be occurred during the reaction due to the non-uniform size distribution of the AgBr substrates. The each solution color turns to dark purple (Ag@AgBr T25), purple (Ag@AgBr T40) and salmon pink (Ag@AgBr T60) after the reduction. The extents of reduction of the AgBr were obtained by EDX analysis (**Table 4**). After the reduction reaction, the atomic percentage of Ag increased and that of brome decreased because the AgBr provide the precursor of the metallic silver during the reduction.

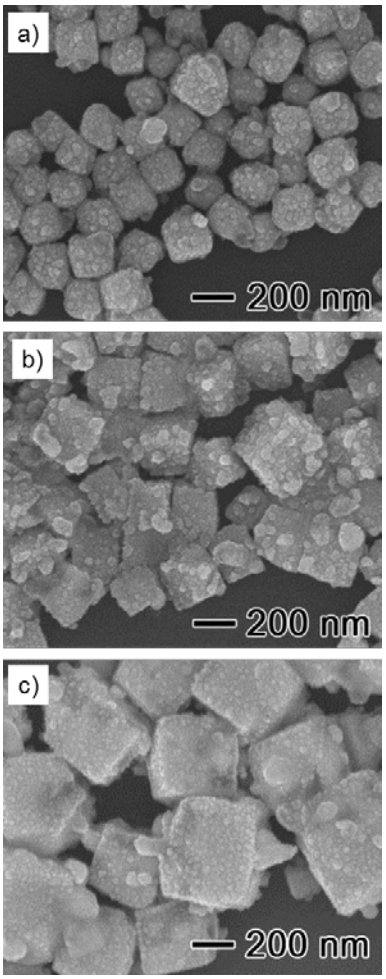

Figure 26. FE-SEM images of the Ag@AgBr nanocomposites synthesized by reducing the as-prepared AgBr nanocubes. The reduction was conducted using the AgBr nanocubes prepared at different reaction temperature: (a) 25, (b) 40, and (c) 60 °C. The spectra are normalized against the intensity of major peaks.

Table 4. Atomic% of Ag and Br on the synthesized Ag@AgBr nanoparticles.

Sample	Atomic% of Ag	Atomic% of Br	Atomic ratio, Ag:AgBr	Reduction% of Ag
Ag@AgBr T25	52.4	47.6	0.101	9.16
Ag@AgBr T40	51.9	48.1	0.079	7.32
Ag@AgBr T60	52.1	47.9	0.088	8.06

3.2.3.2 Spectroscopic observation of Ag@AgBr nanoparticles

The XRD pattern of prepared Ag@AgBr nanoparticles (**Figure 27**) obviously presents the additional peaks at 38.0 compared with that of the pristine AgBr nanocubes. This peak matched well with the standard peaks of the metallic silver, indicating that the Ag nanoparticles were formed on the AgBr surface after the partial reduction. The intensity of Ag metal peak is so weak in the XRD patterns, possibly because the poor crystallinity of the metallic Ag on the surface of AgBr particles.

The elemental composition and chemical states of Ag@AgBr samples were further verified by X-ray photoelectron spectroscopy (XPS), and as a result, silver, bromine, carbon and oxygen species were detected (**Figure 28**). The measurement was conducted with a representative Ag@AgBr T40 samples. The carbon (C 1s) and oxygen (O 1s) peaks could be originated from the residual PVA stabilizer. The high-resolution Br 3d and Ag 3d spectrum of a sample is shown in **Figure 28b** and **Figure 28c**, respectively. The sample had the binding energy of 67.7 and 68.8 eV, which corresponding to Br $3d_{5/2}$ and Br $3d_{3/2}$, respectively, in agreement with the reported value for AgBr [136]. The Ag 3d spectrum of the Ag@AgBr T40 sample consist of two peaks at 367.3 and 373.4 eV correspond to the binding energies of Ag $3d_{5/2}$ and

Ag $3d_{3/2}$, respectively. Each two peak can be further deconvoluted into two peaks; peak at 367.3 eV was deconvoluted into peaks located at 367.3 and 367.9 eV, while peak at 373.4 eV can be deconveoluted to peaks at 373.4 and 373.9 eV. The peaks at 367.3 and 373.4 eV are for Ag^+ ion of AgBr, while the peaks at 367.9 and 373.9 eV are attributed to metallic Ag^0 [136]. The ratio of Ag to AgBr (Ag^+ ion) was calculated to be 0.147, which is similar to the ratio value obtained by EDX analysis.

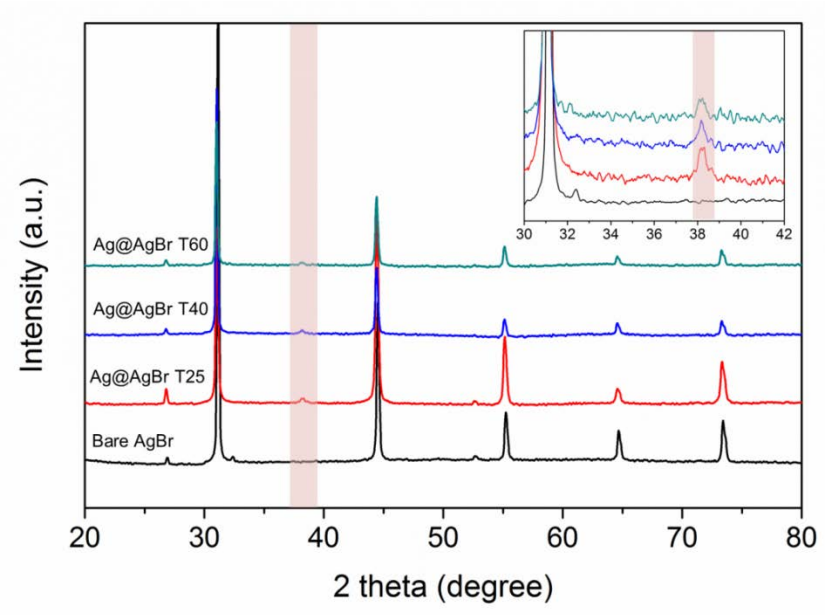

Figure 27. XRD patterns of as-prepared AgBr@Ag and bare AgBr samples. The inset image shows the magnified XRD patterns.

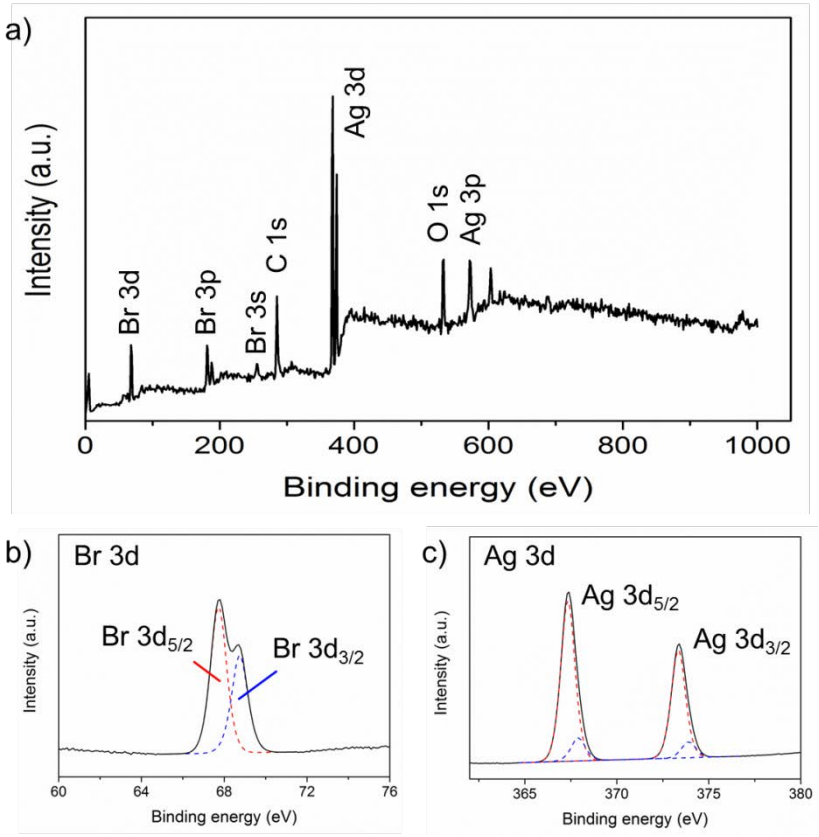

Figure 28. (a) XPS survey spectra and high-resolution spectra of (b) Br 3d and (c) Ag 3d spectra of Ag@AgBr samples. The XPS spectra were obtained using a representative Ag@AgBr T40 sample.

3.2.3.3 The effect of AgBr size in the light absorption properties of Ag@AgBr nanoparticles

As shown in the UV-vis spectra (**Figure 29a**), the AgBr did not presented any specific absorption peak at visible light region. Instead, the shoulder peaks at around 315 nm were observed, consistent with the previously reported observations for silver bromide nanoparticles. The absorbance merely increased at whole visible light region as the AgBr size increased (from ~72 to ~183 nm) because of the bigger particles more scattered the incident light than the smaller ones. As shown in **Figure 29b**, the synthesized Ag@AgBr nanocomposites have distinct absorption peaks in the visible light region compared with the pristine AgBr nanocubes, resulting from the SPR of the formed silver nanoparticles [136,137]. Each sample shows the strong absorption peak at around ~400 nm, which corresponded to the typical plasmon peak of silver nanoparticles. The plasmon peak becomes broader as increasing the size of AgBr substrate because the bigger AgBr has the silver nanoparticles with more diverse shapes and diameters on its surface. Notably, the Ag@AgBr nanocomposites exhibit the absorption peak at red-shifted region, which may be originated from the interaction between the AgBr substrate and the deposited metallic Ag nanoparticles. The

Ag@AgBr T25 sample shows their unique peak at ~600 nm while, the Ag@AgBr T40 sample has the peak at ~650 nm. Literature reported that the refractive index of the substrate caused a shifting of the light absorption. For the Ag nanoparticles on the AgBr surface, the red-shifted absorption peak is observed because the refractive index of the AgBr (2.23) is higher than that of water (1.32) or air (1.0). In the case of the Ag@AgBr T60, specific red-shifted peak was not observed. Instead, the absorption at whole light region was increased compared to the bare AgBr counterpart. It may have originated from a large number of different shapes and size of the Ag nanoparticles grown on AgBr which cause the plasmonic oscillations cover a wide range of the frequencies. Therefore, it can be considered that the light absorption region of the silver-silver bromide nanocomposites can be controlled by varying the size of the silver halide substrate.

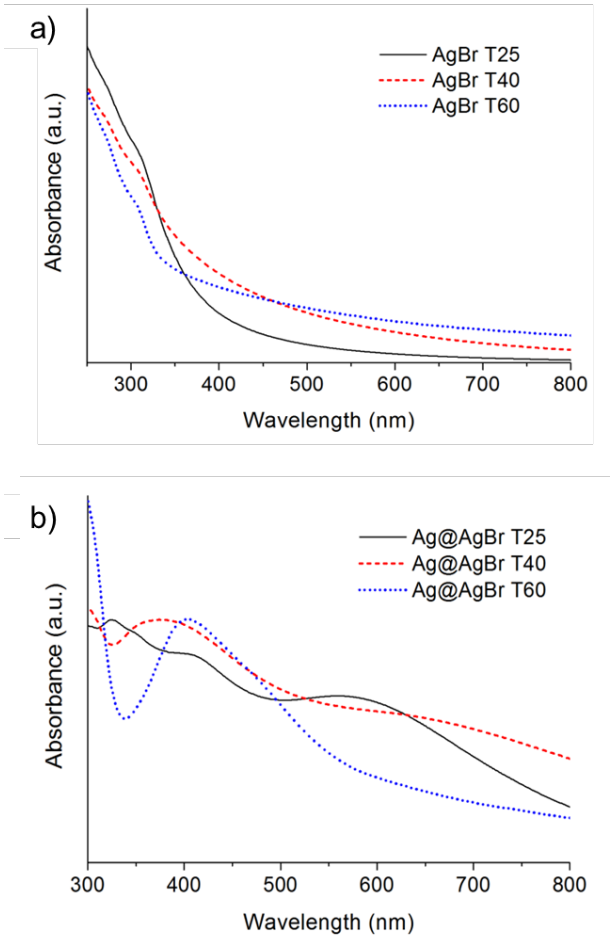

Figure 29. UV-vis spectra of the (a) as-prepared AgBr solution and the (b) Ag@AgBr solution.

3.2.4 Visible-light responsive photocatalytic properties of synthesized Ag@AgBr nanoparticles

The photocatalytic activities of the as-prepared Ag@AgBr nanoparticles were evaluated by decomposition of MB under visible light condition. Generally, the 50 mg of sample was applied to degrade the dye molecules as a standard condition [113]. In this work, the 50 mg of the prepared nanophotocatalysts completely absorbed the MB molecules during the pre-adsorption step because of their high surface area. Thus, the 10 mg of samples was used for photocatalytic activity test. **Figure 30a** shows the photocatalytic degradation of MB over the silver-silver bromides and bare AgBr under visible light ($\lambda > 400$ nm) condition, in which C_0 is the concentration of MB at adsorption-desorption equilibrium and C is the concentration at a given time. In the experimental condition of this work, the bulk AgBr decomposed only 10 % of MB within 30 min. On the other hand, bare AgBr T25 sample showed some photocatalytic activity due to its enlarged surface area; it could degrade 27.8 % of MB within 30 min. The AgBr semiconductor has a bandgap of 2.6 eV, which could be excited under visible light irradiation [43]. Interestingly, the loading of Ag NPs on the AgBr surface remarkably enhanced the dye degradation efficiency of the samples. The

Ag@AgBr T25 sample decomposed the 95 % of MB molecules within 30 min. *Jiang et al.* demonstrated that the interfacial interaction between the metallic Ag and the AgBr is indispensable for the photocatalytic activity of the Ag@AgBr composite [136]. Under visible light irradiation, electric fields are intensive in the vicinity of the Ag nanoparticles because of their SPR, and would induce rapid formation of electron-hole pairs on the AgBr surface. In addition, the AgBr-based conventional semiconductor photocatalysis process simultaneously occurred because AgBr could also be directly photo-excited under visible light irradiation to generate electron-hole pairs in its conduction band and valence band, respectively [136]. Together with the injected SPR electrons from the Ag nanoparticles, the photogenerated electrons in the conduction band could initiate the catalytic reaction [87]. The photocatalytic activity of the Ag@AgBr nanocomposites was in the following order: T25 > T40 > T60. The photocatalytic activities enhanced with decreasing the size of the Ag@AgBr nanocomposites. The smaller photocatalyst provided more sites for contacting and degrading the dye molecules, leading to the enhanced photocatalytic activity. For practical application, the MB degradation test of the Ag@AgBr nanocomposites was performed under direct sunlight condition (air temperature of ~ 30 °C). When the MB

solution containing the synthesized Ag@AgBr T25 samples in placed under the direct sunlight, the blue solution became purplish, the color of silver-silver bromide nanocomposites. **Figure 30b** plot the UV-vis absorption spectra of the test solution at different reaction times under sunlight irradiation condition. The decomposition of MB molecules was completed within 20 min by Ag@AgBr T25 photocatalyst, which is much shorter time compared with the result under Xenon-lamp (100 W) condition. The enhanced activity might be originated from the broadband of the sunlight, including UV. Based on these data it can be concluded that the synthesized Ag@AgBr nanocomposites can be utilized as the visible light driven photocatalyst.

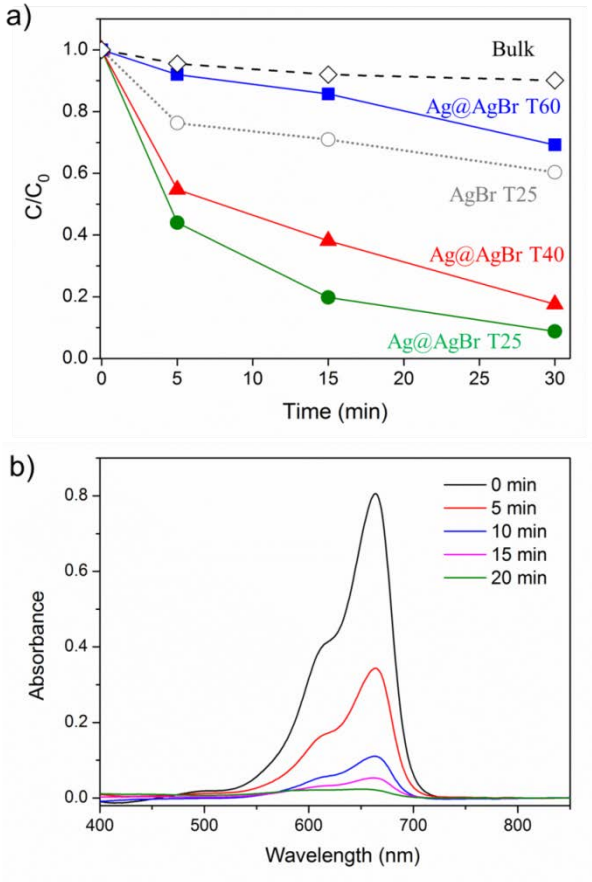

Figure 30. (a) Photocatalytic degradation of MB over various Ag@AgBr composites and pristine AgBr under visible light irradiation (> 400 nm) and (b) Absorption spectra of MB molecules after exposed to the sunlight for different times with the Ag@AgBr T25.

3.3. Fabrication of silver/poly(vinyl alcohol) composite nanofiber in aqueous system

As mentioned above, most of the metal-containing polymer nanofibers have been prepared *via* the electrospinning method, which needs a high electric potential to jet the fibers. Recently, the aqueous synthetic route to fabricate silver nanoparticles/PVA/methacrylated polymer composite nanofibers has been suggested [70,114]. In this work, it is assumed that the Ag/PVA complex was linearly assembled due to the dipole-dipole interaction between the silver nanoparticles under vigorous magnetic stirring condition. However, the formation mechanism of the silver-polymer fibrous nanostructure was not fully understood. Herein, the detail formation mechanism of the Ag nanoparticles embedded PVA nanofibers was newly suggested through careful systematical investigation. This work demonstrates that the introduction of a small molecule such as AIBN can provide a means as powerful as surfactants in controlling the structure of the Ag-PVA nanocomposites. The role of azo compounds has been investigated and a plausible mechanism is proposed to account for the formation of Ag-PVA composite nanofibers. These studies might advance our understanding of the formation of the metal-polymer nanocomposite.

3.3.1 Characterization of silver nanoparticles-containing poly(vinyl alcohol) nanofibers

3.3.1.1. Microscopic observation of the nanofibers

In this work, silver nanoparticles embedded PVA nanofibers were synthesized in aqueous solution at 60 °C. The sample was prepared by adding 1 mL of AIBN (0.1 g) dissolved in MC (methylene chloride) solution to $AgNO_3$ (20 mg)-dissolved PVA (0.1 g) aqueous solution (50 mL) at 60°C. After 6 h of reaction, the solution appeared turbid. Mat-type samples were obtained after centrifugation and drying (**Figure 31a**). Field-emission scanning electron microscopy (FE-SEM) images of the synthesized composites show nanofibrous structures (*ca*. 35 nm), several tens of micrometers in diameter and length (**Figure**s **31b, c**). Additionally, transmission electron microscopy (TEM) observation confirmed that the Ag compounds (diameter: *ca*. 8 nm) were densely embedded throughout the nanofibers (**Figures 31d, e**). Due to the low electron density of the thin PVA shell, it was difficult to identify the polymeric shell on the aligned Ag nanoparticles in the TEM images. Notably, in the FE-SEM images, the synthesized Ag/PVA nanofibers exhibited a smooth surface, with no metallic nodules; this indicates that the Ag nanocompounds were located inside the polymer substrates and

not on the surface of the polymer [138]. Judging from these data, it could be concluded that silver/PVA composite nanofibers were successfully fabricated by the aqueous-phase synthetic method.

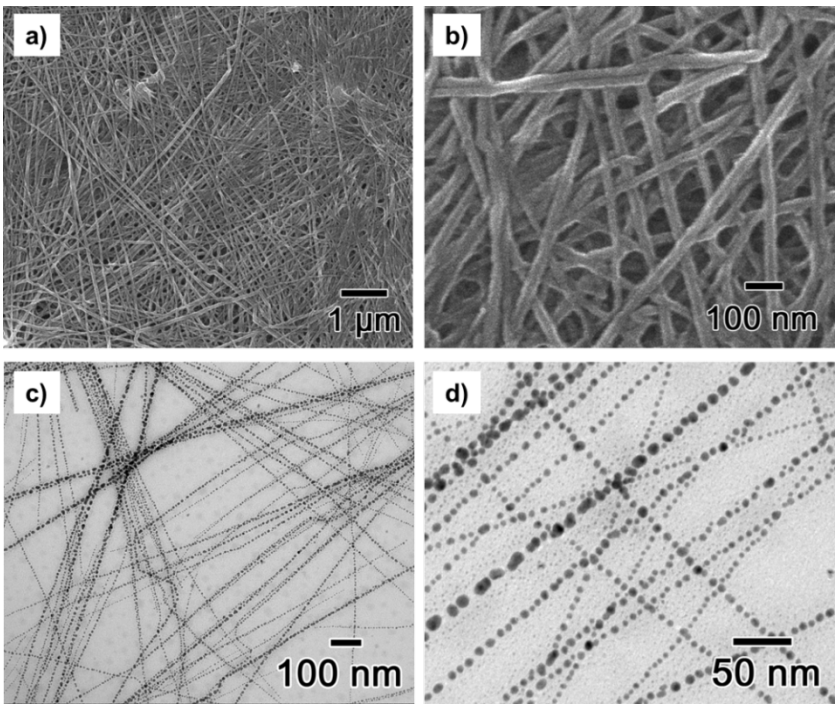

Figure 31. (a,b) FE-SEM and (c,d) TEM images of synthesized Ag/PVA nanofibers.

3.3.1.2. Spectroscopic analysis of the nanofibers

The structural features of the Ag/PVA composite nanofibers were analyzed by Fourier transform infrared (FTIR) spectroscopy. For comparison, the FTIR spectra of pristine AIBN and PVA samples were also obtained. **Figure 32** shows that the Ag/PVA nanofibers had the characteristic peaks of both AIBN and PVA. A broad peak around 3400 cm^{-1} for the Ag/PVA nanofibers was attributed to the O−H stretching vibration of PVA [69]. The peak near 2200 cm^{-1} originated from C≡N bonding in AIBN, which was used as a seed for the Ag complex. Importantly, the vibrational band for C≡N stretching, generally detected at 2245 cm^{-1} for AIBN, had shifted down to 2167 cm^{-1} for the Ag/PVA nanofibers; this was attributed to the restricted vibrational motion of the C≡N group as a result of its coordination with the Ag ions [139]. Additionally, the peak at 1245 cm^{-1}, originating from the C−O stretching vibration of PVA, had shifted to 1220 cm^{-1}. To confirm that the shift was due to Ag coordination and not the formation of hydrogen bonds with absorbed water, it was also observed that the FTIR spectra of the PVA sample dissolved in water (the sample was dried under ambient conditions). In this case, the band shift was not detected. This suggests that the Ag cations interacted with the hydroxyl group of PVA and

reduced the frequency of this absorption band. The FTIR data provided evidence that supported the presence of coordination between the Ag ions and metal-binding groups of AIBN (the cyano group) and PVA (the hydroxyl group). For further study of the Ag/PVA nanofiber composition, X-ray photoelectron spectroscopy (XPS) analysis was performed. XPS is effective in characterizing the elemental composition of the Ag/PVA-composite nanofiber surface. **Figure 33a** shows XPS peaks for C 1s, N 1s, O 1s, and Ag 3d, indicating the existence of PVA and AIBN molecules on the surface of Ag nanoparticles. The C 1s spectrum can be deconvoluted into four peaks located at 284.5, 285.9, 287.4, and 288.6 eV, which were assigned to the characteristic peaks of the C−C (and/or C−H), C≡N, C−OH, and C=O groups, respectively (**Figure 33b**). The C−OH peak may be attributed to the hydroxy group of PVA [140,141]. Previous studies have reported that PVA contains small amounts of carbonyl groups in its polymer chain, resulting from commercial preparation of PVA by hydrolysis of poly(vinyl acetate). Thus, the C=O groups most likely originated from hydrolyzed PVA [142]. **Figure 33c** presents the Ag 3d XPS spectrum of the as-prepared samples. The Ag/PVA nanofiber shows two peaks centered at 373.9 and 368 eV. The Ag 3d peaks indicate that two components coexist in Ag $3d_{5/2}$ and Ag

$3d_{3/2}$ signals, giving peaks at 367.8 and 368.5 eV for $3d_{5/2}$, while 373.8 and 374.5 eV for $3d_{3/2}$. The peaks at 367.8 and 373.8 eV can be ascribed to Ag^{+} ions, whereas the peaks at 368.5 and 374.5 eV can be attributed to metallic Ag^{0} [143]. The XPS results support that the product contained Ag compounds, and also that Ag was partially reduced to metallic Ag (*ca.* 36 %). Under the experimental conditions of this study, some of the Ag^{+} ions were reduced to metallic Ag nanoparticles by hydroxyl groups of PVA at elevated temperatures. Sixty-four percent of the Ag compound remained in an Ag-complex form with AIBN and PVA. Additionally, thermogravimetric analysis (TGA) data confirmed that the synthesized Ag/PVA nanofibers contained *ca.* 55 wt% Ag compound (**Figure 34**). Unfortunately, the spatial distribution of metallic Ag and Ag complexes (Ag ions) cannot be clearly imaged with electron microscopic techniques, because exposing the Ag complex to an electron beam with high current density reduces the Ag complex to metallic Ag.

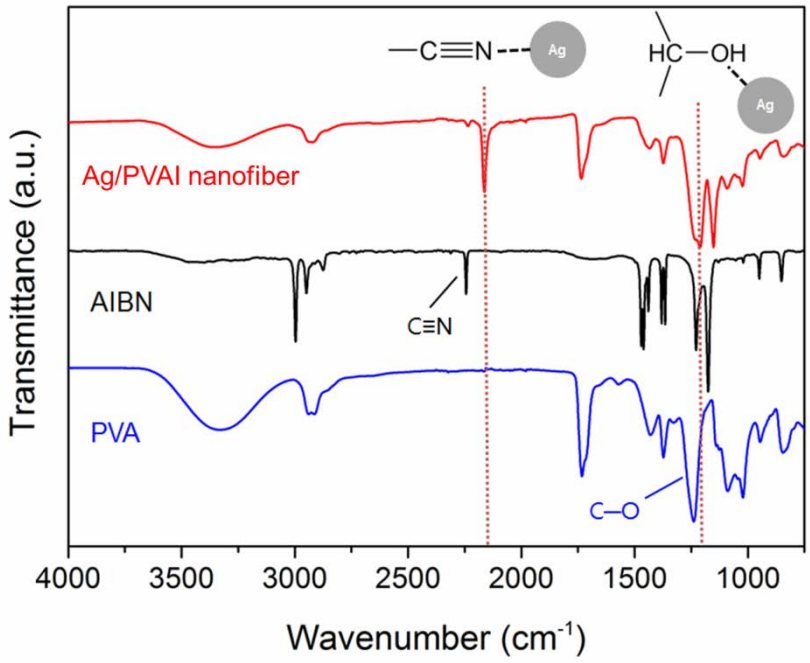

Figure 32. FTIR spectra of the Ag/PVA composite nanofibers (upper, red line), bare AIBN (middle, black line), and bare PVA (bottom, blue line). Vertical dot lines represent the shifted C≡N peak (left) and C-O peak (right) of the Ag/PVA composite nanofibers.

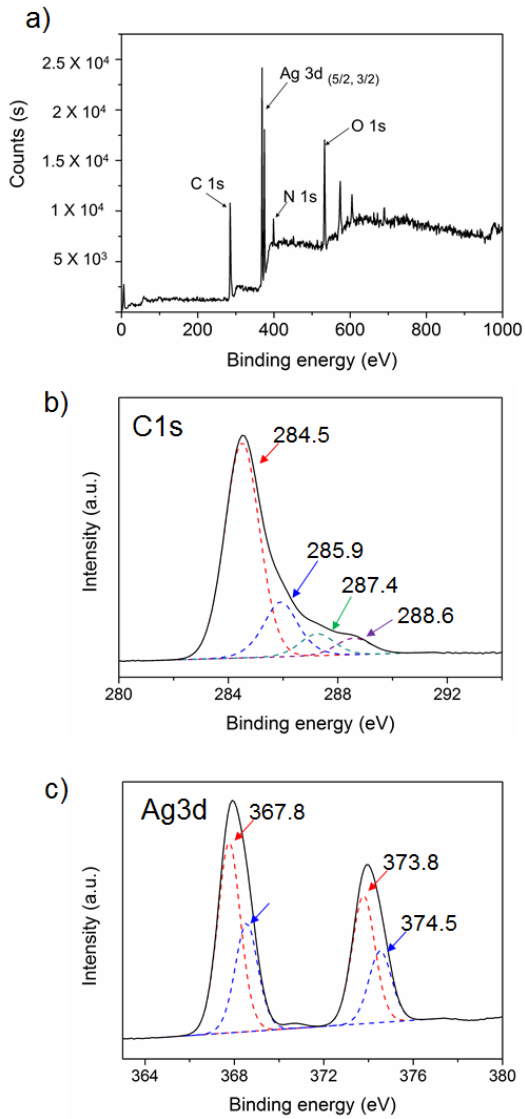

Figure 33. (a) XPS survey spectra of the Ag/PVA nanofibers showing the peaks for C 1s, Ag 3d, N 1s, and O 1s. Normalized XPS spectra of the (b) C 1s and (b) Ag 3d regions.

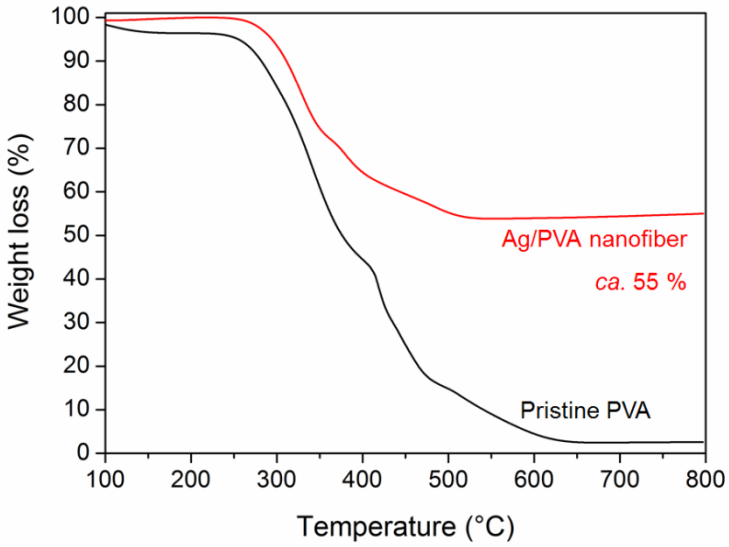

Figure 34 TGA graph of the silver-PVA composite nanofibers. Pristine PVA molecule was used as comparative material.

3.3.2 Systematic investigation of the fabrication of silver/poly(vinyl alcohol) nanofibers.

3.3.2.1. Control experiments

In this synthesis, AIBN is critical to the formation of Ag/PVA nanofibers. When the reaction was conducted with only Ag nitrate and PVA (without AIBN), with other experimental parameters being kept the same as in **Figure 31**, there was no fiber formation; only micrometer-sized irregular products were observed (**Figure 35**). Meanwhile, a comparative reaction containing only Ag nitrate and AIBN (without PVA) was performed, which produced needle-shaped products having various diameters (ranging from 0.2–1 μm) (**Figure 36**). AIBN formed a complex with Ag ions *via* coordination between the Ag^+ ions and the cyano group of the AIBN molecules. The Ag ion/AIBN complexes then became oriented in the flow direction due to the shear flow produced by magnetic stirring [70]. The length of the complex was short due to the absence of PVA, which acted as a gelator for nanofiber growth in the axial direction. Additionally, when the reaction was performed without stirring, aggregated particles were obtained instead of the nanofibers (**Figure 37**). These results indicate that the generation of the Ag/AIBN complex is a prerequisite for nanofiber formation and that magnetic

stirring played a pivotal role in the formation of Ag/PVA nanofibers.

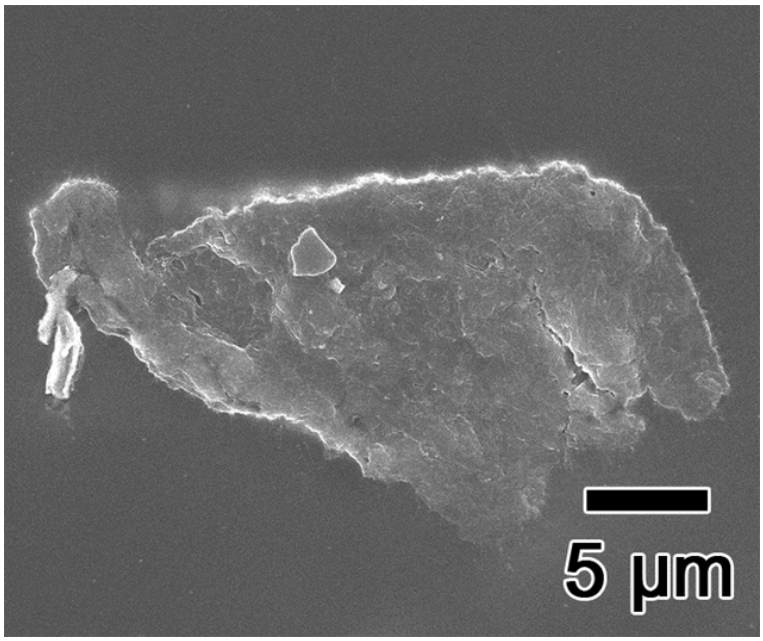

Figure 35. FE-SEM image of the product which is obtained from the control experiment without AIBN.

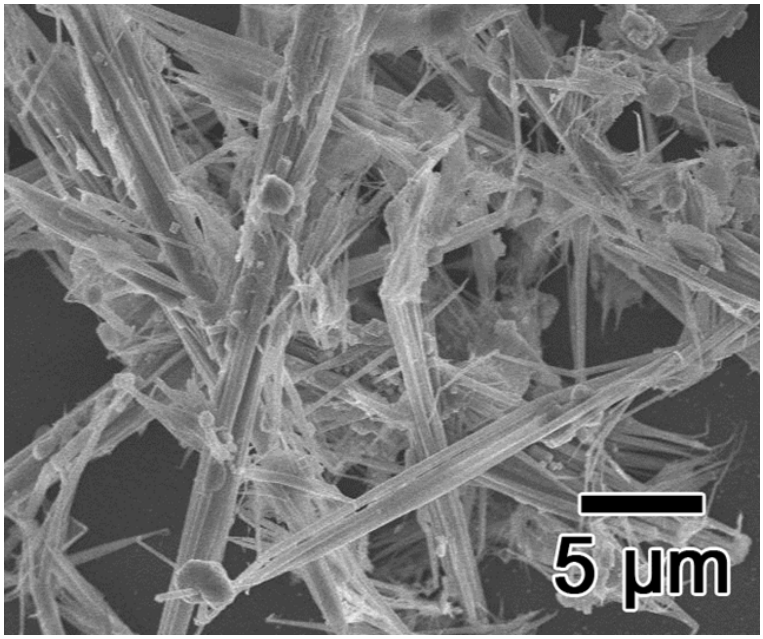

Figure 36. FE-SEM image of the silver-AIBN nanorods which is obtained from the control experiment without PVA.

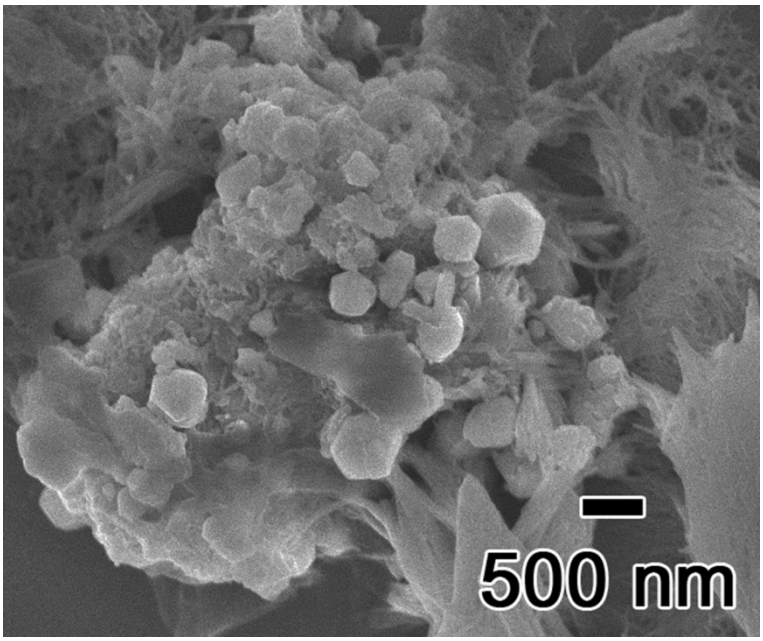

Figure 37. FE-SEM image of the silver-PVA composite which is obtained from the control experiment without magnetic stirring.

3.3.2.2. Time-dependent observation of growth of the nanofibers

Figure 38 shows time-dependent microscopic observation of the evolution of the nanofiber shape as a function of the reaction time. Aliquots of the reaction solution were removed at various reaction times (0.5, 1, 2, and 4 h) and examined under FE-SEM and TEM. In the initial stage (t = 30 min), micron-sized complexes were observed (**Figure 38a, c**); these complexes were believed to have been composed of Ag ions, AIBN, and PVA. After 1 h of reaction (**Figure 38b**), the products became smaller (sub-micrometer in diameter) and nanofibrous structures having a short length were occasionally observed. The nanofiber appeared to be growing from the surface of the spherical particles. As the reaction time increased, there was a significant change in the morphology of the products. At t = 2 h (**Figure**s **38d–f**), the fibrous nanostructures with diameters of *ca.* 35 nm were prominent in the product, implying that the nanofibers were grown from complex particles; this was confirmed by magnified FE-SEM images (**Figure 38e**). Over the next 2 h, the nanofibers continued to grow in the axial direction. The diameter of the nanofibers barely changed, while the seed particles became smaller nanoparticles; this suggests that the particles were precursors for the growth of the nanofibers (**Figures 38g, h**). TEM analysis confirmed that

the complex particles, obtained at t = 0.5 h, had Ag compounds in their stuctures. The spatial distribution of Ag and the polymer could not be clearly imaged with TEM due to the change in morphology of the Ag complex, which occurred when the complex was reduced to metallic Ag by the electron beam [44]. As the reaction time increased, fibrous nanostructures were grown from the complex particles (**Figure**s **38f, i**); the grown nanofibers consisted of finely-assembled Ag nanoparticles. Based on these data, the Ag-containing polymer nanofibers were grown from Ag/AIBN/PVA complex particles that formed early in the reaction process.

Based on the microscopic observation, the plausible forming mechanism of the nanofibers can be suggested as shown in **Figure 39**. The Ag/AIBN/PVA complex particles were formed at the initial step because of the coordination between the cationic silver ions and cyano groups of AIBN and hydroxyl groups of PVA. Then, as the reaction was proceeded at 60 °C under magnetic stirring condition, the nanofibers were gradually grown from the complex particles. While the formed nanofibers were getting longer, the size of complex particles which were generated at the early stage of reaction was decreased. After 6 h of reaction, the silver nanoparticles containing polymeric nanofibers could

be obtained as main product as shown in **Figure 31**.

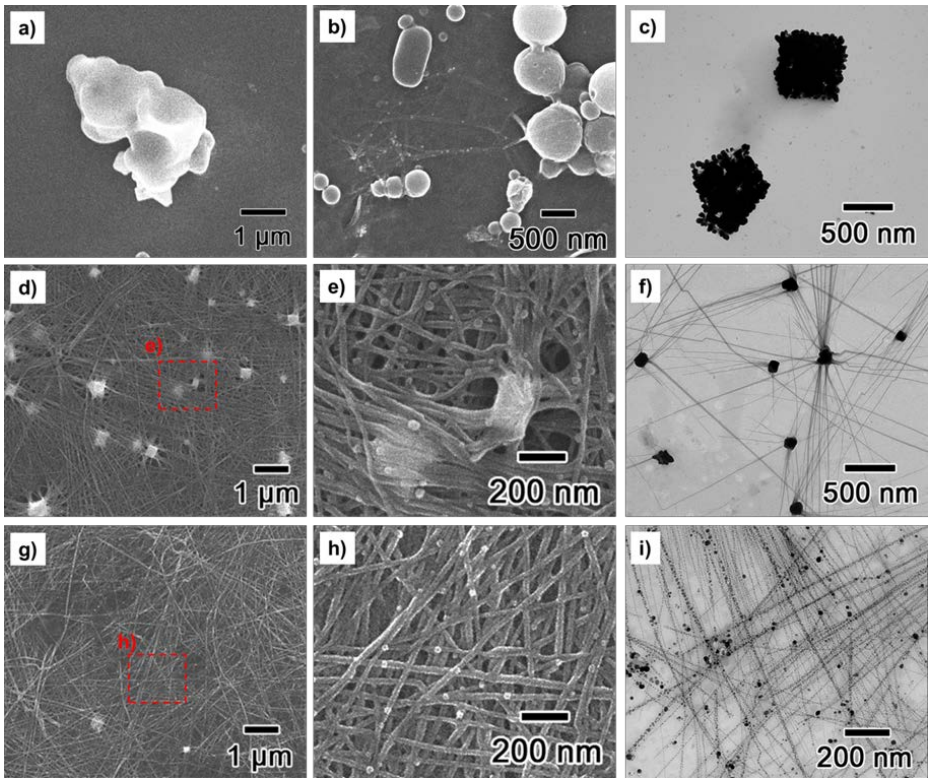

Figure 38. FE-SEM (left, middle column) and TEM (right column) images of the Ag/PVA nanocomposites prepared at different reaction times: (a,c) 0.5, (b) 1, (d,e,f) 2, and (g,h,i) 4 h. The reactions were conducted in aqueous solution at 60°C with magnetic stirring.

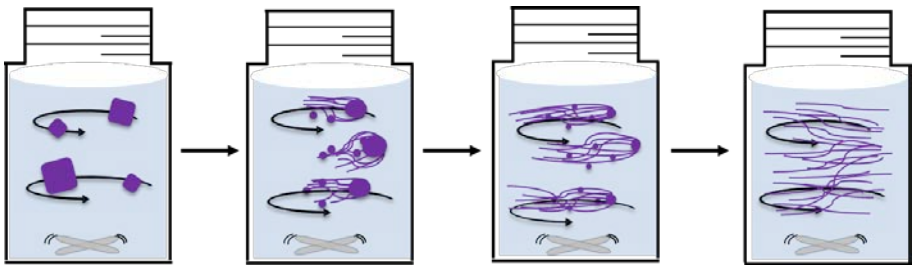

Figure 39. Schematic illustration of the fabrication of silver/PVA nanofibers through the complex-mediated growing process.

3.3.3 Study on synthetic mechanism of the complex-mediated growth of silver/poly(vinyl alcohol) nanofibers

From the aforementioned results, it is clear that the decomposition of AIBN played an important role in the formation of Ag/PVA nanofibers. Notably, when the reaction was performed at 25°C, the nanofibers did not exist. To confirm that the decomposition of AIBN induced the nanofibrous structure formation, several control experiments were conducted. When AIBN was replaced with malononitrile, which has only di-nitrile groups (without azo-groups), the resulting product had a nanoparticle shape. In contrast, when AIBN was replaces with other azo-compounds (capable of decomposition at 60°C), the nanofibers were obtained as shown in **Figure 40**. To investigate the effect of the radicals, AIBN was replaced with benzoyl peroxide (BPO), while carefully keeping the other reaction parameters the same. Similar to AIBN, BPO also decomposed and formed radicals at elevated temperatures. However, irregular-shaped polymeric lumps were obtained after the reaction; this may be due to the different functional groups between AIBN and BPO that have different metal-binding energies. Therefore, it can be concluded that the breaking phenomena of the AIBN molecule and its cyano-functional group (metal-binding group) played a key role in the

formation of the Ag/PVA composite nanofibers.

The plausible synthetic mechanism was suggested from the view of molecules and functional groups (**Figure 41**). In the early stages of the reaction, Ag/AIBN/PVA complex structures were formed by the interaction between cationic Ag ions and the metal-binding functional groups of PVA (hydroxyl group) and AIBN (cyano group). As the temperature approached 60°C under magnetic stirring conditions, AIBN decomposed *via* breakage of the C–N bond (not the C≡N bond). Consequently, the Ag components assembled by the di-cyano groups of AIBN were also disassembled. PVA bound to the detached Ag components inhibited their disassembly, and the Ag components became aligned in the shear direction of the flow produced by magnetic stirring. This flow direction also corresponded to the orientation of the PVA. As a result, the nanofibers grew from the complex particles. The decomposition of AIBN occurred gradually over the course of the reaction, which promoted the formation of Ag/PVA composite nanofibers (the nanofibers contained decomposed AIBN). The Ag complex (or metallic Ag) nanoparticles provided a solid substrate for the formation of nanofibers. **Table 5** summarizes the average diameter and length of the Ag/PVA nanofibers obtained under various experimental

conditions, as well as the molecular weight of PVA and the molar ratio of PVA to $AgNO_3$. The diameter and length were measured from each FE-SEM image. Overall, the amount of PVA affected the diameter of the nanofibers; the diameter of the composite nanofibers decreased as the ratio of PVA to Ag precursor increased. Additionally, the diameter of the nanofibers decreased as the molecular weight increased. As mentioned above, the nanofibers grew from the Ag/AIBN/PVA complex that formed earlier, through decomposition of the AIBN molecules. When the amount of PVA was reduced, thicker and shorter polymer nanofibers were obtained because the PVA could not sufficiently bind or stabilize the Ag nanoparticles, which had become detached from the Ag/AIBN complex formation. Based on these data, PVA acted as a stabilizer and a gelator in the Ag/PVA nanofiber formation mechanism.

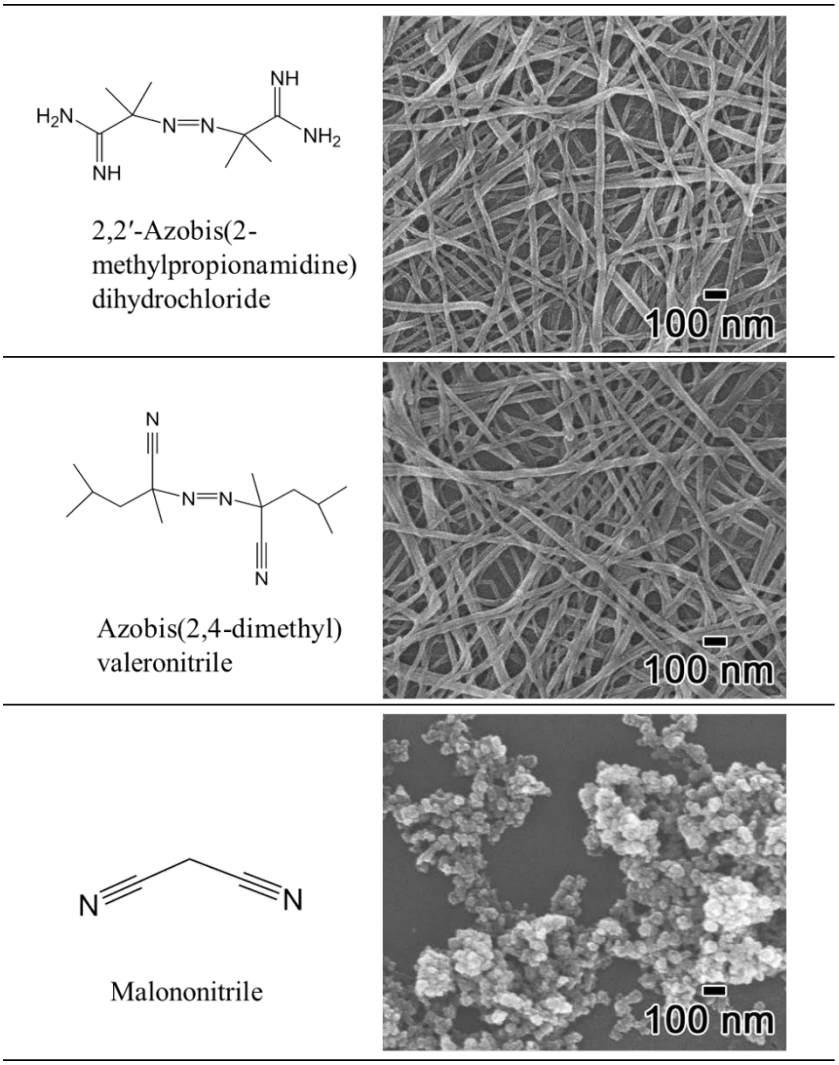

Figure 40. FE-SEM images (right column) of the silver complexes prepared under the same conditions as those in **Figure** 31 except that the AIBN was replaced with other compounds as shown in the left column.

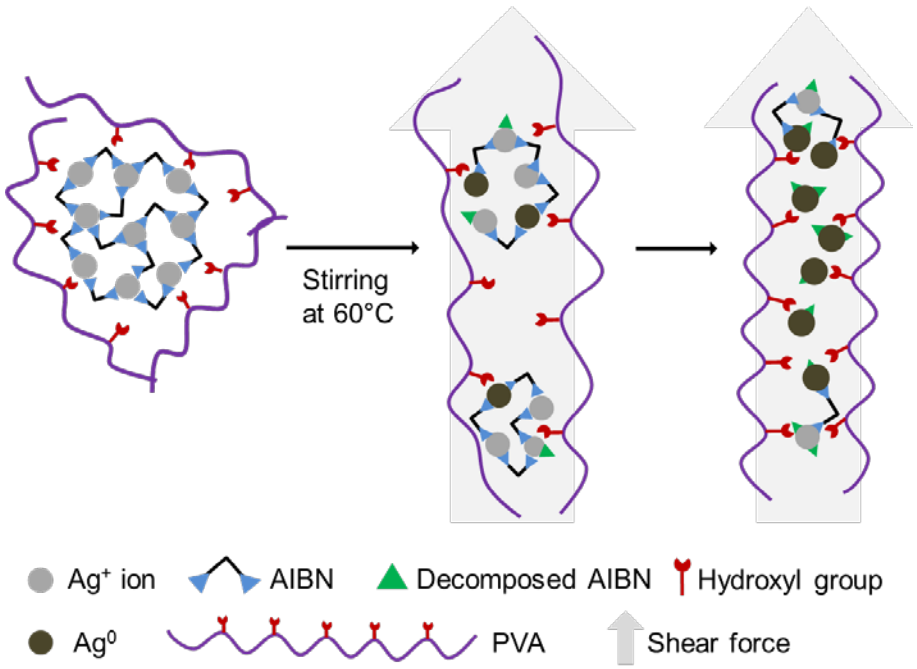

Figure 41. Illustration of the plausible formation mechanism of silver/PVA nanofibers.

Table 5. Summary of the diameter and length to diameter ratio of the synthesized silver/PVA composite nanofibers depending on the concentration and molecular weight of PVA.

Mw of PVA	Concentration [μg/mL]	Molar ratio, PVAI:silver nitrate	Diameter [nm]	Length to diameter ratio[a]
146,000-186,000	260	5:1	~37.3	>100
146,000-186,000	52	1:1	~50	>100
146,000-186,000	26	0.5:1	~75	>100
146,000-186,000	5.2	0.1:1	~110	>100
146,000-186,000	1	0.02:1	~200	~45
31,000-50,000	52	1:1	~60	>100
9,000-10,000	52	1:1	~80	>100
9,000-10,000	0.5	0.01:1	~500	~30

[a] Compared with the diameter, the materials show a range of variation in their length, and thus we expressed '>100' when the average length value exceeds 10 μm.

3.4. Fabrication of silver/poly(vinyl alcohol)/poly[2-(tert-butylaminoethyl) methacrylate] nanofibers through aqueous system as antibacterial agents

3.4.1 Fabrication and characterization of silver/poly(vinyl alcohol)/poly[2-(tert-butylaminoethyl) methacrylate] nanofibers

3.4.1.1 Synthetic procedure of the nanofibers using a radical mediated dispersion polymerization

The synthesis of Ag/PVA/PTBAM nanofibers by radical-mediated dispersion polymerization is illustrated in **Figure** 42. Silver ions (Ag+) were added to an aqueous solution of PVA and were coordinated to hydroxyl groups on the PVA. The Ag^{+}−PVA complex was linearly assembled due to high shear under vigorous stirring. AIBN was then added to the Ag^{+}−PVA aqueous solution at 60 °C. AIBN acted as a reducing agent for the silver ions and as a radical initiator for the TBAM monomer. The silver nanoparticle−PVA complexes (Ag−PVA) were linearly and tightly assembled due to both the high shear conditions and dipole−dipole interactions between silver nanoparticles [144]. When TBAM monomer was injected into the reaction medium, the carboxyl groups of the TBAM monomer formed hydrogen bonds with the hydroxyl groups of PVA. PVA acted as a gelator to form and grow nanofibers in the axial direction and also acted stabilizer to disperse silver nanoparticles. The TBAM monomer was polymerized onto the

Ag−PVA complex for 24 h via radical polymerization using AIBN as an initiator, after which Ag/PVA/PTBAM nanofibers were obtained.

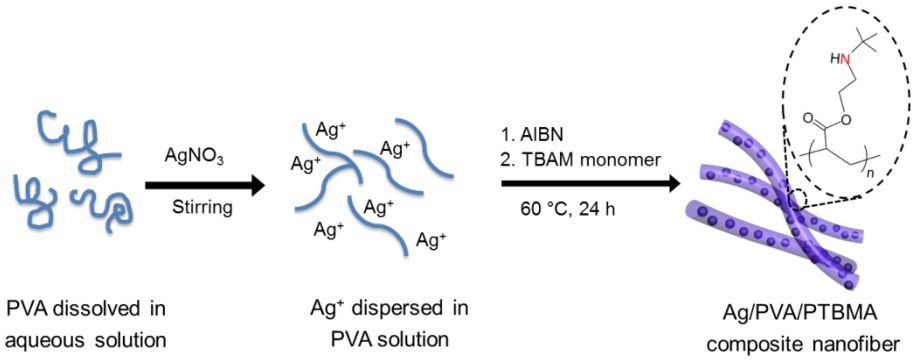

Figure 42. Illustration of the synthetic procedure of silver/PVA/PTBAM nanofibers.

3.4.1.2 Characterization of the synthesized silver/cationic polymer nanofibers

3.4.1.2.1. Microscopic observation of the nanofibers

FE-SEM images in **Figure 43** show the morphology of the fabricated Ag/PVA/PTBAM composite nanofibers. As shown in the FE-SEM image, the synthesized composite nanofibers had fibrous morphology; the average diameter and length of the polymer nanofibers were approximately 40 nm and greater than 10 μm, respectively. It was confirmed using TEM that silver nanoparticles of average 8.5 nm in diameter were finely embedded throughout the polymer nanofibers (**Figure 44**). Additionally, the synthesized Ag/PVA/PTBAM nanofibers possessed a smooth surface morphology (**Figure 43b**), which indicates that the silver nanoparticles were not located on the surface but were instead embedded inside the PTBAM polymer nanofiber. Importantly, it was verified that a nanofibrous structure could be obtained using radical-mediated dispersion polymerization. When the experiments proceeded without $AgNO_3$, the products had atypical morphology with micrometer size rather than fibrous nanostructure (**Figure 45**). The PTBAM was polymerized by the dispersion polymerization using AIBN as radical initiator. However, the polymer did not construct the fibrous

nanostructure. Based on these data, it can be considered that the silver nanoparticles play an important role in formation of fibrous nanostructure.

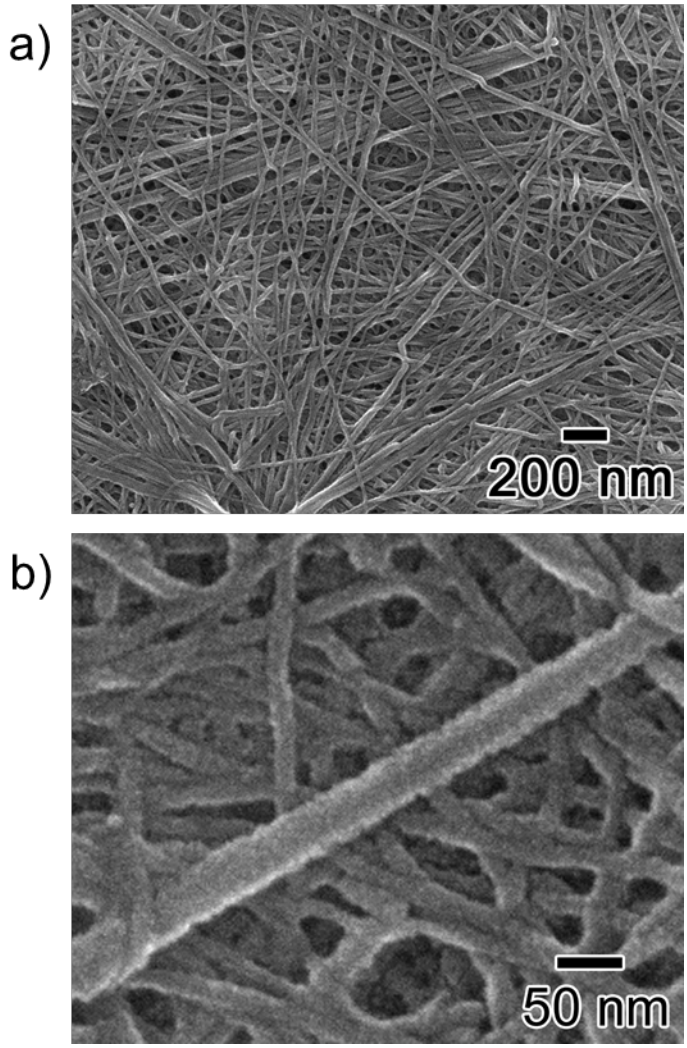

Figure 43. (a) Low- and (b) high-magnified FE-SEM images of synthesized Ag/PVA/PTBAM nanofibers.

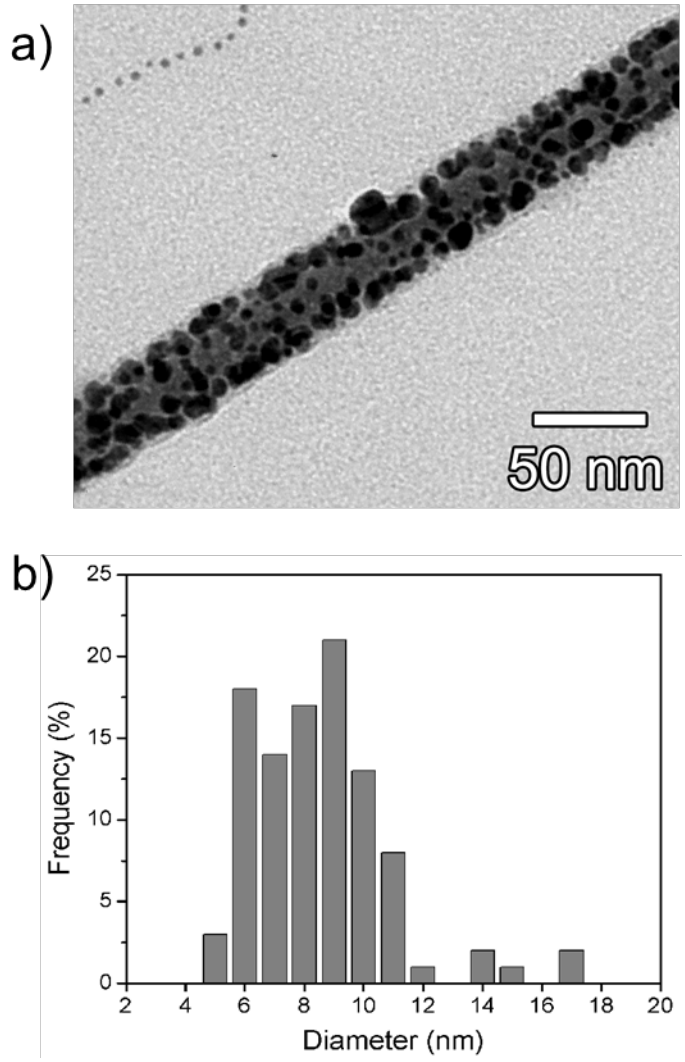

Figure 44. (a) TEM images of the silver nanoparticles embedded PTBAM nanofiber and (b) size distribution of the embedded silver nanoparticles. The silver nanoparticle size was determined via randomly counting 100 Ag nanoparticles.

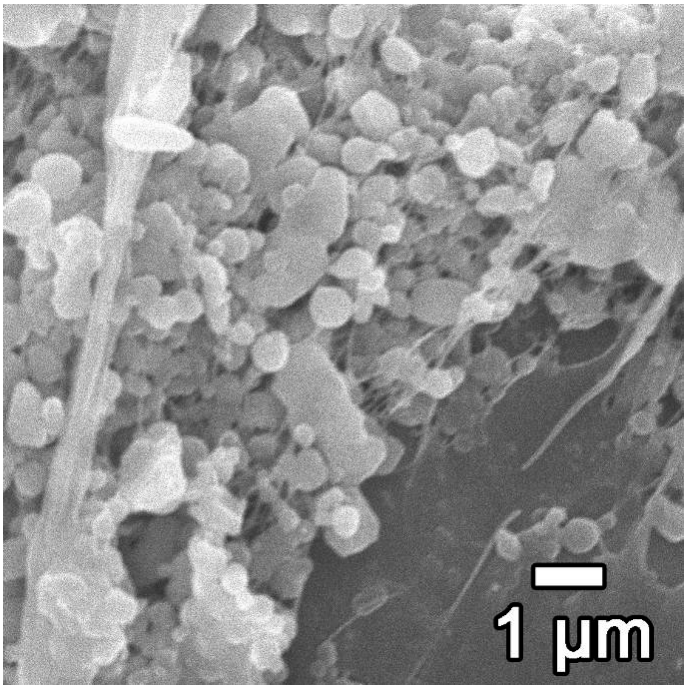

Figure 45. FE-SEM image of PTBAM synthesized as same condition as the Ag/PTBAM nanofibers except for the absence of silver nitrate.

3.4.1.2.2. Spectroscopic observation of the nanofibers

The optical properties of the Ag/polymer nanofibers were analyzed by absorption spectroscopy. To verify polymerization of the PTBAM, FTIR analysis was performed (**Figure** 46). A peak near 3400 cm^{-1} was observed in the FTIR spectrum of the Ag/PVA/PTBAM and was attributed to the O−H stretching vibration of PVA. Peaks at 1738 cm^{-1} and in the 1550−1610 cm^{-1} region were attributed to C=O stretching and COO asymmetric vibrations of PTBAM [145]. In addition, peaks at 1230 and 1150 cm^{-1} were attributed to C−N stretching modes. The peak at 2200 cm^{-1} originated from C≡N bonding in AIBN, which was used as a complex precursor and an initiator.

In the UV−vis spectra (**Figure 47**), the plasmon absorption peak at 402 nm was characteristic of nanosized silver particles; the broadness of this peak was indicative of the polydisperse and nanoscale size of these nanoparticles [146,147]. An XPS spectrum of the Ag/PVA/PTBAM composite is presented in **Figure 48**; the two peaks at 369 and 375 eV, with 6.0 eV separation, corresponded to the Ag 3d5/2 and Ag 3d3/2 binding energies, respectively [148]. It can be concluded from the spectral data that the Ag/PVA/PTBAM nanofiber composite had negligible shifts from and the same spin energy separation as metallic

silver, implying that the synthesized silver nanoparticles were mostly zerovalent. Based on these data, the polymerization was successfully carried out on the surface of the silver−PVA complex, which led to the formation of PTBAM nanofibers with embedded silver nanoparticles. In addition, thermogravimetric analysis (TGA) confirmed that the synthesized Ag/PVA/PTBAM nanofibers contained about 55 wt% silver (**Figure 49**). The weight loss of Ag/PVA/PTBAM nanofibers between 100 and 800 °C (about 45 wt%) was attributed to the thermal degradation of the polymer substrate (PVA and PTBAM). Judging from these ata, it was confirmed that the fabricated silver embedded PTBAM nanofibers were composed of *ca.* 55 wt% of silver. Furthermore, compared with the Ag/PVA nanofibers, the Ag/PVA/PTBAM nanofibers more slowly lost ther wight in the region of 400 to 700 °C. The TGA data support indirectly that the PTBAM was polymerized by the dispersion polymerization method.

The stability of the silver nanoparticles in the polymeric substrates was investigated (**Figure 50**). The colloidal silver nanoparticles were synthesized by generally known polyol synthetic route. The synthesized colloidal silver nanoparticles were easily aggregated in laboratory light condition without any stabilizer. However, the silver nanoparticles in the

Ag/PVA/PTBAM nanofibers had a lower tendency toward aggregation compared with colloidal silver nanoparticles [149.150]. It can be considered that the polymer substrate prevented aggregation of the embedded silver nanoparticles.

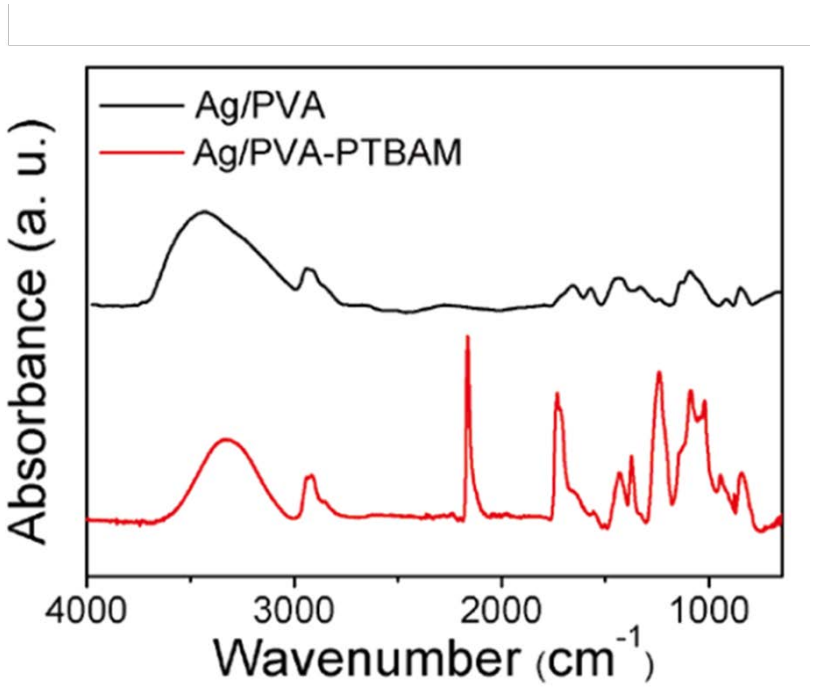

Figure 46. FTIR spectra of Ag-PVA composite and the fabricated silver embedded polymer nanofibers. The Ag-PVA composite was prepared with only $AgNO_3$ and PVA (without AIBN).

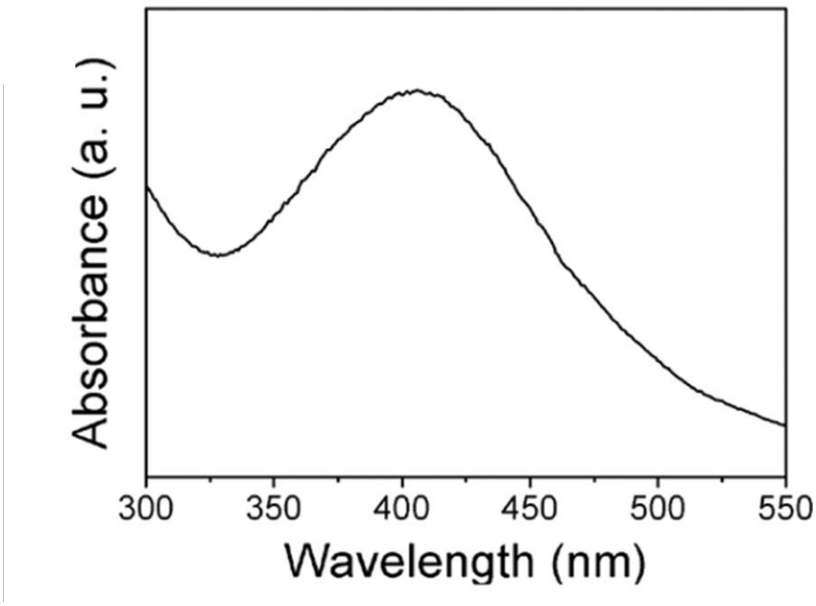

Figure 47. UV-vis spectrum of the Ag nanoparticles embedded PTBAM nanofibers.

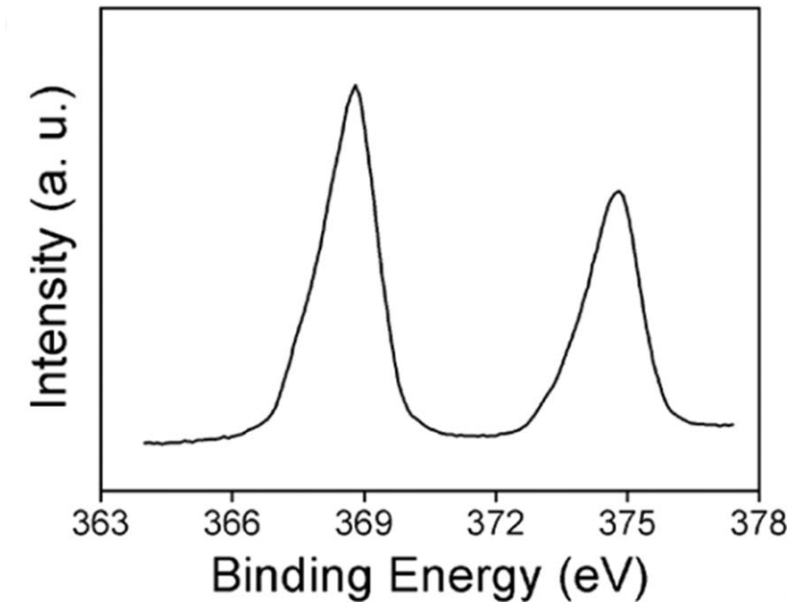

Figure 48. XPS spectrum of Ag nanoparticles embedded PTBAM nanofibers.

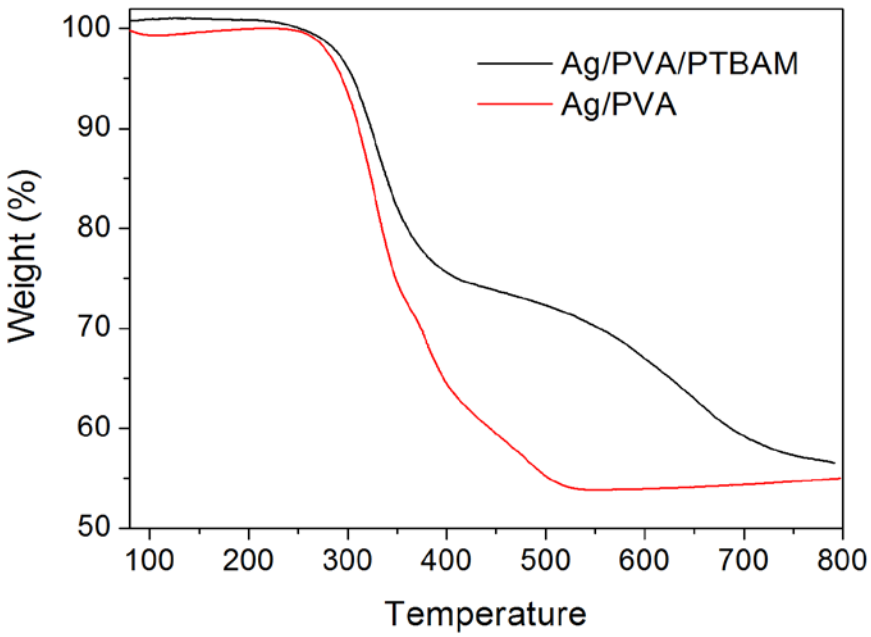

Figure 49. TGA graph of the Ag/PTBAM nanofibers and Ag/PVA nanofibers.

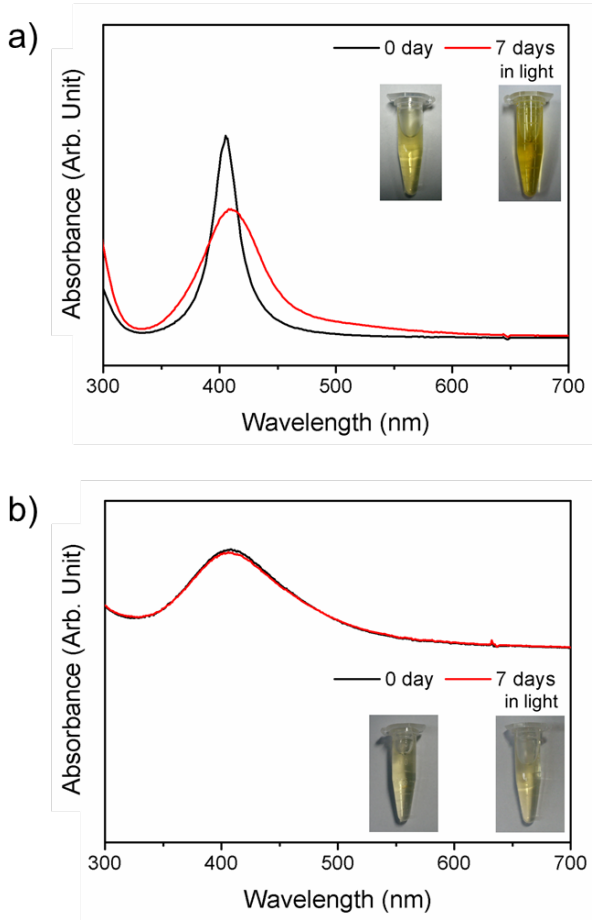

Figure 50. Absorption spectra of (a) colloidal silver nanoparticles and (b) Ag/PVA/PTBAM nanofibers. The spectra was obtained when the sample was newly synthesized (black line) and stored with white light irradiation for 7 days (red line). The inset pictures represent the sample solution under different conditions.

3.4.2 Antibacterial properties of the synthesized silver nanoparticles embedded cationic polymer nanofibers

3.4.2.1 Modified Kirby-Bauer (KB) antimicrobial test

The antibacterial performance of prepared Ag/PVA/PTBAM nanofibers was investigated using a modified Kirby-Bauer technique. SSD, a known anti-inflammatory ingredient, was chosen as a comparative material. Ag/PVA/PTBAM nanofibers and SSD were made into discs with diameters of approximately 13 mm and placed on a bed of *S. aureus* in an agar plate. The antibacterial properties were measured by evaluating the zone of inhibition around the disk after incubation at 37 °C (**Figure 51**). The diameter of the zone of inhibition for the Ag/PVA/PTBAM nanofiber composite disk was approximately 50.2 mm, whereas that of the SSD disk was approximately 17.6 mm. These results indicated that the Ag/PVA/PTBAM nanofibers exhibited superior performance as an antibacterial agent compared to SSD. The SSD slowly releases silver ions as an antibacterial agent,20 and it is possible that the diffusion of silver ions was blocked by the formation of secondary compounds such as silver chloride in the Kirby-Bauer test media [148]. However, in the case of Ag/PVA/PTBAM nanofibers, the PTBAM substrate is sufficiently porous to allow water to pass through the

nanofibers [151]. Thus, silver nanoparticles (or silver ions) embedded in the PTBAM nanofibers could easily diffuse into the test media and act as biocidal agents.

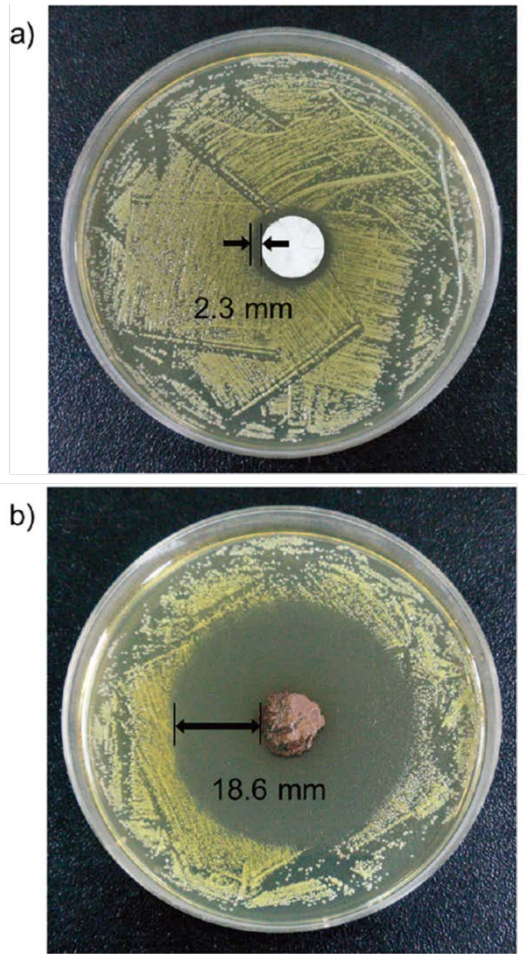

Figure 51. Photograph images of the zone of inhibition of (a) silver sulfadiazine and (b) silver/PTBAM nanofiber by the modified Kirby-Bauer test. Two silver compounds were pressed by hydraulic press to obtain disc shape and placed on the lawn of *S. aureus*. After 12 h of incubation, the zone of inhibition was measured. Both disk sizes are *ca.* 13 mm in diameter.

3.4.2.2 Antibacterial kinetic test

A bacterial inhibition growth curve was used to study the growth kinetics of *E. coli* and *S. aureus* with prepared biocidal samples (**Figure 52**). The optical density at 600 nm (OD_{600}) was measured to monitor bacterial growth; the bacteria were grown to an OD_{600} of 0.1 and then various concentrations of Ag/PVA/PTBAM nanofibers or SSD were added to the bacterial solution [152]. In both cases, the bacterial growth was delayed as the concentration of silver compounds increased, but the rates of bacterial growth delay were different. The growth of *E. coli* was completely inhibited by the Ag/PVA/PTBAM nanofibers when the concentration of nanofibers is 10 μg/mL. The SSD inhibited growth of *E. coli* at 25 μg/mL. In addition, Ag/ PTBAM nanofibers with 5 μg/mL of concentration were able to slow the growth of *S. aureus*, whereas SSD slowed its growth at 10 μg/mL. These results confirmed that the Ag/PVA/PTBAM nanofibers possessed enhanced antimicrobial activity compared to SSD. Both silver ions and silver nanoparticles exhibit antibacterial properties via similar mechanisms, such as interactions with bacterial membranes or binding with metabolic materials [33,34]. However, for the same total silver concentration, the silver nanoparticles in Ag/PVA/PTBAM exhibited significantly higher antibacterial effects

than the silver ions in SSD. When silver ions come into contact with bacteria, precipitates are formed, and the antimicrobial ability of SSD deteriorates [153]. In contrast, the Ag/PVA/PTBAM nanofibers release silver nanoparticles, which come into contact with bacteria without direct precipitation. Therefore, the prepared Ag/PVA/PTBAM nanofibers, which contained silver nanoparticles, showed higher bactericidal efficacy than SSD, which contained only silver ions. The nanometer-sized PTBAM polymer nanofibers also provided a large surface area for more effective antimicrobial performance [154,155].

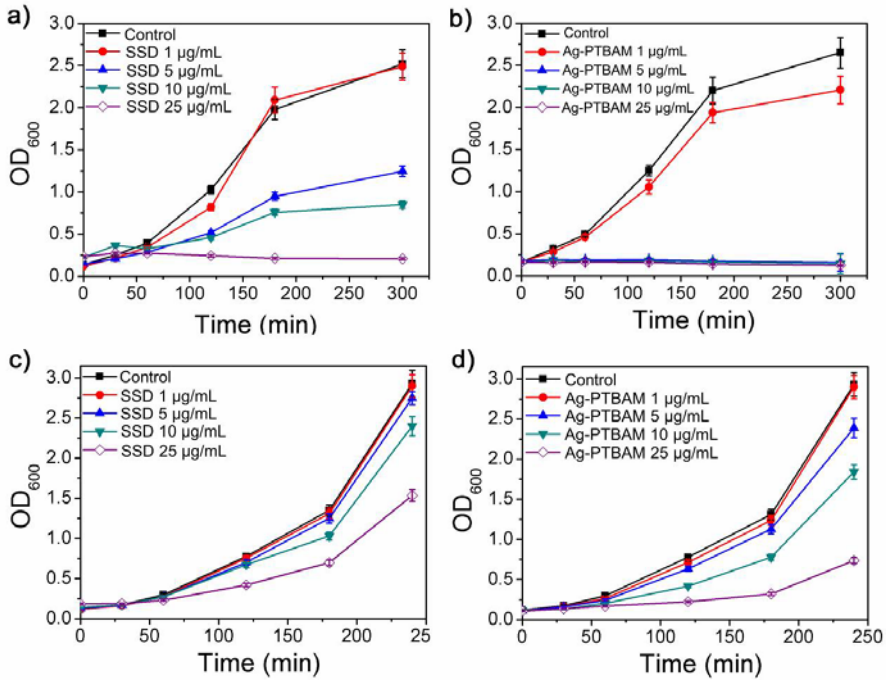

Figure 52. Bacterial growth curve in LB media. Different concentrations of silver sulfadiazine (SSD) or silver nanoparticles embedded cationic polymer nanofiber (Ag/PTBAM) were added to the *E. coli* (a and b) and *S. aureus* (c and d) culture. The growth of the bacteria was monitored measuring the optical density at 600 nm.

3.4.2.3 Minimum inhibitory concentration (MIC) test

Finally, it was evaluated that the extent to which the antibacterial properties of the PTBAM substrate itself contributed to its excellent antibacterial activities. An MIC test was performed to verify the biocidal properties of PTBAM nanofibers. Nanofibers with diameters similar to PMMA (which has no specific biocidal activity) were prepared for comparison with silver nanoparticle-embedded PMMA. The MIC value of $AgNO_3$ was also obtained for comparison. Serial concentrated solutions were each incubated with equal volumes of *E. coli* and *S. aureus* suspensions. The concentrations of the sample solutions were adjusted based on silver content. Growth or no-growth of bacteria was determined by visual inspection. In the case of Gram-negative *E. coli*, the MIC of Ag/PVA/PTBAM nanofibers was about two times lower that of Ag/PMMA nanofibers and about 16 times lower than that of $AgNO_3$ after 24 h incubation (**Table 6**). An additional 24 h after inoculation with fresh bacteria, the MIC values at 48 h were higher than those at 24 h because of the addition of new organisms. An MIC test against Gram-positive *S. aureus* was also performed. In this case, the Ag/PVA/PTBAM nanofibers exhibited enhanced antibacterial activity compared to both Ag/PMMA nanofibers and $AgNO_3$. Notably, the Ag/PVA/PTBAM

nanofibers had higher bactericidal efficiencies than Ag/PMMA nanofibers, which were attributed to the additional antibacterial performance of the PTBAM substrate. The pendant amino groups of PTBAM act as bactericides by inducing phase separation of charged and uncharged lipids inside the cytoplasma membrane of bacteria [106,156]. Eventually, the cytoplasma membrane disintegrates, which causes death of the microorganism [106,156]. For this reason, it was anticipated that Ag/PVA/PTBAM nanofibers would exhibit bactericidal activity to some degree even after depletion of the embedded silver nanoparticles. On the basis of these data, the synthesized Ag/PVA/PTBAM nanofibers had enhanced antibacterial performance because of the antibacterial properties of both the PTBAM nanofibers alone and the embedded silver nanoparticles.

Table 6 Minimum inhibitory concentration tests of various silver compounds[a]

Bacteria	Concn of Ag (ng/mL)[b]	Ag/PTBAM		Concn of Ag (ng/mL)[b]	Ag/PMMA		Concn of Ag (ng/mL)[b]	$AgNO_3$	
		24h	48h		24h	48h		24h	48h
E. coli	1718	−	−	1667	−	−	1783	−	−
	859	−	−	834	−	−	892	−	+
	430	−	−	417	−	−	446	−	+
	215	−	−	208	−	−	223	+	+
	107	−	−	104	−	−	111	+	+
	53.7	−	−	52.1	−	+	55.7	+	+
	26.8	−	+	26.1	+	+	27.9	+	+
	13.4	+	+	13.0	+	+	13.9	+	+
S. aureus	17182	−	−	16673	−	−	17831	−	+
	8591	−	−	8337	−	−	8915	+	+
	4296	−	−	4168	−	−	4458	+	+
	2148	−	−	2084	−	+	2229	+	+
	1611	−	+	1563	−	+	1670	+	+
	1074	+	+	1042	+	+	1114	+	+

[a] LB liquid media was clear before incubation with 2×10^4 to 10^5 per mL of *E.coli* or *S.aureus*; "−" no growth; "+"growth. [b] The concentration of Ag in the silver compounds was measured by ICP-atomic emission spectrometer with aqua-regia treatment.

4. Conclusion

The various silver-containing nanomaterials including silver chloride nanoparticles, silver bromide nanoparticles, Ag-embedded PVA nanofibers, and Ag-embedded PVA/PTBAM composite nanofibers were prepared by simple and environmentally benign methods and the synthesized nanomaterials exhibited potential properties in the application areas of antimicrobial and visible-light photocatalytic fields. The subtopics could be concluded in the viewpoint of subtopics as follows;

1. One-pot and environmentally benign synthetic route at a mild temperature was developed for the preparation of plasmon photocatalytic Ag@AgCl nanoparticles of controlled size. In this system, PVA was used as a stabilizer for the formation of Ag@AgCl nanoparticles through interaction with Ag+ ions; L-arginine was used as a mild reducing agent to form metallic Ag nanoclusters on the surface of the AgCl. The mechanism by which the AgCl nanoparticles were reduced was systematically studied, revealing that the metallic Ag content significantly affected the light absorption property and photocatalytic

performance of the as-prepared photocatalysts. More importantly, it was verified that the size of the AgCl substrate affected the absorption region of the Ag@AgCl nanocomposite. The prepared Ag@AgCl nanoparticles were used as a plasmonic photocatalyst for the degradation of organic dyes under visible light irradiation; they had stable photocatalytic activity and thus may be suitable for pollutant abatement applications.

2. Plasmon photocatalytic Ag@AgBr nanoparticles were synthesized in aqueous solution with PVA stabilizer. L-arginine was used as a mild reducing agent to form metallic Ag nanoparticles on the surface of the AgBr. The size of AgBr substrate nanoparticle can be controlled by varying reaction temperature and it was revealed that the size of the AgBr substrate affected the absorption region of the Ag@AgBr nanocomposite. The prepared Ag@AgBr nanoparticles were used as a plasmonic photocatalyst for the degradation of organic dyes under visible light irradiation. They even showed photocatalytic performance under direct sun-light condition.

3. Complex-mediated synthetic growth method was used to embed silver (Ag) nanoparticles in poly(vinyl alcohol) (PVA) nanofibers in an

aqueous solution. Azobisisobutyronitrile (AIBN) played a pivotal role in the preparation of the Ag/PVA nanofibers, *via* its cyano groups. AIBN was used to assemble the Ag ions to form Ag complexes in the early stages of the reaction. As the reaction temperature approached 60°C, AIBN decomposed *via* breakage of its C-N bonds, and thus the Ag compounds became disassembled. During this stage, Ag nanoparticles were aligned with a PVA assistant, which acted as a gelator and stabilizer for the formation of fibrous nanostructures under magnetic stirring conditions. As a result, PVA nanofibers (diameter: *ca.* 35 nm) were synthesized, with Ag nanoparticles (diameter: *ca.* 8 nm) embedded compactly in the inner part of the fiber. The formation of Ag/PVA composite nanofibers was systematically investigated with field-emission scanning electron microscopy, transmission electron microscopy, Fourier transform infrared spectroscopy, and X-ray photoelectron spectroscopy. Additionally, several control experiments were conducted and a plausible mechanism for the synthesis of Ag/PVA composite nanofibers was proposed.

4. Silver/PVA/PTBAM composite nanofibers were synthesized using one-pot, radical-mediated dispersion polymerization under aqueous

conditions. From UV-vis analysis, the embedded silver nanoparticles exhibited a lower tendency toward aggregation compared with colloidal silver nanoparticles. The fabricated Ag/PVA/PTBAM nanofibers had enhanced antibacterial activities against both Gram-negative *E. coli* and Gram-positive *S. aureus* based on the bactericidal properties of both the silver nanoparticles and the PTBAM substrate. The antibacterial kinetics and MIC test showed that the silver/PVA/PTBAM nanofiber had the enhanced killing rate and effective antimicrobial activity than $AgNO_3$, SSD, and Ag/PVA/PMMA nanofibers. In addition, the Ag/PVA/PTBAM nanofiber had an excellent release-antibacterial property than SSD in the modified Kirby-Bauer method. These results suggest that Ag/PVA/PTBAM composite nanofibers have potential for use in biofilms and hygienic and antiadhesion applications.

In summary, diverse silver complex nanomaterials were fabricated by simple and environmentally benign synthetic routes. PVA-stabilizing synthetic route was suggested for the fabrication of silver halide (AgBr, AgCl) nanoparticles. After partial reduction, the silver nanoparticles decorated silver halide nanocomposites shows excellent plasmonic photocatalytic under visible-light irradiation. In addition, silver-

embedded polymeric nanofibers (Ag/PVA and Ag/PVA/PTBAM) were synthetized by complex-mediated growth mechanism. In this system, the radical initiator (AIBN) played pivotal role in the formation of the nanostructures and PVA acted as a gelator for their fibrous structures. The synthesized Ag/PVA/PTBAM nanofibers presented excellent antibacterial activity against Gram-negative and Gram-positive bacteria compared to silver nitrate and SSD.

References

[1] H. Cui, Q. Li, S. Gao, J. K. Shang, *J. Ind. Eng. Chem.* **2012**, 18, 1428.

[2] J. P. Kottmann, O. J. F. Martin, D. R. Smith, S. Schultz, *Chem. Phys. Lett.* **2001**, *341*, 1.

[3] R. Ma, T. Sasaki, *Adv. Mater.* **2010**, *22*, 5082.

[4] G. A. Ozin, A.C. Arsenault, *Nanochemistry, A Chemical approach to nanomaterials*, RSC publishing, **2005**.

[5] C. P. Poole, F. J. Owens, *Introduction to nanotechnology*, Wiley-VCH, **2003**.

[6] G. Schmid, *Nanoparticles*, Wiley-VCH, **2004**.

[7] B. Lim, P. H. C. Camargo, Y. Xia, *Langmuir* **2008**, *24*, 10437.

[8] S. E. Skrabalak, L. Au, X. Li, Y. Xia, *Nature Protocols* **2007**, *2*, 2182.

[9] Y. Xia, Y. Xiong, B. Lim, S. E. Skrabalak, *Angew. Chem. Int. Ed.* **2009**, *48*, 60.

[10] Y. Oaki, H. Imai, *Adv. Mater.* **2006**, *18*, 1807.

[11] Y. Piao, J. Kim, H. B. Na, D. Kim, J. S. Baek, M. K. Ko, J. H. Lee, M. Shokouhimehr, T. Hyeon, *Nat. Mater.* **2008**, *7*, 242.

[12] H. Zhu, D. Yang, Y. Ji, H. Zhang, X. Shen, *J. Mater. Sci.* **2005**, *40*, 591.

[13] T. Yu, B. Lim, Y. Xia, *Angew. Chem. Int. Ed.* **2010**, *49*, 4484.

[14] H. Yoon, J. Jang, *Adv. Func. Mater.* **2009**, *19*, 1567.

[15] S. W. Lee, H. J. Lee, J. H. Choi, W. G. Koh, J. M. Myoung, J. H. Hur, J. J. Park, J. H. Cho, U. Jeong, *Nano lett.* **2010**, *10*, 347.

[16] K. J. Lee, W.-K. Oh, J. Song, S. Kim, J. Lee, J. Jang, *Chem. Commun.* **2010,** *46*, 5229.

[17] O. S. Kwon, S. J. Park, J. S. Lee, E. Park, T. Kim, H.-W. Park, S. A. You, H. Yoon, J. Jang, *Nano Letters* **2012**, *12*, 2797.

[18] G. A. Somorjai, *Chem. Rev.* **1996**, *96*, 1223.

[19] S. Jeong, K. Woo, D. Kim, S. Lim, J. S. Kim, H. Shin, Y. Xia, J. Moon, *Adv. Funct. Mater.* **2008**, *18*, 679.

[20] H. Cang, T. Sun, Z.-Y. Li, J. Chen, B. J. Wiley, Y. Xia, X. Li, *Opt. Lett.* **2005**, *30*, 3048.

[21] J. L. West, N. J. Halas, *Annu. Rev. Biomed. Eng.* **2003**, *5*, 285.

[22] B. Lim, Y. Xiong, Y. Xia, *Angew. Chem. Int. Ed.* **2007**, *46*, 9279.

[23] K. A. Willets, R. P. Van Duyne, *Annu. Rev. Phys. Chem.* **2007**, *58*, 267.

[24] G. C. Papavassiliou, *Prog. Solid State Chem.* **1979**, *12*, 185.

[25] R. Narayanan, M. A. El-Sayed, *J. Phys. Chem. B* **2005**, *109*, 12663.

[26] A. Zecchina, E. Groppo, S. Bordiga, *Chem. Eur. J.* **2007**, *13*, 2440.

[27] M. Faraday, *Philos. Trans. R. Soc. London* **1857**, *147*, 145.

[28] Y. Wang, Y. Zheng, C. Z. Huang, Y. Xia, *J. Am. Chem. Soc.* **2013**, *135*,

1941.

[29] Y. Sun, Y. Xia, *Science* **2002**, *298*, 2176.

[30] Y. Sun, B. Mayers, T. Herricks, Y. Xia, *Nano Lett.* **2003**, *3*, 955.

[31] Y. Xiong, I. Washio, J. Chen, H. Cai, Z.-Y. Li, Y. Xia, *Langmuir* **2006**, *22*, 8563.

[32] A. Nagy, G. Mestl, *Appl. Catal. A* **1999**, *188*, 337.

[33] P. Dallas, V. K. Sharma, R. Zboril, *Adv. Colloid Interface Sci.* **2011**, *166*, 119.

[34] J. R. Morones, J. L. Elechiguerra, A. Camacho, K. Holt, J. B. Kouri, J. T. Ramírez, M. J. Yacaman, *Nanotechnology*, **2005**, *16*, 2346.

[35] M. Lv, S. Su, Y. He, Q. Huang, W. Hu, D. Li, C. Fan, S.-T. Lee, *Adv. Mater.* **2010**, *22*, 5463.

[36] G. Begum, J. Manna, R. K. Rana, *Chem. Eur. J.* **2012**, *18*, 6847.

[37] P. Christopher, H. Xin, S. Linic, *Nat. Chem.* **2011**, *3*, 467.

[38] R. Georgekutty, M. K. Seery, S. C. Pillai, *J. Phys. Chem. C* **2008**, *112*, 13563.

[39] A. Pan, L. Yao, Y. Qin, Y. Yang, D. Kim, R. Yu, B. Zou, P. Werner, M. Zacharias, U. Gosele, *Nano Lett.* **2008**, *8*, 3413.

[40] P. Wang, B. Huang, X. Qin, X. Zhang, Y. Dai, J. Wei, M.-H. Whangbo, *Angew. Chem. Int. Ed.* **2008**, *47*, 7931.

[41] Y. Li, Y. Ding, *J. Phys. Chem. C* **2010**, *114*, 3175.

[42] H. Xu, H. Li, J. Xia, S. Yin, Z. Luo, L. Liu, L. Xu, *ACS Appl. Mater. Interfaces* **2011**, *3*, 22.

[43] P. Wang, B. Huang, X. Zhang, X. Qin, H. Jin, Y. Dai, Z. Wang, J. Wei, J. Zhan, S. Wang, J. Wang, M.-H. Whangbo, Chem. Eur. J. 2009, 15, 1821.

[44] C. An, S. Peng, Y. Sun, *Adv. Mater.* **2010**, *22*, 2570.

[45] S. Peng, Y. Sun, *J. Mater. Chem.* **2011**, *21*, 11644.

[46] C. An, R. Wang, S. Wang, X. Zhang, *J. Mater. Chem.* **2011**, *21*, 11532.

[47] S.-H. Jeon, P. Xu, B. Zhang, N. H. Mack, H. Tsai, L. Y. Chiang, H.-L. Wang, *J. Mater. Chem.* **2011**, *21*, 2550.

[48] R. Abargues, K. Abderrafi, E. Pedrueza, R. Gradess, J. Marqués-Hueso, J. L. Valdés, J. Martinez-Pastor, *New J. Chem*., **2009**, *33*, 1720.

[49] J. Y. Chun, H. K. Kang, L. Jeong, Y. O. Kang, J.-E. Oh, I.-S. Yeo, S. Y. Jung, W. H. Park, B.-M. Min, *Colloid. Surface. B.* **2010**, *78*, 334.

[50] X. Zan, M. Kozlov, T. J. McCarthy, Z. Su, *Biomacromolecules* **2010**, *11*, 1082.

[51] K. J. Lee, J. H. Oh, Y. Kim, J. Jang, *Chem. Mater*. **2006**, *18*, 5002

[52] J. Song, H. Oh, H. Kong, J. Jang, *J. Hazard. Mater*. **2011**, *187*, 311.

[53] M. Ikegame, K. Tajima, T. Aida, *Angew. Chem. Int. Ed*. **2003,** *42*, 2154.

[54] J. Jang, H. Yoon, *Chem. Commun*. **2003**, 720.

[55] T. Hatano, A.-H. Bae, M. Takeuchi, N. Fujita, K. Kaneko, H. Ihara, M. Takafuji, S. Shinkai, *Angew. Chem. Int. Ed.* **2004**, *43*, 465.

[56] J. Xie, X. Li, Y. Xia, *Macromol. Rapid Commun.* **2008**, *29*, 1775.

[57] N. Bhardwaj, S. C. Kundu, *Biotechnol. Adv.* **2010**, *28*, 325.

[58] Y.-S. Lee, T. L. Arinzeh, *Polymers* **2011**, *3*, 413.

[59] C. D. Saquing, J. L. Manasco, S. A. Khan, *Small* **2009**, *5*, 944.

[60] Q. Shi, N. Vitchuli, J. Nowak, J. M. Caldwell, F. Breidt, M. Bourham, X. Zhang, M. McCord, *Eur. Polym. J.* **2011**, *47*, 1402.

[61] H. R. Pant, M. P. Bajgai, K. T. Nam, Y. A. Seo, D. R. Pandeya, S. T. Hong, H. Y. Kim, *J. Hazard. Mater.* **2011**, *185*, 124.

[62] Y. Wang, Q. Zhang, C.-L. Zhang, P. Li, *Food Chem.* **2012**, *132*, 419.

[63] Q. Shi, N. Vitchuli, J. Nowak, J. Noar, J. M. Caldwell, F. Breidt, M. Bourham, M. McCord, X. Zhang, *J. Mater. Chem.* **2011**, *21*, 10330.

[64] N. Mahanta, S. Valiyaveettil, *RSC Advances*, **2013**, *3*, 2776.

[65] B. H. Jones, T. P. Lodge, *J. Am. Chem. Soc.* **2009**, *131*, 9746.

[66] L. Shi, C. Berkland, *Adv. Mater.* **2006**, *18*, 2315.

[67] B. Lim, Y. Xia, *Angew. Chem. Int. Ed.* **2011**, *50*, 76.

[68] A. Melaiye, Z. Sun, K. Hindi, A. Milsted, D. Ely, D. H. Reneker, C. A. Tessier, W. J. Youngs, *J. Am. Chem. Soc.* **2005**, *127*, 2285.

[69] H. Kong, J. Jang, *Langmuir* **2008**, *24*, 2051.

[70] H. Kong, J. Jang, *Chem. Commun.* **2006**, 3010.

[71] H. Kong, J. Jang, *Biomacromolecules* **2008**, *9*, 2677.

[72] H. Tong, S. Ouyang, Y. Bi, N. Umezawa, M. Oshikiri, J. Ye, *Adv. Mater.* **2012**, *24*, 229.

[73] M. Cherevatskaya, M. Neumann, S. Füldner, C. Harlander, S. Kümmel, S. Dankesreiter, A. Pfitzner, K. Zeitler, B. König, *Angew. Chem. Int. Ed.* **2012**, *51*, 4062.

[74] H. J. Yun, H. Lee, N. D. Kim, D. M. Lee, S. Yu, J. Yi, *ACS Nano* **2011**, *5*, 4084.

[75] S. X. Ouyang, J. H. Ye, *J. Am. Chem. Soc.* **2011**, *133*, 7757.

[76] J. S. Lee, O. S. Kwon, J. Jang, *J. Mater. Chem.* **2012**, *22*, 14565.

[77] E. Lee, J.-Y. Hong, H. Kang, J. Jang, *J. Hazard. Mater.* **2012**, *219-220*, 13.

[78] R. Dong, B. Tian, C. Zeng, T. Li, T. Wang, J. Zhang, *J. Phys. Chem. C* **2013**, *117*, 213.

[79] J. Yu, G. Dai, B. Huang, *J. Phys. Chem. C* **2009**, *113*, 16394.

[80] G. Zhang, W. Choi, *Chem. Commun.* **2012**, *48*, 10621.

[81] R. Asahi, T. Morikawa, T. Ohwaki, K. Aoki, Y. Taga, *Science* **2001**, *293*, 269.

[82] K. L. Kelly, E. Coronado, L. L. Zhao, G. C. Schatz, *J. Phys. Chem. B*

2003, *107*, 668.

[83] A. Moores, F. Goettmann, *New J. Chem.* **2006**, *30*, 1121.

[84] Z. Zhang, L. Zhang, M. N. Hedhili, H. Zhang, P. Wang, *Nano Lett.* **2013**, *13*, 14.

[85] S. Linic, P. Christopher, D. B. Ingram, *Nature Mater.* **2011**, *10*, 911.

[86] K. Awazu, M. Fujumaki, C. Rockstuhl, J. Tominaga, H. Murakami, Y. Ohki, N. Yoshida, T. Watanabe, *J. Am. Chem. Soc.* **2008**, *130*, 1676.

[87] Y. B. Tian, J. Zhang, *Catal. Surv. Asia* **2012**, *16*, 210.

[88] M. Choi, K.-H. Shin, J. Jang, *J. Colloid. Interface Sci.* **2010**, *341*, 83.

[89] Z. Lou, B. Huang, P. Wang, Z. Wang, X. Qin, X. Zhang, H. Cheng, Z. Zheng, Y. Dai, *Dalton Trans.* **2011**, *40*, 4104.

[90] M. L. Cohen, *Nature* **2000**, *406*, 762.

[91] H. W. Boucher, G. H. Talbot, J. S. Bradley, J. E. Edwards Jr., D. Gilbert, L. B. Rice, M. Scheld, B. Spellberg, J. Bartlett, *Clin. Infect. Dis.* **2009**, *48*, 1.

[92] L. B. Rice, *Curr. Opin. Microbiol.* **2009**, *12*, 476.

[93] P. Tenke, C. R. Riedl, G. L. Jones, G. J. Williams, D. Stickler, E. Nagy, *Int. J. Antimicrob. Agents* **2004**, S67.

[94] S. Hou, H. Gu, C. Smith, D. Ren, *Langmuir*, **2011**, *27*, 2686.

[95] V. Alt, T. Bechert, P. Steinrücke, M. Wagener, P. Seidel, E. Dingeldein,

E. Domann, R. Schnettler, *Biomaterials* **2004**, *25*, 4383.

[96] Z. Xiu, Q. Zhang, H. L. Puppala, V. L. Colvin, P. J. J. Alvarez, *Nano Lett.* **2012**, *12*, 4271.

[97] J. C. Grunlan, J. K. Choi, *Biomacromolecules* **2005**, *62*, 532.

[98] P. Dallas, J. Tucek, D. Jancik, M. Kolar, A. Panacek, R. Zboril, *Adv. Funct. Mater.* **2010**, *20*, 2347.

[99] P. Dallas, R. Zboril, A. B. Bourlinos, D. Jancik, D. Niarchos, A. Panacek, D. Petridis, *Macromol. Mater. Eng.* **2010**, *295*, 108.

[100] L. Kvitek, A. Panacek, J. Soukupova, M. Kolar, R. Vecerova, R. Prucek, M. Holecova, R. Zboril, *J. Phys. Chem. C* **2008**, *112*, 5825.

[101] G. Sun, T. Y. Chen, M. S. Habercom, W. B. Wheatlev, S. D. Worley, *J. Am. Water. Resour. As.* **1996**, *32*, 793.

[102] J. Liang, Y. Chen, K. Barnes, R. Wu, S. D. Worley, T.-S. Huang, *Biomaterials* **2006**, *27*, 2495.

[103] A. V. Bazilevsky, A. L. Yarin, C. M. Megaridis, *Langmuir* **2007**, *23*, 2311.

[104] L. Timofeeva, N. Kleshcheva, *Appl. Microbiol. Biotechnol.* **2011**, *89*, 475.

[105] F. Siedenbiedel, J. C. Tiller, *Polymers* **2012**, *4*, 46.

[106] G. Seyfriedsberger, K. Rametsteiner, W. Kern, *Eur. Polym. J.* **2006**, *42*,

3383.

[107] M. L. W. Knetsch, L. H. Koole, *Polymers* **2011**, *3*, 340.

[108] S. H. Hwang, J. Song, Y. Jung, O. Y. Kweon, H. Song, J. Jang, *Chem. Commun.* **2011**, *47*, 9164.

[109] G. Applerot, A. Lipovsky, R. Dror, N. Perkas, Y. Nitzan, R. Lubart, A. Gedanken, *Adv. Funct. Mater.* **2009**, *19*, 842.

[110] J. Song, H. Kong, J. Jang, *Chem. Commun.* **2009**, 5418.

[111] J. Song, H. Song, H. Kong, J.-Y. Hong, J. Jang, *J. Mater. Chem.* **2011**, *21*, 19317.

[112] E. Weir, A. Lawlor, A. Whelan, F. Regan, *Analyst* **2008**, *133*, 835.

[113] H. Kong, J. Song, J. Jang, *Environ. Sci. Technol.* **2010**, *44*, 5672.

[114] J. Song, H. Kong, C. Lee, S. H. Hwang, J. Jang, *ACS Appl. Mater. Interfaces* **2012**, *4*, 460.

[115] H. Dong, J. Huang, R. R. Koepsel, P. Ye, A. J. Russell, K. Matyjaszewski, *Biomacromolecules* **2011**, *12*, 1305.

[116] F. Guo-Dong, Y. Fang, L. Zhigang, L. Xinsong, *J. Mater. Chem.* **2008**, *18*, 859.

[117] A. Dong, S. Lan, J. Huang, T. Wang, T. Zhao, W. Wang, L. Xiao, X. Zheng, F. Liu, G. Gao, Y. Chen, *J. Colloid. Interf. Sci.* **2011**, *364*, 333.

[118] J. Jang, Y. Kim, *Chem. Commun.* **2008**, 4016.

[119] Y. Ye, Q. Song, Y. Mao, *J. Mater. Chem.* **2011**, *21*, 257.

[120] H. Kong, J. Song, J. Jang, *Chem. Commun.* **2010**, *46*, 6735.

[121] H. Kong, J. Song, J. Jang, *Macromol. Rapid Commun.* **2009**, *30*, 1350.

[122] K. Tan, S. K. Obendorf, *J. Membrane Sci.* **2007**, *305*, 287.

[123] K. H. Jung, M. W. Huh, W. Meng, J. Yuan, S. H. Hyun, J. S. Bae, M. H. Hudson, I. K. Kang, *J. Appl. Polym. Sci.* **2007**, *105*, 2816.

[124] X. Laloyaux, E. Fautré, T. Blin, V. Purohit, J. Leprince, T. Jouenne, A. M. Jonas, K. Glinel, *Adv. Mater.* **2010**, *22*, 5024.

[125] P. Chowdhury, S. K. Saha, A. Guha, S. K. Saha, *Appl. Surf. Sci.* **2012**, *261*, 598.

[126] A. Cooper, R. Oldinski, H. Ma, J. D. Bryers, M. Zhang, *Carbohyd. Polym.* **2013**, *92*, 254.

[127] H. Deng, P. Lin, S. Xin, R. Huang, W. Li, Y. Du, X. Zhou, J. Yang, *Carbohyd. Polym.* **2012**, *89*, 307.

[128] Y. Wen, Z. Tan, F. Sun, L. Sheng, X. Zhang, F. Yao, *Mater. Sci. Eng. C-Mater.* **2012**, *32*, 2026.

[129] J.-Y. Hong, H. Yoon, J. Jang, *Small*, **2010**, *6*, 679.

[130] S. Glaus, G. Calzaferri, *Photochem. Photobiol. Sci.* **2003**, *2*, 398.

[131] B. Wiley, Y. Sun, Y. Xia, *Acc. Chem. Res.* **2007**, *40*, 1067.

[132] J. Alegret, T. Rindzevicius, T. Pakizeh, Y. Alaverdyan, L. Gunnarsson,

M. Käll, *J. Phys. Chem. C* **2008**, *112*, 14313.

[133] L. Gunnarsson, T. Rindzevicius, J. Prikulis, B. Kasemo, M. Käll, *J. Phys. Chem. B* **2005**, *109*, 1079.

[134] P. K. Jain, W. Huang, M. A. El-Sayed, *Nano Lett.* **2007**, *7*, 2080.

[135] B. Li, R. Long, X. Zhong, Y. Bai, Z. Zhu, X. Zhang, M. Zhi, J. He, C. Wang, Z.-Y. Li, Y. Xiong, *Small* **2012**, *8*, 1710.

[136] J. Jiang, H. Li, L. Zhang, *Chem. Eur. J.* **2012**, *18*, 6360.

[137] L. Kuai, B. Geng, X. Chen, Y. Zhao, Y. Luo, *Langmuir* **2010**, *26*, 18723.

[138] T.-H. Nguyen, Y.-H. Kim, H.-Y. Song, B.-T. Lee, J. Biomed. Mater. Res. B **2011**, *96B*, 225.

[139] J. Jang, J. Bae, *Angew. Chem.* **2004**, *116*, 3891.

[140] D. Briggs, G. Beamson, *Anal. Chem.* **1993**, *65*, 1517.

[141] M. A. Gülgün, O. O. Popoola, W. M. Kriven, *J. Mater. Res.* **1995**, *10*, 1565.

[142] J. T. Clarke, E. R. Blout, *J. Polym. Sci.* **1946**, *1*, 419.

[143] Md. S. A. S. Shah, M. Nag, T. Kalagara, S. Singh, S. V. Manorama, *Chem. Mater.* **2008**, *20*, 2455.

[144] J. Liao, Y. Zhang, W. Yu, L. Xu, C. Ge, J. Liu, N. Gu, *Colloids Surf. A* **2003**, *223*, 177.

[145] N. P. Bayramgil, *J. Appl. Polym. Sci.* **2008**, *109*, 1205.

[146] T. Huang, R. W. Murray, *J. Phys. Chem. B* **2003**, *107*, 7434.

[147] J. P. Cason, K. Khambaswadkar, C. B. Roberts, *Ind. Eng. Chem. Res.* **2000**, *39*, 4749.

[148] A. Melaiye, R. S. Simons, A. Milsted, F. Pingitore, C. Wesdemiotis, C. A. Tessier, W. J. J. Youngs, *J. Med. Chem.* **2004**, *47*, 973.

[149] A. Henglein, *Chem. Mater.* **1998**, *10*, 444.

[150] V. Dal Lago, L. França de Oliveira, K. De Almeida Gonçalves, J. Kobarg, M. Borba Cardoso, *J. Mater. Chem.* **2011**, *21*, 12267.

[151] K. Rege, N. R. Raravikar, D.-Y. Kim, L. S. Schadler, P. M. Ajayan, J. S. Dordick, *Nano Lett.* **2003**, *3*, 829.

[152] M. Liong, B. France, K. A. Bradley, J. I. Zink, *Adv. Mater.* **2009**, *21*, 1684.

[153] R. Joerger, T. Klaus, C. G. Granqvist, *Adv. Mater.* **2000**, *12*, 407.

[154] Q. F. Wei, H. Ye, D. Y. Hou, H. B. Wang, W. D. Gao, *J. Appl. Polym. Sci.* **2006**, *99*, 2384.

[155] W. J. Li, C. T. Saurencin, E. J. Caterson, R. S. Tuan, F. K. Ko, *J. Biomed. Mater. Res. A* **2002**, *60*, 613.

[156] P. Ottersbach, B. Kossmann, *GIT Labor-Fachz.* **2002**, *46*, 452.

국문초록

최근 나노 크기의 물질의 제조가 많은 관심을 받고 있다. 나노 물질은 최소한 한변이 1 에서 100 나노미터의 이내의 길이를 갖는 작은 물질을 뜻하며, 이러한 작은 크기로 인해 상대적으로 크기가 큰 물질에 비해 독특한 화학적, 물리적, 그리고 광학적 특징을 지니게 된다. 초기의 금 나노입자로부터 최근의 그래핀에 이르기까지 다양한 나노물질이 발견, 개발되고 다양한 분야에 걸쳐 연구되고 있다. 하지만 여전히 친환경적이고 간단한 방법을 이용해 나노 물질을 제조하는 연구에 관한 보고는 부족한 실정이다.

본 학위논문에서는 친환경적이고 간단한 방법을 통해 은 컴플랙스 나노구조체를 제조하는 연구를 기술하였다. 폴리비닐 알코올을 안정화 물질로 사용하여 할로겐화은 (염화은, 브롬화은) 나노입자를 물상에서 제조하였다. 또한 반응 온도를 조절함 으로써 이렇게 제조된 나노입자의 크기를 조절 할 수 있었다. 이 반응 방법에서, 폴리비닐 알코올은 은 이온과의 상호작용을 통해 나노 크기의 할로겐화은 입자를 제조하는 데에 있어 안정제 역할을 하였다. 부분적인 환원과정을 거쳐 금속 은 나노 입자가 박힌 할로겐화은 나노복합체를 제조할

수 있었고, 이렇게 제조한 나노복합체는 가시광 영역의 빛을 흡수하는 특성을 보였다. 또한, 가시광 하에서 우수한 플라스몬-광촉매 성능을 나타내었다. 본 연구를 통해 할로겐화은 지지체의 크기가 빛 흡수 영역에 영향을 미친다는 것을 밝혀내었다.

또한, 간단한 물-상의 제조방법을 통해 은을 함유한 고분자 나노섬유를 제조하였다. 은/폴리비닐 알코올 나노섬유를 제조하는데에 있어서, AIBN이 은 이온과 컴플랙스를 형성하는 것을 밝혀내었다. 이러한 컴플랙스는 AIBN의 시안기와 은 이온 사이의 상호작용에 의한것으로 사료된다. 라디칼 개시제이기도 한 AIBN은 이 반응에서 은 이온의 환원제로서의 역할도 수행하였다. 또한, 폴리비닐 알코올은 섬유형태의 나노구조체를 제조하는데에 있어서 겔레이터 및 안정제로 사용하였다. 이러한 반응을 거쳐 물 상에서 온화한 온도하에서 은/폴리비닐 알코올 나노섬유를 제조할 수 있었다. 더하여, 위의 반응에 항균성 고분자의 단량체를 첨가함으로써 은/폴리비닐 알코올/항균성 고분자의 나노섬유를 제조할 수 있었다. 이 방법에서는 AIBN이 분산 중합의 라이칼 개시제의 역할을 수행하였다. 이렇게 제조한 나노섬유는 항균제로서 응용되었다.

본 학위논문에는 간단하고 친환경적인 공정을 통해 은을 함유한 나노물질들을 제조하고 그를 응용하는 가능성에 대한 연구를 수행한 내용을 담았다. 폴리비닐 알코올은 은을 함유한 나노복합체를 제조하는데에 있어서 안전제 및 구조 형성 유도체로서의 역할을 하였다. 본 학위논문에서 제시한 나노물질들은 항균, 광촉매 등의 환경분야에 응용이 가능할 것이다. 본 학위논문은 은이 박힌 할로겐화은 나노-광촉매와 은/고분자 나노섬유의 간단한 제조 방법을 제시할 뿐 아니라 금속을 함유한 나노복합체의 제조 과정에 대한 이해를 증진 시킬 수 있을 것으로 기대된다.

주요어: 은; 할로겐화은; 나노복합체; 폴리비닐 알코올; 광촉매; 항균
학 번: 2008-21086

고마움의 글

2004년에 학부에 입학하여 벌써 10년이 지났습니다. 그 동안 학교도 많이 바뀌어 새로운 건물이 생겨나고, 외부 음식점도 학교안에서 쉽게 찾아 볼 수 있습니다. 그 짧지 않은 시간 동안 저는 302동에서 저의 20대의 대부분의 시간을 보냈고, 그 시간이 헛되지 않아 이렇게 박사학위를 받게 되었습니다. 졸업논문까지 작성이 끝나고 뒤돌아보니 많은 생각들이 스쳐지나갑니다. 미숙하고 실수투성이던 연구실 막내가 이제는 송박사라 불리게 됐습니다. 고맙습니다. 제가 한명의 박사가 되기까지 많은 분들의 도움이 있었다는 걸 알고 있습니다. 이 고마움의 글을 통해 그 마음을 조금이나마 표현하고자 합니다. 누구보다도 먼저 저의 지도교수님이신 장정식 교수님께 큰 고마움의 마음을 전합니다. 늘 연구에 대한 열정과 성실한 자세를 강조하시며 스스로도 성실한 모습을 버리지 않고 보여주시는 교수님의 모습은 제게 큰 산과 같았습니다. 실수와 실패가 대부분인 연구 생활에서 포기하지 않고 연구를 계속해 나갈 수 있었던 데에는 교수님의 관심과 지도 편달이 있었기 때문입니다. 또한 바쁘신 와중에도 귀한 시간을 내시어 제 부족한 논문을 심사해 주시고 좋은 말씀으로 지도해주신 조재영 교수님, 김영규 교수님, 이종찬 교수님 , KIST 임순호 박사님께도 깊은 고마움의 마음을 전합니다.

대학원 6년의 시간동안 비좁은 연구실 공간에서 그 어느 곳보다 더 많은 시간을 보냈습니다. 따듯한 가족이 그리운 저에게는 연구실이 집이었고 교수님께서 아버지셨고, 연구원들이 제 가족이었습니다. 오지랖 넓은 저와 함께 연구실 생활을 해 주신 것만으로도 고맙습니다. 연구실에서 소중한 인연과 소중한 추억을 만들었습니다. 연구뿐만이 아니라 저의 인격과 가치관 형성에도 큰 영향을 주신 많은 선배님들과 친구, 후배들에게 고마운 마음을 전합니다.

한명 한명 이름을 말하며 인사를 전하지 않아도 저의 이 깊은 고마움을 느끼실 거라 믿습니다. 제 뒤에 남은 후배들에게 부지런하고 진실되게 연구를 대하면 틀림없이 좋은 결과가 있을 것이라고 말해 주고 싶습니다. 부디, 쉽지 않은 연구 생활에서 중도에 좌절하지 말고 부지런히 실패하시고 결국 찾아올 성공을 맛보시길 바랍니다.

박사학위를 받은 지금도 제가 부족한 점이 많다는 것을 잘 알고 있습니다. 이런 저에게 진심어린 지도와 관심, 응원을 보내 주시는 많은 분들께 고마운 마음을 전하며 글을 마무리 짓겠습니다. 항상 발전하여 지금보다 더욱 더 큰 사람이 되도록 늘 정진하겠습니다.

2013년 12월

관악을 내려가며

송주명 올림.